GRS

Buffering Performance of
GMZ and MX80
Bentonites for Geological
Disposal of High-Level
Radioactive Waste

BGR

中核集团 CNNC 核地研院 BRIUG

GRS

GRS - 702

Buffering Performance of GMZ and MX80 Bentonites for Geological Disposal of High-Level Radioactive Waste

Chun-Liang Zhang (GRS)
Ju Wang (BRIUG)
Stephan Kaufhold (BGR)
Yuemiao Liu (BRIUG)
Oliver Czaikowski (GRS)

November 2022

Foreword

Bentonite is world-widely taken as engineered barrier material for geological disposal of high-level radioactive waste (HLW). Within the ELF-China Pilot Project (10. 2020 - 08. 2022), thermo-hydro-mechanical-chemical processes in bentonite barrier systems were investigated using laboratory experiments and numerical modelling. The project was co-funded by the German Federal Ministry for Economic Affairs and Climate Action (BMWK) under contract number 02E11850B and by the China Atomic Energy Authority (CAEA) as well as the China National Nuclear Corporation (CNNC). The experiments were carried out jointly by the German and Chinese partners

- German Gesellschaft für Anlagen- und Reaktorsicherheit (GRS),
- German Federal Institute for Geosciences and Natural Resources (BGR),
- China Beijing Research Institute of Uranium Geology (BRIUG).

The experiments investigated the buffering performance of GMZ bentonite for the long-term safe isolation of HLW in granite at the Beishan site in China compared to the well-known MX80 bentonite. With the help of newly developed test methods, safety-relevant properties and behaviour of the bentonites were determined, including chemical and mineralogical composition, water absorption capacity, swelling capacity, water permeability, gas migration, self-sealing of engineered voids, deformations and strength, and thermal effects. A wide range of valuable results were obtained. It was found that the tested bentonite GMZ and MX80 behave in the same way in terms of quality. The quantitative differences in the properties stem from differences in montmorillonite content and dry density. Main findings include:

- the water uptake and retention capacity increases with increasing montmorillonite content;
- the swelling pressure builds up with hydration and increases exponentially with increasing montmorillonite content and dry density;
- the water permeability decreases exponentially with increasing montmorillonite content and dry density;
- the gas penetration in the water-saturated bentonites requires high overpressures to create micro-fissures for gas passage;
- the highly saturated bentonite has a high plastic deformability;

- the engineered voids in the bentonite buffer can seal themselves due to the high swelling capacity and ductile deformability of the bentonite; and
- no significant thermal effects on the buffering performance of the bentonites were found in the tested range of 20 – 100 °C.

It should be noted that further research is needed to strengthen the database, improve the understanding of the coupled thermo-hydro-mechanical behaviour of the bentonites, validate the constitutive models and numerical codes for accurate prediction and assessment of the repository performance and safety.

Contents

IV

1   Introduction

A deep geological repository (DGR) has been proposed for safe isolation of high-level radioactive waste (HLW) in the granite at Beishan site in the north-western China. Its preliminary concept is based on a multi-barrier system, which is composed of the host rock and engineering barriers, as illustrated in figure 1.1 /WAN 18/. The engineered barrier system (EBS) comprises the waste canister, bentonite buffer, as well as backfill and seal of the whole facility including boreholes, drifts, shafts, and ramps. The bentonite buffer consists of pre-compacted blocks surrounding the waste canister and pellets filling gaps remaining in the deposition hole. The most important functions of the buffer are to ensure the stability of the barrier system and to limit transport of radionuclides with water flow into the biosphere/SKB 11/WAN 18/VIL 20/.
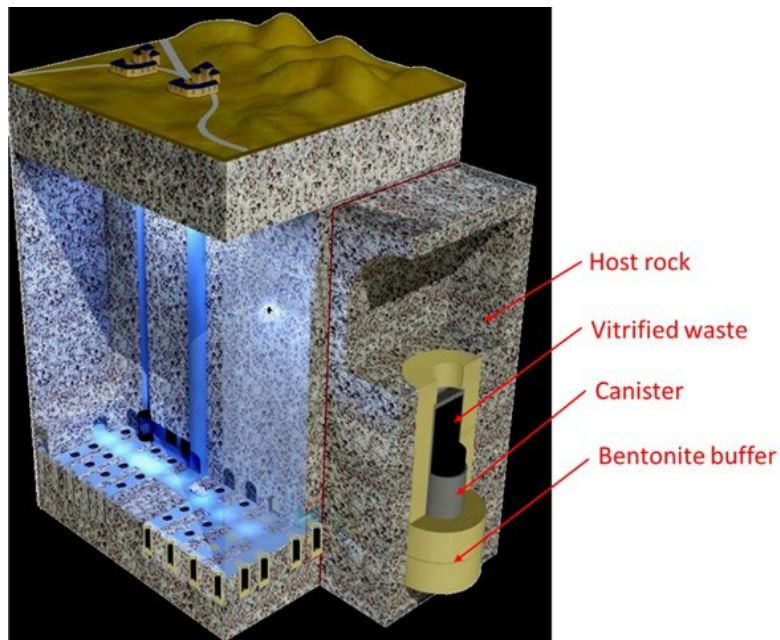
Fig. 1.1   Preliminary concept for disposal of HLW in granite in China with multiple barriers (waste canister, bentonite buffer, host rock) (Wang et al,. 2018) /WAN 18/

As a candidate buffer material, GaoMiaoZi (GMZ) bentonite has been investigated with respect to the requirements on the buffer such as:

 a) sufficiently high swelling capacity to seal engineered voids and gaps in the backfilled deposition holes,

 b) low porosity and hydraulic conductivity to limit water flow and radionuclide transport,

 c) high sorption capacity to retard radionuclide release from the waste,

d) sufficient plasticity to protect the canister from damage through hard contact with the surrounding rock, and

e) allowing gas release without compromising the integrity and barrier functions of the multi-barrier-system.

During the last two decades, GMZ bentonite was extensively characterized in terms of thermo-hydro-mechanical-chemical (THMC) properties /LIU 03/10/YE 13/ZHU 13/ /CHE 15/XU 17/SUN 18/ZHA 19/CUI 21/. Particularly, a large-scale mock-up experiment was carried out to investigate THM processes occurring in the bentonite buffer surrounding HLW /LIU 14/ CHE 14/. The bentonite buffer consisted of pre-compacted blocks with a dry density of 1.7 g/cm^3 and pellets filling the annular gap between the blocks and the boundary wall. It was heated by a central heater up to a maximum temperature of 90 °C and hydrated by injecting the Beishan granite groundwater to the external surface of the buffer. The observed THM processes were numerically simulated and analysed.

In the framwork of the German-Chinese cooperation programme in the context of disposal of radioactive waste, a joint research project – ELF China Project /ELF 20/ was launched 2020 to improve the understanding of the coupled THMC behaviour of bentonite buffer and to enhance the model predictability of the long-term performance of a repository in crystalline rock. The research activities during the first pilot phase (from 10.2020 to 08.2022) focused on development of experimental methods to investigate THMC properties of bentonite and establishment of nummerical models to simulate the mock-up test.

Among others, GRS focused on laboratory experiments to study geotechnical properties of GMZ bentonite in comparison with the well-known MX80 bentonite, which was mostly characterized as buffer material for DGRs in many countries (e.g., Finland, Sweden, France, Switzerland). The experiments considered the dynamic buffer conditions expected in the repository. As HLW canisters and bentonite blocks/pellets are emplaced in the deposition holes, the temperature will rise by heat emission from the waste. Simultaneously, a hydration process will take place in the buffer by taking up water from the surrounding rock. The water uptake and retention behaviour are essential for prediction of the saturation process in the buffer. Upon water saturation, the bentonite will swell and seal the engineered gaps/voids and then swelling pressure will build up. The swelling pressure is responsible for the integrity and stability of the buffer-rock system. The most important barrier function of the buffer will be ensured by its low hydraulic conductivity to limit advective transport of radionuclides with water flow. When moisture contacts the

metallic canisters and components of the construction, anaerobic corrosion will occur and produce gases. In early stage before full water saturation of the buffer, the gases can easily escape without build-up of high gas pressure. When the buffer is highly saturated, the gas flow will be hindered and accumulated, which could lead to high gas pressures accessing certain thresholds and impairing the integrity of the buffer-rock system /HOR 96/ROD 99/SEL 14/HAR 17/LEV 20/. Thus, the knowledge of gas migration in the water-saturated buffer is necessary for safety assessment of the DGR. Moreover, the host rock may also be damaged through geological events, e.g., earthquake (in worst case scenario). The local movement of fragmented blocks may cause shear stress and deformation in the buffer. A high plasticity is required on the buffer to avoid direct contact with the hard rock and hence damage of the canisters.

The important properties and responses of the bentonites as HLW buffer were investigated under the THM buffer conditions:

- chemical and mineralogical compositions
- water uptake and retention capacity
- hydration and induced swelling pressure
- water conductivity under different hydraulic gradients
- gas penetration and impact
- self-sealing of engineered voids/gaps
- shear deformation and strength, and
- thermal effects.

Specific test setups and methods were developed and applied for determination of such many different properties of the bentonites. The experiments performed and results achieved are presented in this project final report.

2　Experiments and results

2.1　Basic characteristics of GMZ and MX80 bentonites

Two types of the natural GMZ bentonite, GMZ01 and GZM02, were extracted from the deep and shallow positions of the bedded deposit in the northern China – Inner Mongolia autonomous region. Up to now, GMZ01 has been more intensively investigated compared to GMZ02. Moreover, the commercial MX80 bentonite from Wyoming in USA was taken as reference for comparison, because its behaviour is mostly characterized and deeply understood.

The sample materials GMZ01 and GMZ02 were milled powder with grain sizes smaller than 74 μm, whereas MX80 was granulated by crushing pre-compacted blocks of a dry density of 2.0 g/cm^3 to grain sizes of 0.2 – 2 mm. Figure 2.1 pictures the sample materials. Their initial water contents were measured after drying at 105 °C for 2 days to values of 10.3 % at GMZ01, 8.0 % at GMZ02 and 12.6 % at MX80, respectively. The grain densities were determined on the dried materials by means of a helium gas pycnometer. Quite similar values were obtained to 2.67 g/cm^3 for MX80, and 2.66 g/cm^3 for GMZ01 and GMZ02. The different water contents are dependent on the material mineralogical compositions and storage conditions.

GMZ01, d < 74 μm　　　　GMZ02, d < 74 μm　　　　MX80, d < 2 mm
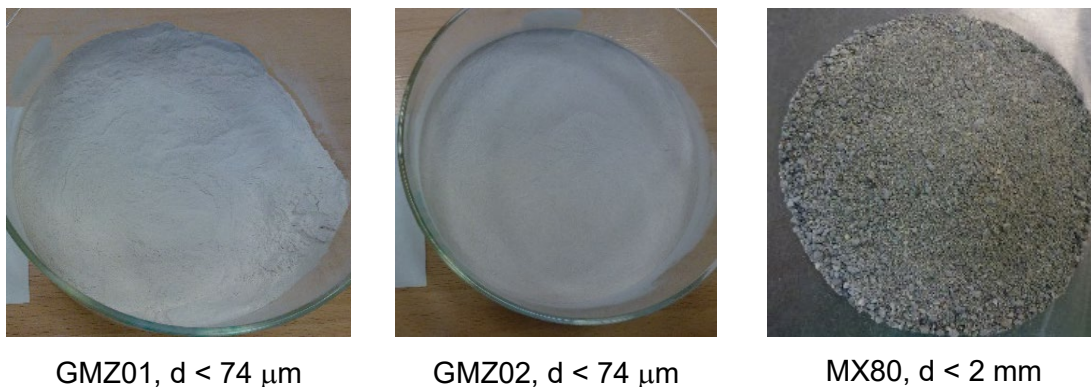
Fig. 2.1　Pictures of tested bentonite powder GMZ01 and GMZ02 as well as granular bentonite MX80

The chemical compositions, exchangeable cations and cation exchange capacity (CEC) of bentonite GMZ01 and GMZ02 were determined by BRIUG and summarized in tables 2.1 and 2.2. The minerological compositions of GMZ01 and GMZ02 determined by BRIUG are given in table 2.3. The previous experiments /LIU 10/ indicated that the mineralogical composition of GMZ01 does not change after preheating at 80 – 95 °C and

exposuring to water for several months, whereas MX80 exhibits slightly change after the treatment; and moreover, the chemical composition, cation exchange capacity and exchangeable cation of both bentonites do not change significantly.

Tab. 2.1   Chemical compositions of bentonite GMZ01 and GMZ02 (BRIUG)

Sample	Al_2O_3	SiO_2	P_2O_3	CaO	K_2O	TiO_2	FeO
GMZ01	14.24	68.40	0.05	0.99	0.68	0.14	0.26
GMZ02	14.19	70.70		1.11	2.5	0.08	
continuing	TFe_2O_3	MgO	Na_2O	MnO	SO_3	Ignition loss	
GMZ01	2.53	3.31	1.62	0.036		7.67	
GMZ02	1.17	2.37	1.47		0.03	5.39	

Tab. 2.2   Exchangeable cation and cation exchange capacity (CEC) of GMZ01 and GMZ02 (BRIUG)

Sample	Exchangeable cation		(mmol/100g)		CEC
	$E(K^+)$	$E(Na^+)$	$E(1/2Ca^{2+})$	$E(1/2Mg^{2+})$	(mmol/100g)
GMZ01	0.78	35.42	21.68	12.92	75.67
GMZ02	0.99	28.95	20.66	10.49	64.70

Tab. 2.3   Mineralogical compositions of GMZ01 and GMZ02 (BRIUG)

Sample	Montmorillonite	Quartz	Feldspar	Cristobalite	Mica	Zeolite
GMZ01	73.2	8.7	7.6	9.0	0	0
GMZ02	48.0	27.9	14.6	1.2	1.5	6.9

The mineralogical compositions of the sample materials were determined at the German Federal Institute for Geosciences and Natural Resources (BGR) by means of X-ray diffraction and Rietveld analysis. Considering the maximum temperature of 90 °C designed for the buffer, the mineralogical analysis was performed on the samples preheated at 105 °C for 14 days (B) and without heat treatment (A). The measured results are summarized in table 2.4. It is obvious that the studied bentonites consist predominantly of montmorillonite amounting to 86 % in MX80, 71 – 74 % in GMZ01 and 56 % in GMZ02, respectively. Accessory minerals are quartz, cristobalite, plagioclase, K-feldspar, etc. It is to be noted that the preheating did not affect the mineralogical compositions of the bentonites. Moreover, the present results are consistent with the data from BRIUG /LIU 10/ for GMZ01 and GMZ02, and from literature /KAR 07/PLÖ 07/ for MX80.

**Tab. 2.4**   Minerlogical compositions of the tested bentonites GMZ01, GMZ02 and MX80 (BGR)

Bentonite	GMZ01		GMZ02		MX80	
Mineral content (%)	A	B	A	B	A	B
Montmorillonite	71	74	56	56	86	86
Quartz	14	12	17	17	6	6
Cristobalite	6	6	3	3	1	1
Plagioclase	6	6	6	7	2	3
K-Feldspar	3	2	8	7	3	1
Clinoptilolite			6	6		
Mica			4	4		
Gypsum					< 1	2
Pyrite					< 1	< 1
Apatite					< 1	< 1

A: samples without heat treatment
B: samples preheated at 105 °C for 14 days

The dominat clay mineral in the bentonites is montmorillonite with fraction of f_m = 86 % in MX80, 71 – 74 % in GMZ01 and 56 % in GMZ02, respectively. Montmorillonite is responsible for water adsorption and swelling. The generally accepted structure of montmorillonite is a unit made of an alumina octahedral sheet sandwiched between two silica tetrahedral sheets /PUS 90/BRA 02/HUE 07/YON 12/BIR 17/: (Pusch et al. 1990; Bradbury and Baeyens 2002; Hueckel et al. 2002; Yong et al. 2012; Birgersson et al. 2017). Figure 2.2 shows a schematic of the montmorillonite structure (taken from /BRA/). The tetrahedral-octahedral-tetrahedral (TOT) layers of typical particles have dimensions in the a- and b- directions between 50 and 200 nm and combine one above the other in the c-direction to form platelets. The thickness of these platelets depends on the water content and type of exchangeable cation but commonly only a few TOT-layers form the primary particles. The number of platelets in each primary particle varies from 3 – 5 in Na-montmorillonite to 10-20 (and more) for a Ca-montmorillonite /PUS 90). Larger clay particles are formed from stacks of these platelets (aggregates). Water and other polar molecules can enter between the TOT-layers causing expansion in the c-direction (interlayer swelling). The c-axis lattice parameter is ~ 0.96 nm in the absence of any polar molecule in the interlayer. These so-called 2:1 layers (or TOT layer) have a permanent negative charge, which is balanced by exchangeable cations which in turn can take up water by hydration. In a simplified view water uptake is distinguished according to the number of water layers which formed. Each layer of water increases the c-spacing by

~0.25 nm. There are between 1 and 4 layers of H_2O in the interlayer space after saturation, depending on the ambient conditions. The water uptake initiates swelling of the layers if unconfined or generates repulsive forces (swelling pressure) between the layers under confined conditions.
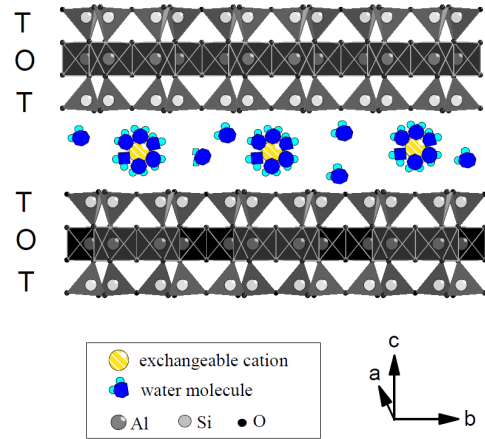
Fig. 2.2   Schematic representation of the montmorillonite structure (taken from Bradbury and Baeyens 2002 /BRA 02/)

2.2   Water retention

2.2.1   Test method

As the initially dry bentonite in form of blocks and granulated pellets is emplaced in disposition holes, a hydration or saturation process takes place in the buffer by taking up water from the humid surrounding rock under effect of vapour-pressure gradient or suction gradient. The water uptake and retention capacity of a bentonite buffer dominates its THMC properties and performance. This crucial property was firstly determined for the bentonites using vapour transfer technique under free and confined conditions.

Figure 2.3a shows two typical specimens under free and confined conditions respectively. The loose specimens with an initial weight of 50 g each were placed in bowls, while the compacted ones were confined in stainless steel thick-wall cells of 50 mm diameter and 20 mm height. The compacted GMZ01 and GMZ02 specimens with respective dry densities of 1.7 g/cm³ and 1.8 g/cm³ are representative of the designed buffer blocks /LIU 14/CHE 14/, while MX80 ones with a dry density of 1.5 g/cm³ are consistent with that emplaced in a horizontal drift at Mont-Terri Underground Rock Laboratory /MÜL 17/. The specimens in the cells were covered with sintered porous discs,

which allow exchange of water vapour in- and outside. Under applied vapour-pressure or suction gradients between the specimens and the surrounding air, water molecules migrated by diffusion from the humid air into the pore space in relatively dry specimens, or inversely. Whereas the relative humidity in each desiccator was continuously recorded by transistor psychrometer sensors, the amount of water uptake was measured by weighing the specimens at time intervals of 1 – 2 months until equilibrium was reached over total durations of 8 – 10 months. The specimens were placed in desiccators (Fig. 2.3b) at different relative humidity values adjusted using different salt solutions as given in table 2.5. The relative humidity RH is correlated to the matrix suction s by the psychrometric law /FRE 93/:

$$ s = -\frac{\rho_w RT}{M_w} \ln(RH) \tag{2.1} $$

where T is the absolute temperature, R is the universal gas constant, ρ_w and M_w are the density and the molecular mass of water, respectively. A range of RH–values of 22 % to 100 % was applied, corresponding to s = 207 to 0 MPa at temperature of 24 °C.

a. bentonite specimens placed in a bowl and confined in a cell

b. specimens placed in desiccators at different relative humidities

Fig. 2.3   Pictures of bentonite specimens placed in desiccators for measurement of water retention capacities at different humid conditions

Tab. 2.5   Salt solutions used for the measurement of water retention capacities of bentonites GMZ01, GMZ02 and MX80 at different relative humidities

Salt solution	Relative humidity RH (%)	Suction s (MPa)
LiCl	22.0	207.1
$CaCl_2$	34.5	145.6
$Mg(NO_3)_2 \cdot 2H_2O$	55.0	81.8
KJ	67.0	54.8
NaCl	73.0	43.0
KCl	81.3	28.3
$ZnSO_4 \cdot 7H_2O$	86.7	19.5
$Na_2HPO_4 \cdot 12H_2O$	95.0	7.0
$CuSO_4 \cdot 5H_2O$	96.5	4.9
H_2O	100.0	0.0

2.2.2   Test results

Water uptake

Figure 2.4 presents the evolution of water uptake by the confined bentonites GMZ01 with a dry density of ρ_d = 1.7 g/cm^3, GMZ02 with ρ_d = 1.8 g/cm^3 and MX80 with ρ_d = 1.5 g/cm^3 at different humidity values of RH = 23 % to 100 %. All the specimens took up water from the humid environment at RH > 50 %. The amount of water uptake increases with time to a constant as equilibrium is reached. The duration to equilibrium increases with increasing the relative humidity. At RH > 95 %, the water uptake to equilibrium needs more than a half of year for the relatively large and dense specimens. As the equilibrium was reached at the specimens of GMZ01 and GMZ02 at RH = 52 %, 76 % and 87 %, the salt solutions in the desiccators were exchanged to lower humidity values of RH = 23 %, 35 % and 63 %, respectively. Consequently, some of the previously adsorbed water desorbed to a new equilibrium. The desorption of MX80 specimens occurred at RH < 31 %.

Water retention

Water contents achieved at equilibrium are depicted in figure 2.5 as a function of suction for all specimens. As expected, water content of each bentonite increases with decreasing suction to a maximum at zero suction. The low porosities of the compacted specimens under volume-constraint conditions limited the water uptake, particularly at low suctions s < 5 – 10 MPa. Moreover, adsorbed water content is largely determined by the fraction of montmorillonite (f_m) in bentonite. The maximum water content for the loose

MX80 bentonite with f_m = 86 % is about two and three times that for GMZ01 with f_m = 74 % and GMZ02 with f_m = 56 %, respectively. For the volume-constraint specimens, the degree of water saturation is usually calculated by

$$S_w = \frac{V_w}{V_v} = \frac{\rho_d \times w}{\rho_w \times \phi}$$ (2.2)

where V_w is the volume of the pore water, V_v is the volume of the pore void, ρ_d is the dry density of the specimen, ρ_w is the density of the pore water, w is the mass water content, and ϕ is the porosity. Assuming the density of normal water ρ_w = 1.0 g/cm³, the calculation indicates unrealistic "oversaturation" (S_w > 100 %) for the compacted specimens at zero suction: S_w = 145 % for MX80, 121 % for GMZ01, and 101 % for GMZ02. This is because the density of pore water in a compacted bentonite is higher than the normal one /MIT 76/HUE 02/VIL 10/. Assuming that these specimens were fully saturated with the maximum water contents, S_w = 100 %, the densities of the pore waters can be estimated from back calculation: ρ_w = 1.37 g/cm³ for MX80 with ρ_d = 1.5 g/cm³ and ϕ = 46%; ρ_w = 1.12 g/cm³ for GMZ01 with ρ_d = 1.7 g/cm³ and ϕ = 38.8 %; and ρ_w = 1.01 g/cm³ for GMZ02 with ρ_d = 1.8 g/cm³ and ϕ = 35.3 %. The higher density of the pore water in MX80 is attributed to the higher montmorillonite content, compared to GMZ01 and GMZ02. Similar results were also reported for the pore water in compacted FEBEX bentonite /VIL 10/.
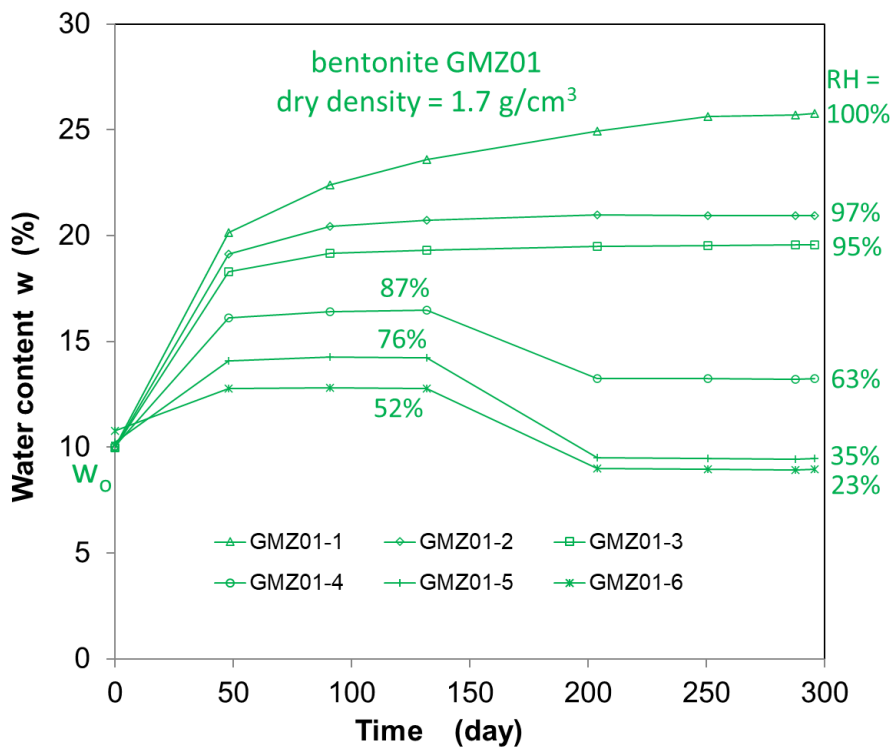
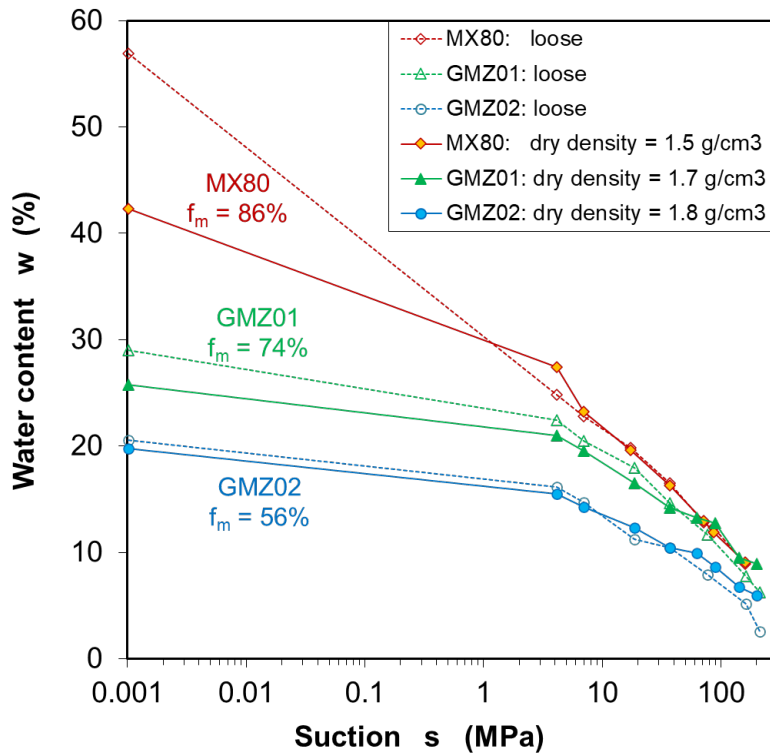a. Bentonite GMZ01 with a dry density of 1.7 g/cm³
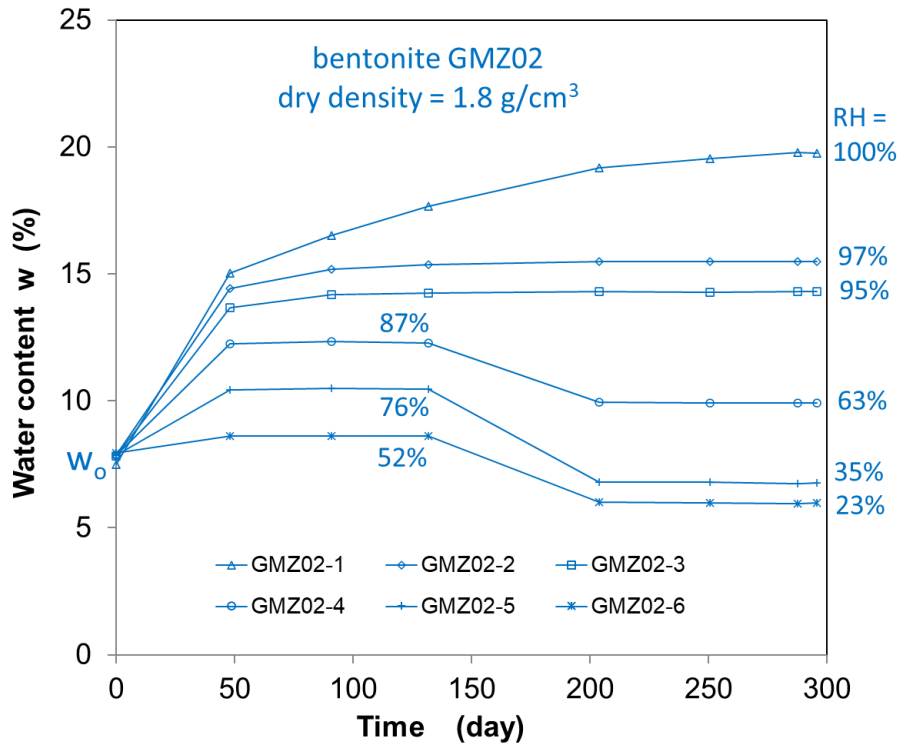
b. Bentonite GMZ02 with a dry density of 1.8 g/cm^3
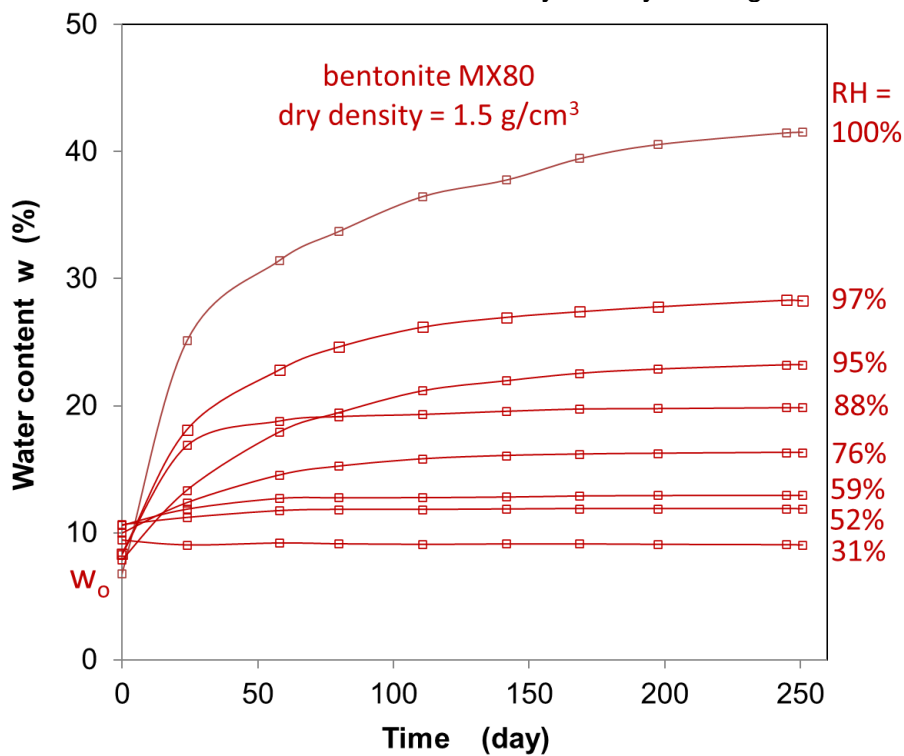
c. Bentonite MX80 with a dry density of 1.5 g/cm^3

Fig. 2.4 Evolution of water uptake measured on the compacted bentonites GMZ01, GMZ02 and MX80 under confined conditions

Fig. 2.5   Water retention curves of the loose and compacted bentonites GMZ01, GMZ02 and MX80

Porewater in bentonite

The high capacity of water adsorption of montmorillonite is due to its layer-structure with permanent negative charges and physical-chemical interactions with water /BRA 02/ /YON 12/BIR 17/VIL 20/. Figure 2.6 illustrates a schematic of the microstructure and pore water in compacted and saturated MX80 bentonite, which was proposed by Bradbury and Baeyens /BRA 02/. It is to be noted that the elements included in figure 2.6 are not to scale: accessory minerals are three orders of magnitude larger than montmorillonite grains that have a much more bladed habit (~40 times wider than thick) and consist of fewer sheets than shown in this figure /JEN 19/. The microstructure of montmorillonite is a unit made of an alumina octahedral sheet sandwiched between two silica tetrahedral sheets. The layers stack to form platelets. The negative charges in these layers are the cause of water uptake. There is a broad consensus that three types of water in bentonite can be distinguished: interlayer water, double-layer water, and free water. The interlayer water is adsorbed on the internal surfaces of the montmorillonite units and immobile. The double-layer water exists in the electrical double layers associated with the external surfaces of the clay stacks (particles or clusters). On the external surfaces of the stacks, the water is strongly bounded and immobile too. The adsorption force in the double-layer water decreases with increasing distance from the surfaces. The free water exists in

relatively large pore space surrounding the clay stacks and other mineral particles. The internally and externally adsorbed water is denser and more viscous than the free water /MIT 76/HUE 02/VIL 10/. The distributions and proportions of the different types of water in bentonite strongly depends on the amount of permanent charge, exchangeable cations, soluble components (calcite gypsum), dry density (or porosity), and water content /KAU 10/JEN 19/. Therefore, the given model of water distribution in figure 3 cannot be generalized for all types of bentonites with different cations (monovalent, divalent, and mixed). As reported in /MUU 87/BRA 07/, the content of free water in saturated bentonite MX80 is below 5 % at dry densities of 1.2 – 1.8 g/cm3. The tested bentonites GMZ01 and GMZ02 consist of relatively smaller montmorillonite contents and thus comprise more proportions of free water. The conceptual model in figure 2.6 (even though not for all bentonites) is helpful for understanding micro-mechanisms of THMC macroprocesses occurring in the bentonite buffer.
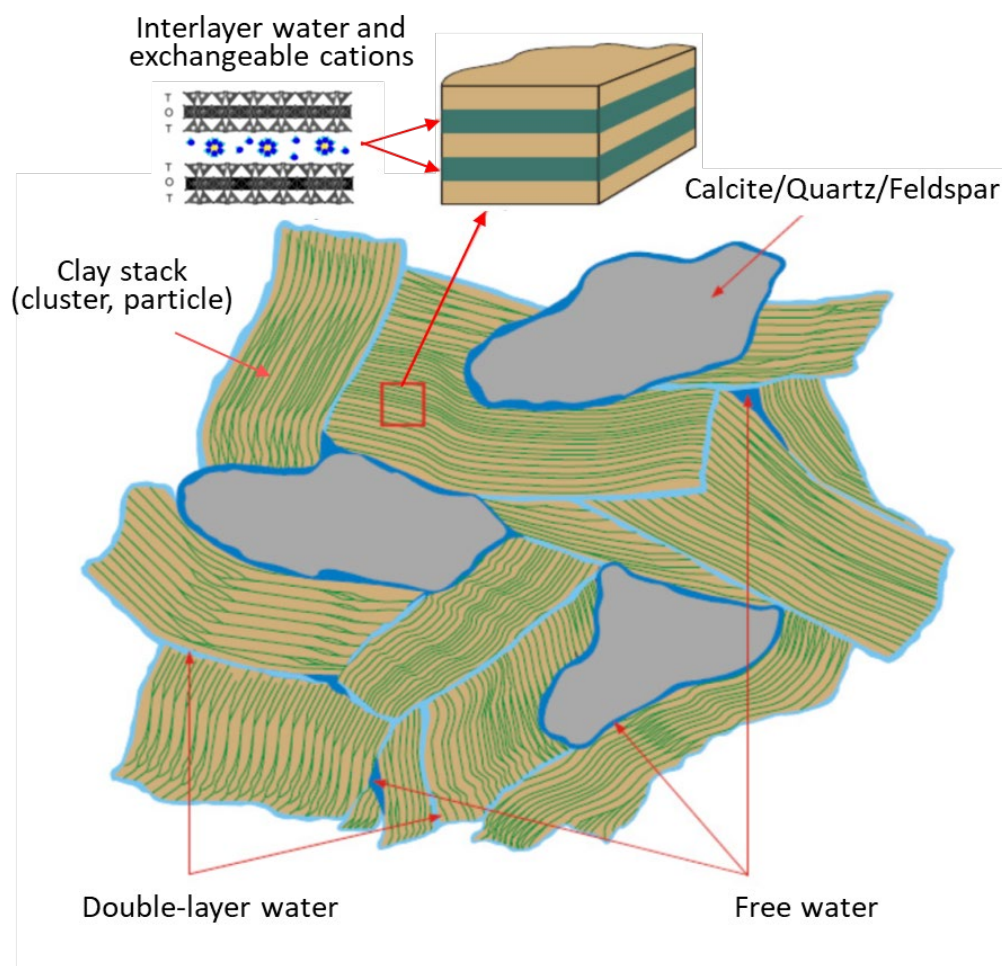
Fig. 2.6   Schematic of the microstructure and water (interlayer, double-layer, and free water) in compacted bentonite (from Bradbury and Baeyens 2002 /BRA 02/)

2.3 Swelling pressure

Bentonite buffer emplaced in the deposition holes tends to swelling with hydration, sealing the engineered gaps and voids, and then upbuilding of swelling pressure against the rigid rock boundaries. Certain swelling pressure is required to ensure the mechanical stability and barrier function of the buffer. Swelling pressures of the three kinds of bentonites (GMZ01, GMZ02, MX80) were determined at various dry densities of 1.8 g/cm^3 for pre-compacted blocks to ~1.0 g/cm^3 for pellets filling the engineered voids.

2.3.1 Test method

Setup

A specific setup was developed and used for sequential measurements of swelling pressure, water permeability, and gas penetration behaviour of the bentonites, as shown in figure 4. It consists of 14 stainless steel cells, a syringe pump, hydraulic lines, and measuring instruments. The cells were designed for high rigidity with a wall thickness of 30 mm, in which specimens can be compacted to high densities. The specimen is fixed by screwing a thick cap over the cell wall with 20 spiral turns over long distance of 40 mm to constrain volume expansion during development of swelling pressure up to 30 MPa. This setup allows parallel testing on different specimens under identical conditions, so that one can obtain a great amount of data from each specimen and hence save up the total time expenditure. Another advantage is the possibility to compare the measured properties and responses of the different specimens under the same boundary conditions.

Specimens

Different kinds of specimens were prepared for testing as shown in figure 5: compacted powder/granules, loose pellets, and assembled blocks with gaps. The compacted specimens were compacted in the cells to a size of 50 diameter and 15 mm height but different dry densities of r_d = 1.3 – 1.8 g/cm^3. The pellets were produced by crushing pre-compacted blocks (r_d = 1.7 g/cm^3) to grain sizes of 2 – 4 mm. The dry density of the loosely emplaced pellets was relatively low at r_d = 0.87 g/cm^3. The assembled blocks consisted of a central vertical gap of 3 mm width and had an average dry density of 1.65 g/cm^3. A mixture of pellets-blocks was prepared to a height of 15 mm for each layer and to an

average dry density of 1.31 g/cm³. All specimens were installed in the cells and heated at 105 °C for 2 – 3 days to match the initial dry conditions of the buffer induced by heating from HLW. The adjusted temperature is higher than the designed one for the repository to ensure some extrapolation of test data beyond that. The preheating caused some contraction and separation of the specimens from the cell walls. Thus, possible effect of friction between specimen and cell wall could be avoided for precise measurement of swelling pressure using the load cell at the top. The test temperature was controlled at 24±1 °C.

a. layout

b. cell elements

c. testing system
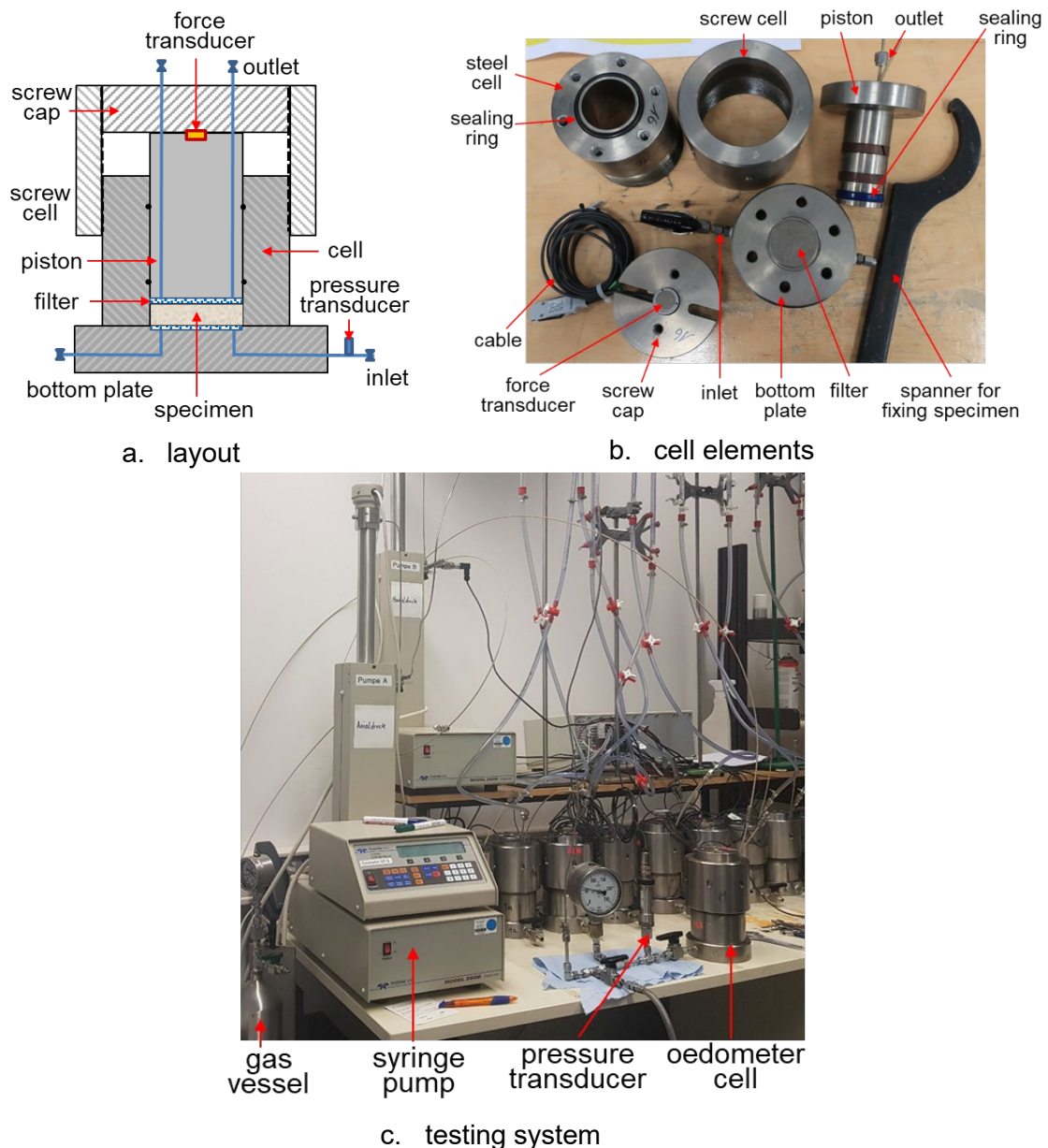
Fig. 2.7 A setup with parallel arranged oedometer cells for sequential measurements of water saturation, swelling pressure, water permeability, and gas penetration behaviour of different bentonite specimens under identical conditions

16

Fig. 2.8   Different kinds of specimens prepared using GMZ01 bentonite

The specimens were hydrated by infiltration of synthetic Beishan site groundwater (BSW) from the scaled burette into the bottom of each specimen at small height differences of 0.5 – 0.8 m. The synthetic water was manufactured according to the chemistry of the groundwater in the granite at depths of 510 – 540 m (table 2.6 after Zhou et al. 2020 /ZHO 20/). The chemical components of the synthetic water is given in table 2.7. The *pH* was 7.5. For some tests on MX80 bentonite, synthetic Opalinus clay water (OPAW) was applied too (table 2.8).

Tab. 2.6   Chemical components of the Beishan granite groundwater in borehole BS15-3 at depths of 509-538 m (Zhou et al. 2020 /ZHO 20/)

Component	Na^+	K^+	Mg^{2+}	Ca^{2+}	Cl^-	SO_4^{2-}	HCO_3^-
Content (mg/L)	921	10.1	42.8	181	1006	1220	150

Tab. 2.7   Chemical composition of the synthetic Beishan granite groundwater

Component	NaCl	$NaHCO_3$	$KHCO_3$	$MgSO_4 \cdot 7H_2O$	$CaCl_2 \cdot 2H_2O$	Na_2SO_4
Content (g/L)	2.045	0.370	0.052	0.868	1.328	3.108

17

Tab. 2.8   Main chemical components of the synthetic Opalinus clay water at Mont-Terri after Pearson (1999) /PEA 99/

Component	Na$^+$	Cl$^-$	Mg^{2+}	Ca^{2+}	SO$_4{}^{2-}$	K$^+$
Content (mmol/L)	240	300	16.9	25.8	14.1	1.6

The densities and viscosities of the synthetic waters were measured at different temperatures of 30 – 80 °C for OPAW, 20 – 50 °C for BSW and distilled water (H$_2$O). The results are shown in figure 2.9. It is obvious that the water densities and viscosities decrease with increasing temperature. The viscosity of BSW is almost identical with that of H$_2$O in the test range but slightly lower than that of OPAW. The viscosities of BSW and H$_2$O are close to each other in the test range and can be extrapolated for high temperatures /UPC 15/ by

$$\mu_\mathrm{w} = A \, exp\left(\frac{B}{273.15+T}\right) \tag{2.3}$$

where μ_w is the dynamic viscosity of the water (Pa·s), T is the teperature (°C), and the parameters A = 2.05×10^{-6} Pa·s and B = 1805.5 K.
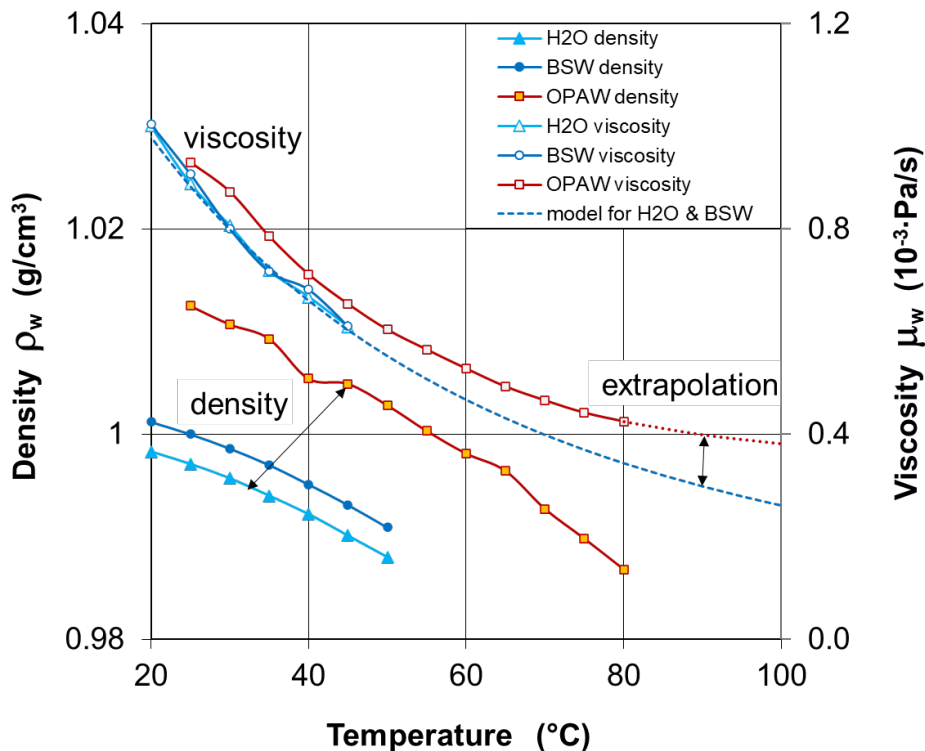
Fig. 2.9   Density and viscosity of the synthetic waters as a function of temperature

2.3.2   Test results

Evolution of swelling pressure with water uptake

During hydration, swelling pressure developed in each specimen, which was measured by a load cell installed between the upper piston and the top cap. Figures 2.10-12 show the evolution of water uptake and buildup of swelling pressure of the compacted bentonites GMZ01, GMZ02 and MX80 during infiltration of the synthetic Beishan groundwater (BSW). The specimens were pre-compacted to dry densities of 1.3 – 1.8 g/cm^3 at GMZ01, 1.5 – 1.8 g/cm^3 at GMZ02 and 1.4 – 1.8 g/cm^3 at MX80, respectively. The tests on each bentonite repeated in 3 – 4 groups to ensure the reliability of the measurements.
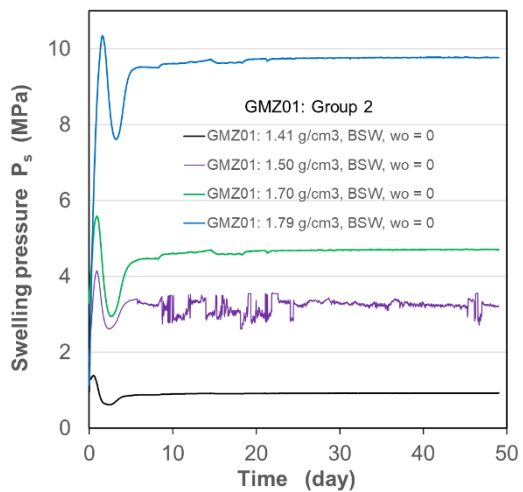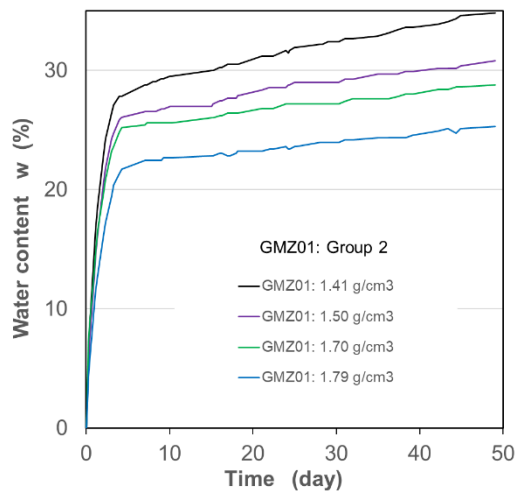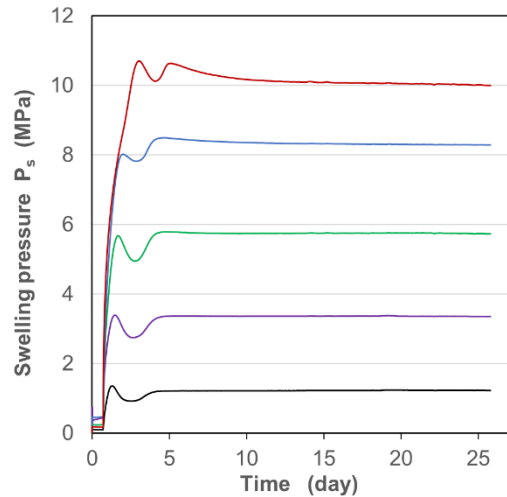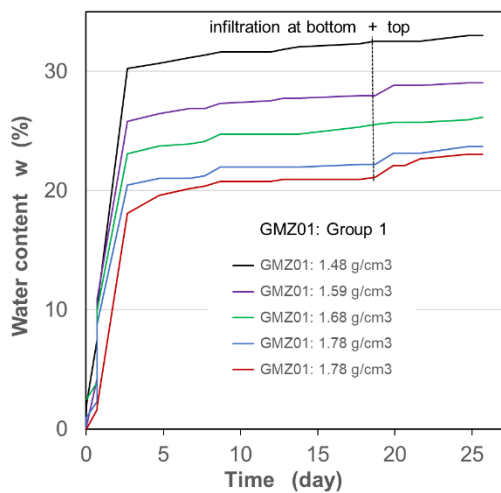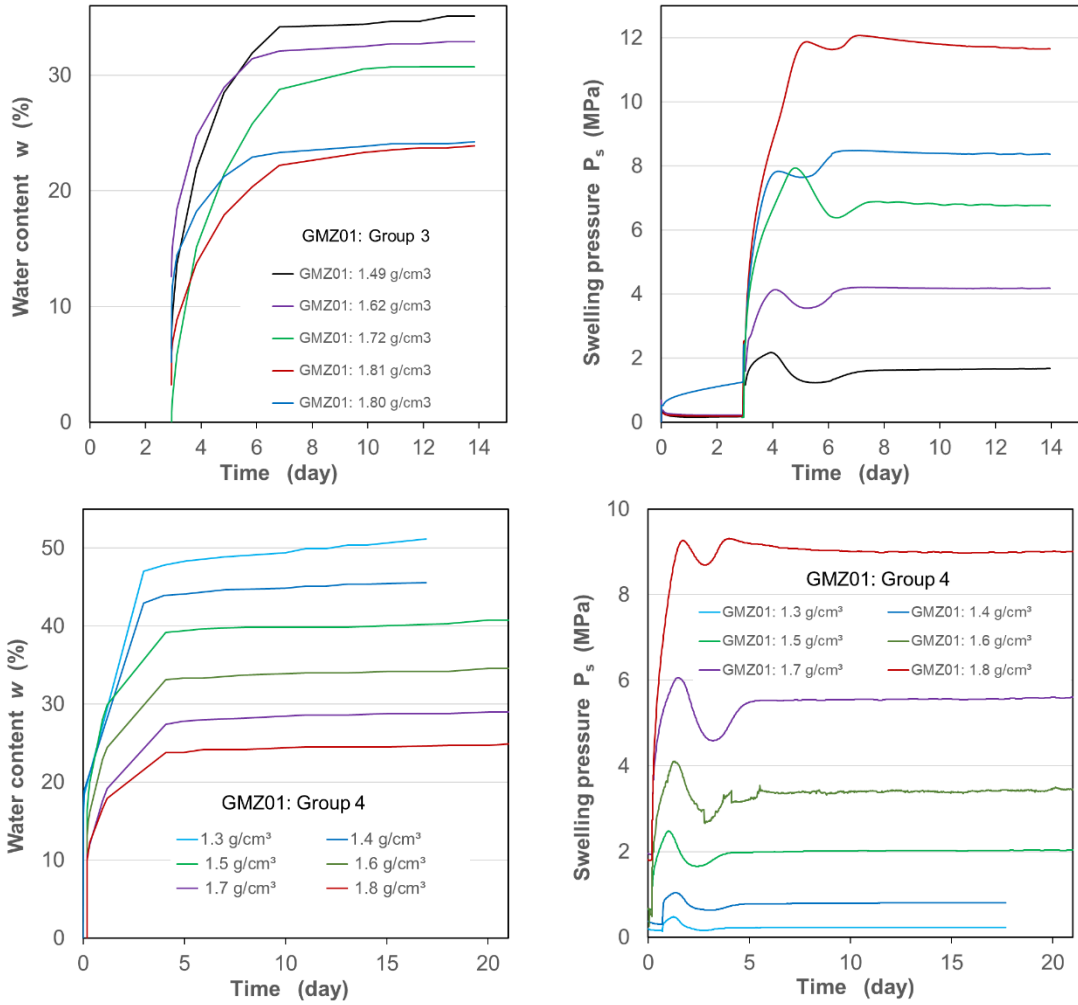
Fig. 2.10 Evolution of water uptake and build-up of swelling pressure obtained from the compacted bentonite GMZ01 in four groups
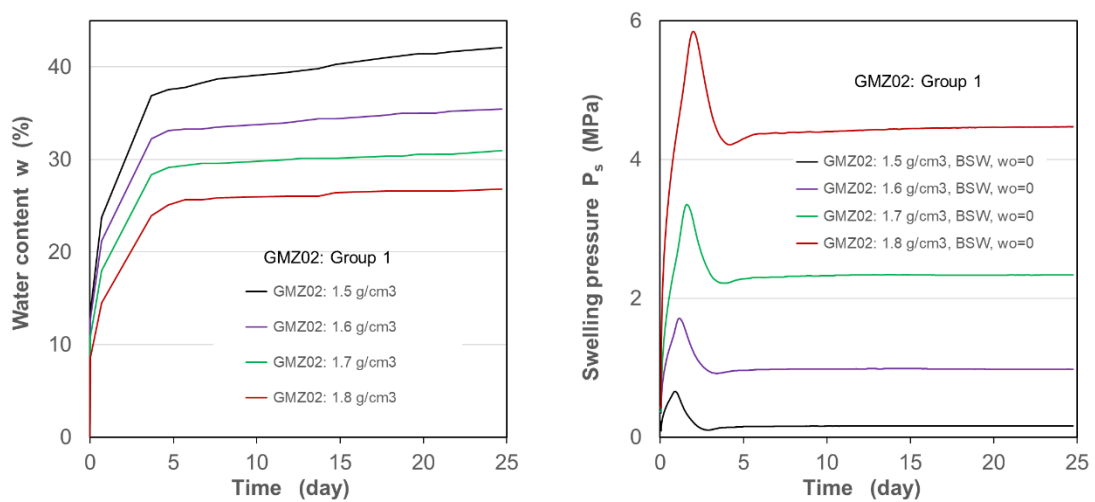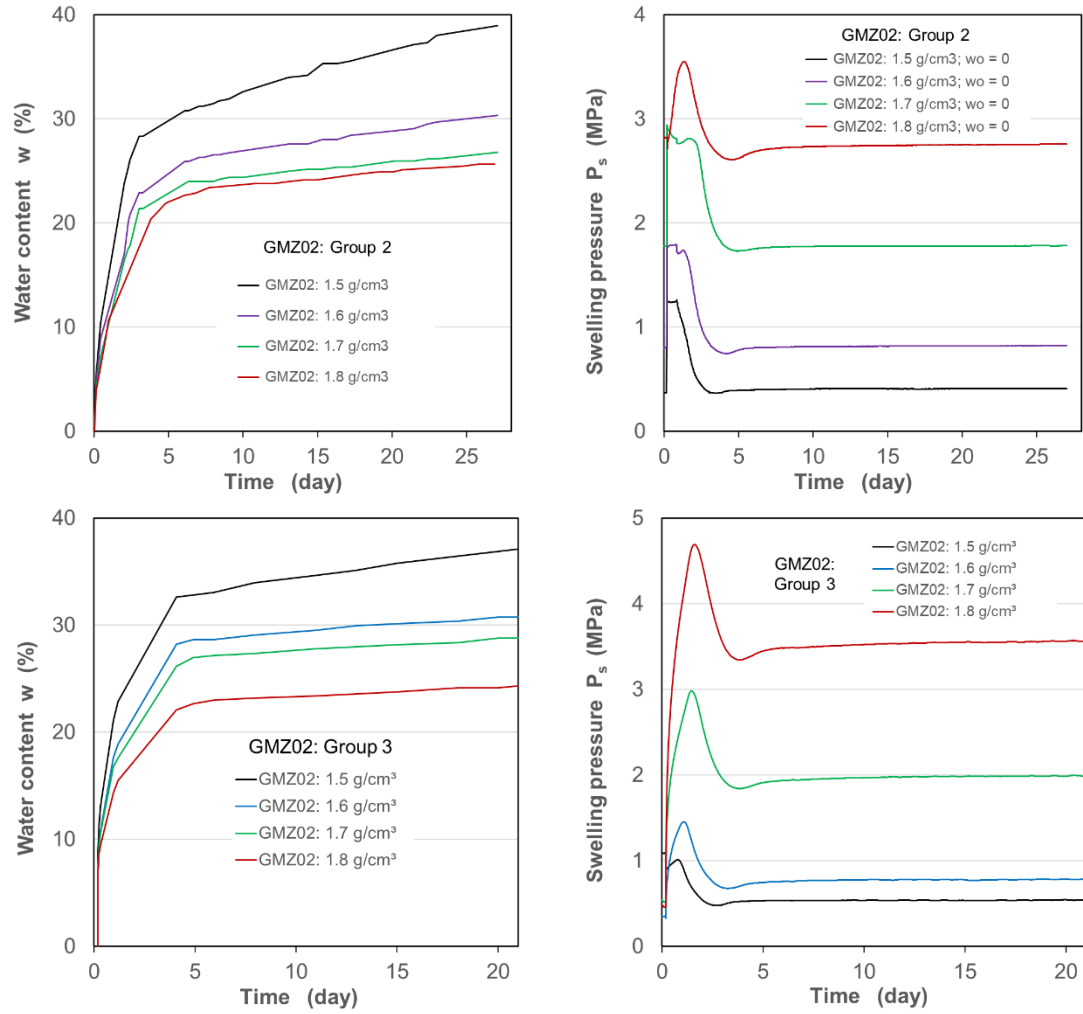
Fig. 2.11 Evolution of water uptake and build-up of swelling pressure obtained from the compacted bentonite GMZ02 in three groups
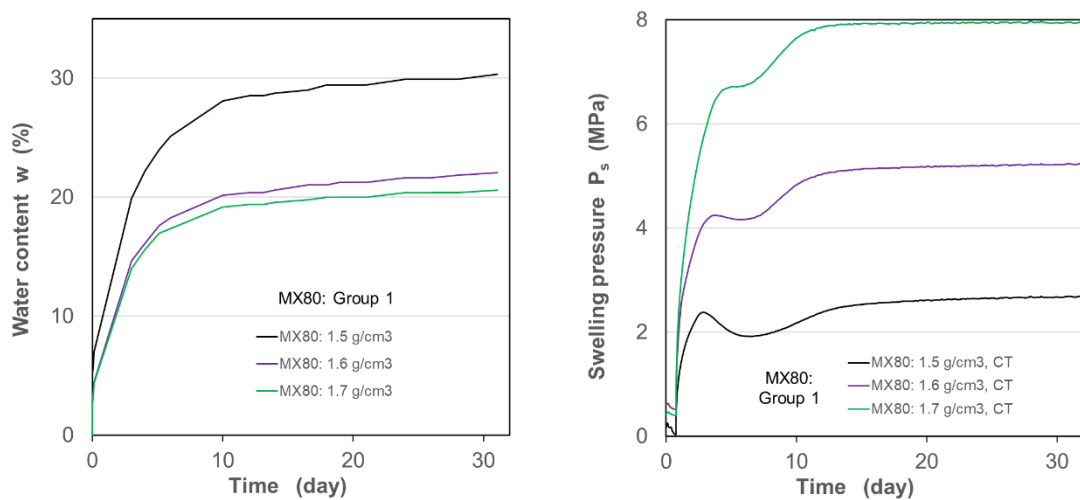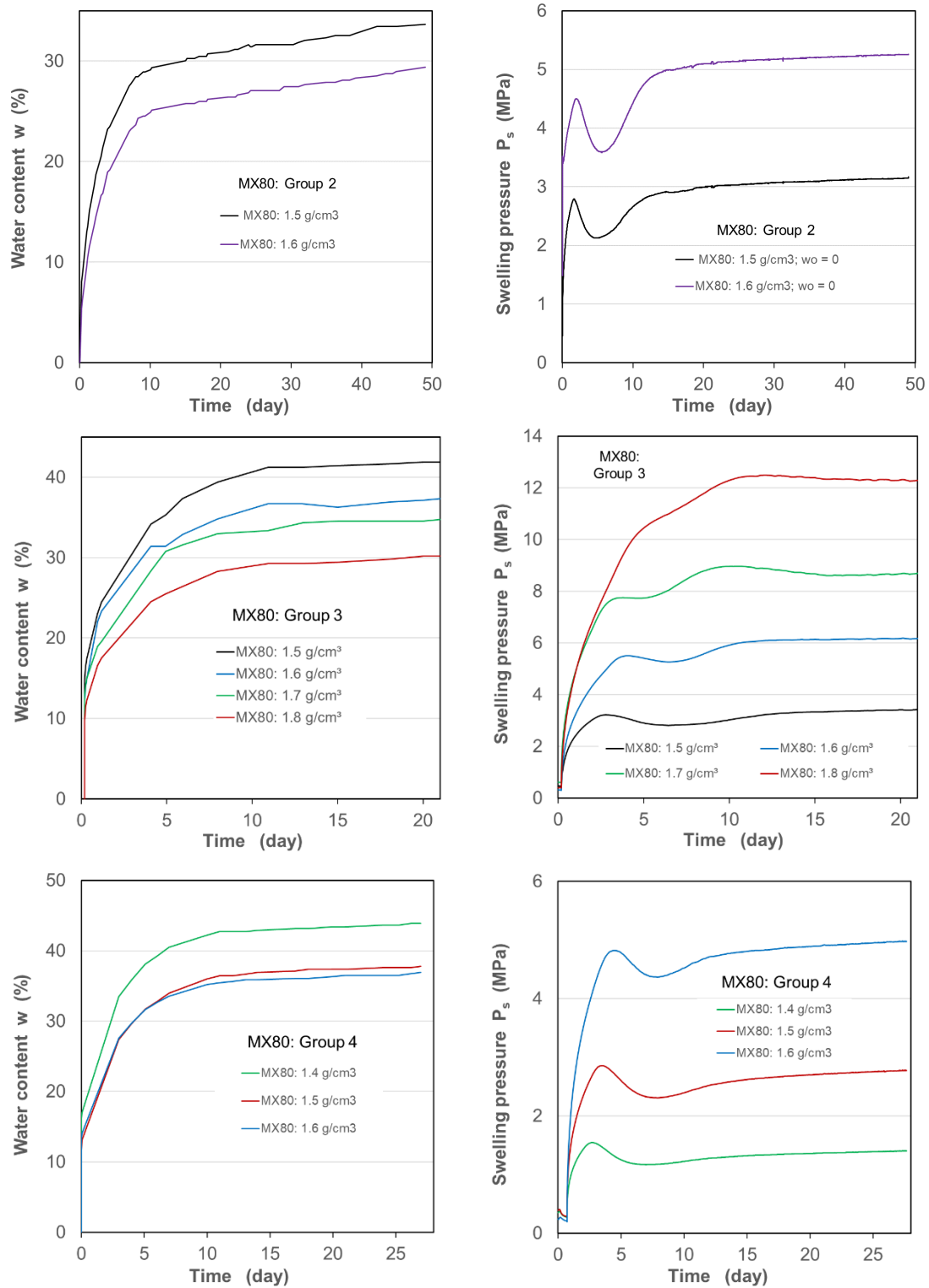
Fig. 2.12   Evolution of water uptake and build-up of swelling pressure obtained from the compacted bentonite MX80 in four groups

The results indicate that the water uptake was quickly in the first 3 – 5 days due to high suction effect and then slowed down with time to constant. Over two to three weeks, full saturation was reached at all the specimens, which was confirmed by measurement of their final water contents after testing. The saturated water content depends on dry density and montmorillonite content. Figure 2.13 illustrates the saturated water contents reached after the water infiltration over three weeks. It is obvious that the saturated water content of each bentonite increases linearly with decreasing dry density due to the increased pore space and with increasing montmorillonite content due to its high adsorption capacity.
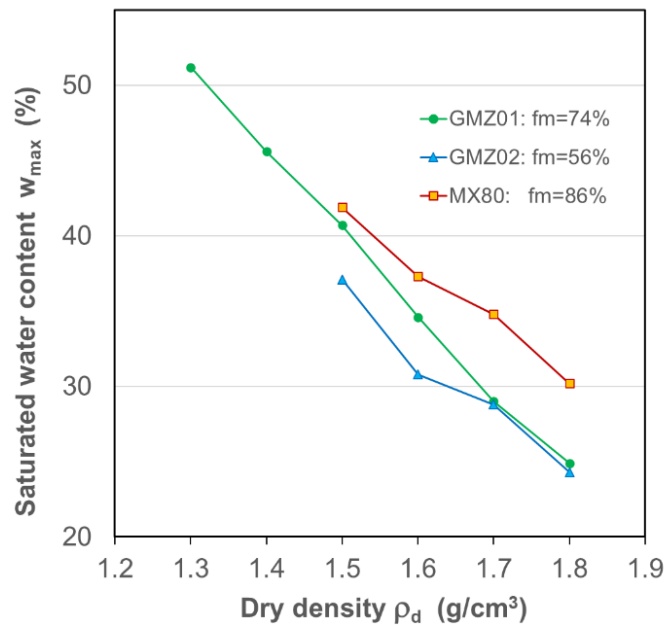
Fig. 2.13   Saturated water contents of the bentonites GMZ01, GMZ02 and MX80 as a function of dry density

In correspondence to the water uptake, swelling presssure built up in the bentonites under constraint volume conditions. All the compacted specimens exhibited a typical swelling pressure evolution with a double-peak shape (figures 2.10-12). Figure 2.14 also shows the water uptake and the induced swelling pressure of GMZ01 pellets with large voids, assembled blocks with a vertical gap, and pellets-blocks mixture.
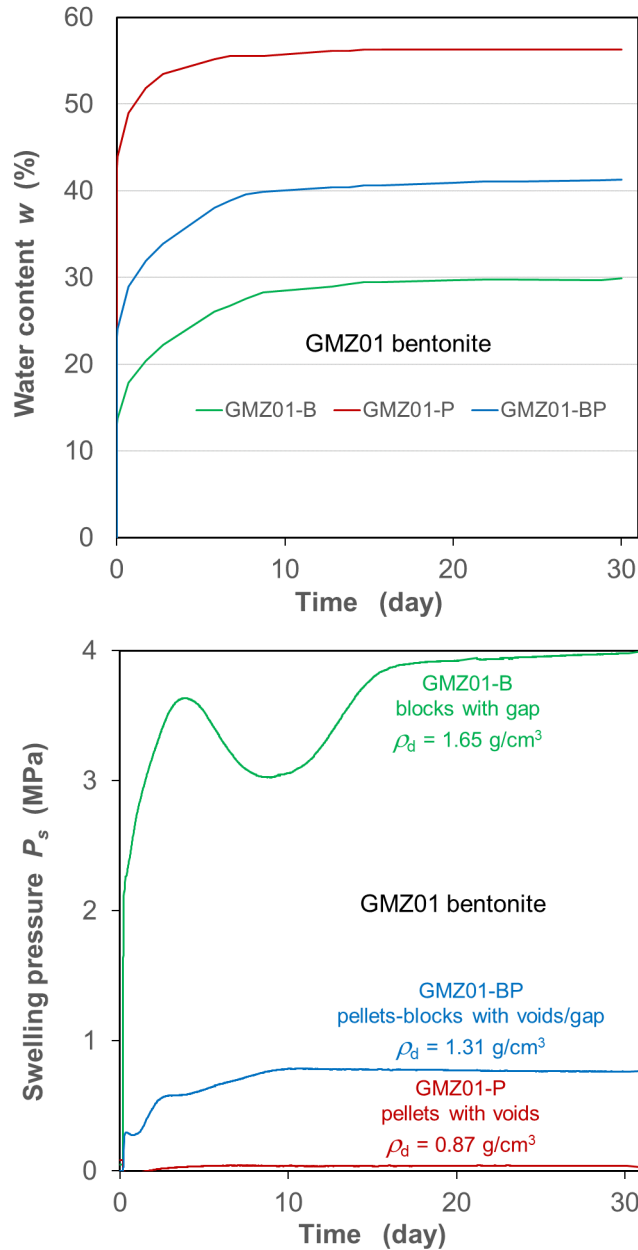
Fig. 2.14 Build-up of swelling pressure of the GMZ01 pellets, blocks and assembled pellets-blocks with large voids and gaps

It is obvious that all the specimens of the different bentonites with the different densities exhibited a double-peak shape of the swelling pressure evolution, independent of the initial inner structures (high homogeneity of compacted specimens or high heterogeneity of the loose pellets and assembled blocks). This is consistent with the observations by other researchers /PUS 90/IMB 06/ZHU 13/. Generally, the double-peak evolution is attributed to variations of micro- and macrostructures in compacted bentonite during saturation process. The initial increase in swelling pressure is a direct consequence of water uptake and associated expansion of montmorillonite interlayers (interlayer or crystalline

swelling pressure). The interlayer expansion also destabilizes the macrostructure between clay particles. As the local swelling pressure reaches the first peak, the macrostructure in the wetted area becomes weaker and breaks down, leading to a relaxation of the pressure. Simultaneously, the hydration in the electrical double layers between clay particles results in overlapping of thin water-films at narrow spaces and generates repulsive forces (double-layer swelling pressure). This increases the global swelling pressure again to a constant value as the bentonite is fully saturated. The swelling pressures at full saturation are higher than the first peaks at MX80 specimens but somewhat lower at GMZ01 and GMZ02, which is determined by the interlayer swelling pressure controlled by montmorillonite fraction.

Dependencies of swelling pressure on montmorillonite content and dry density

The final swelling pressures P_s of all the specimens are summarised in figure 2.15 as a function of dry density ρ_s together with some data from literature. The data indicate strong dependencies of the swelling pressure on the dry density ρ_d and the montmorillonite fraction f_m. Dixon et al. (2002) /DIX 02/ already introduced a so-called effective montmorillonite dry density (EMDD) for estimation of swelling pressure of bentonite-based materials. However, it seems to be very difficult for quantification of the associated parameters. Based on the present data, a simple model is here proposed

$$P_s = \alpha \times f_m^n \times exp(\beta \times \rho_d) \tag{2.4}$$

where α, β and n are the parameters. Fitting the present data from GMZ01, GMZ02 and MX80 specimens yields the parameter values of α = 0.0006 MPa, β = 6 cm³/g, and n = 3.7. The calculated model curves represent the mean lines through the scattered data for each kind of bentonite. Moreover, this model can also well match the swelling pressure-dry density curve for FEBEX bentonite with a montmorillonite fraction f_m = 90 % /VIL 10/. Additionally, the data obtained using the synthetic Beishan groundwater (BSW) for the hydration of the bentonites are consistent with those obtained using deionized water (H_2O) for GMZ01 /XU 17/ZHA 19/ and for MX80 /BUC 89/KAR 08/SEI 15/.

It is interesting to point out that the swelling pressure data obtained from GMZ01 pellets and blocks with the large voids/gaps are consistent with those of the compacted homogeneous specimens. This is the consequence of homogenization of the inner structure in the pellets and self-sealing of the gaps between the blocks due to the sufficient

swelling of clay particles with hydration. Figure 2.16 pictures the homogenized pellets and the sealed gap between blocks, compared with the initial states (figures 2.8b-c). Because of the low average dry density of the pellets, the large voids could not be completely sealed by the swelling of the clay particles. In contrast, the gap between the blocks could be completely sealed by the high swelling of the dense bentonite matrix.
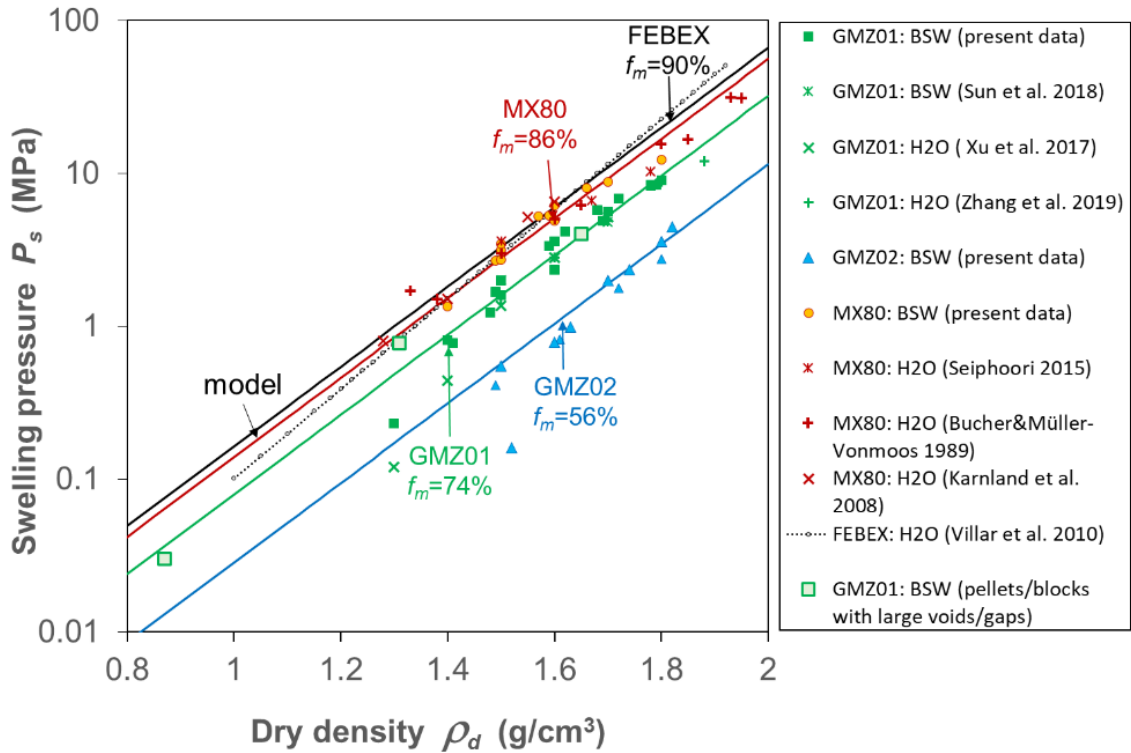
Fig. 2.15 Summarization of the swelling pressure data from the different bentonites (GMZ01, GMZ02, MX80, FEBEX) compared with the proposed model

(a) homogenized pellets (b) sealed gap between blocks

Fig. 2.16 Pictures of the homogenized pellets (a) and the self-sealed gap (initial width of 3 mm) between blocks (b) of GMZ01 bentonite over two months hydration

26

2.4 Water permeability

2.4.1 Test method

After full saturation of the specimens during the swelling pressure measurement, water permeability of each specimen was determined by injection of the synthetic groundwater (BSW) and measurement of water outflow using scaled burettes (accuracy of ±0.05 ml). The injection pressure was stepwise increased by means of the pump from 0.1 to 1.5 MPa, while the outlet pressure was kept at atmospheric. Each pressure step lasted over days to a month to reach steady-state flow. The corresponding hydraulic gradients across the specimen can be calculated by

$$i = \frac{P_w - P_o}{\rho_w \times g \times L}$$
(2.5)

where P_w and P_o are the up- and downstream water pressures (kPa), ρ_w is the water density (kg/m^3), g is the gravitational acceleration (9.81 m/s^2), and L is the specimen length (m). The calculated i – values vary in a range of 60 to 1000. The application of the different hydraulic gradients aimed at validating Darcy's law for the compacted bentonites. During steady-state flow, hydraulic conductivity K_h (m/s) and/or intrinsic water permeability K_w (m^2) can be determined according to Darcy's law /LIU 17/

$$K_h = \frac{v}{i} = \frac{Q_w \times \rho_w \times g \times L}{A \times (P_w - P_o)}$$
(2.6)

$$K_w = \frac{Q_w \times \mu_w \times L}{A \times (P_w - P_o)} = K_h \times \frac{\mu_w}{\rho_w \times g}$$
(2.7)

where v is the average velocity (m/s) of water flux Q_w (m^3/s) through the section A (m^2), μ_w is the dynamic viscosity of the water (1x10^{-3} Pa·s), P_w and P_o are the up- and downstream water pressures (Pa). The calculation indicates $K_w \approx 1\text{x}10^{-7} K_h$ for the synthetic water at the room temperature.

2.4.2 Test results

Figure 2.17 depicts water flow velocities v measured across the bentonite specimens at hydraulic gradients of $i = 60 - 1000$. At GMZ01 and GMZ02 specimens with dry densities of $\rho_d = 1.5 - 1.8$ g/cm^3, the flow velocity increases linearly with the hydraulic gradient and

27

the linear *v-i* lines pass through the origin of the coordinate system. This confirms Darcy's law for the compacted bentonites. In contrast, the *v-i* lines for MX80 specimens at ρ_d = 1.5 – 1.8 g/cm^3 are even though linear but do not pass through the origin of the coordinate system. The intersection of the line with *i* axis is the threshold gradient *I*, which are estimated for MX80 to be ~200 at ρ_d = 1.5 g/cm^3, ~150 at ρ_d = 1.6 g/cm^3 and ~300 at ρ_d = 1.8 g/cm^3 respectively. The high threshold gradients should be attributed to the immobile state of the strongly bound water in the dense bentonite with the high montmorillonite fraction (cf. figure 3). At low hydraulic gradients *i* < *I*, the bound water cannot be moved and any migration of solutes in the water is dominated by molecular diffusion. To move the bound water needs high hydraulic gradients to overcome the threshold, *i* > *I*.

The slope of the *v-i* line is equal to the hydraulic conductivity K_h (equation 2.6) and correspondingly, the water permeability K_w can be derived (equation 2.7). The measured K_w–data are summarized in figure 2.18 as a function of total porosity ϕ. Obviously, the permeability decreases with decreasing porosity and with increasing montmorillonite fraction, which can be approximately approached by

$$K_\mathrm{w} = \kappa \times (1 - f_m)^m \times exp(\omega \times \phi) \tag{2.8}$$

where K_wo, *m* and ω are the parameters. Fitting the data yields κ = 8x10^{-22} m^2, *m* = 3.2, and ω = 20. The calculated curves agree well with the data.

In fact, the water permeability is determined by effective porosity rather than total porosity. The effective porosity in bentonite is controlled by macropores occupied by free water and the interconnection of them, which are subjected to compression by swelling pressure. Therefore, the water permeability may be directly related to the swelling pressure, as shown in figure 2.19. For a given bentonite, the permeability decreases almost linearly with swelling pressure. Additionally, the permeability decreases with increasing montmorillonite fraction, which determines the fractions of free and bound pore water. The dependencies of water permeability on swelling pressure and montmorillonite fraction can be approached by

$$K_\mathrm{w} = \gamma \times (1 - f_m)^\eta \times P_s \tag{2.9}$$

where γ and η are the parameters. γ = 1.2x10^{-18} m^2 and η = 2 are determined based on the data. A reasonable agreement between the model and the data can be found.
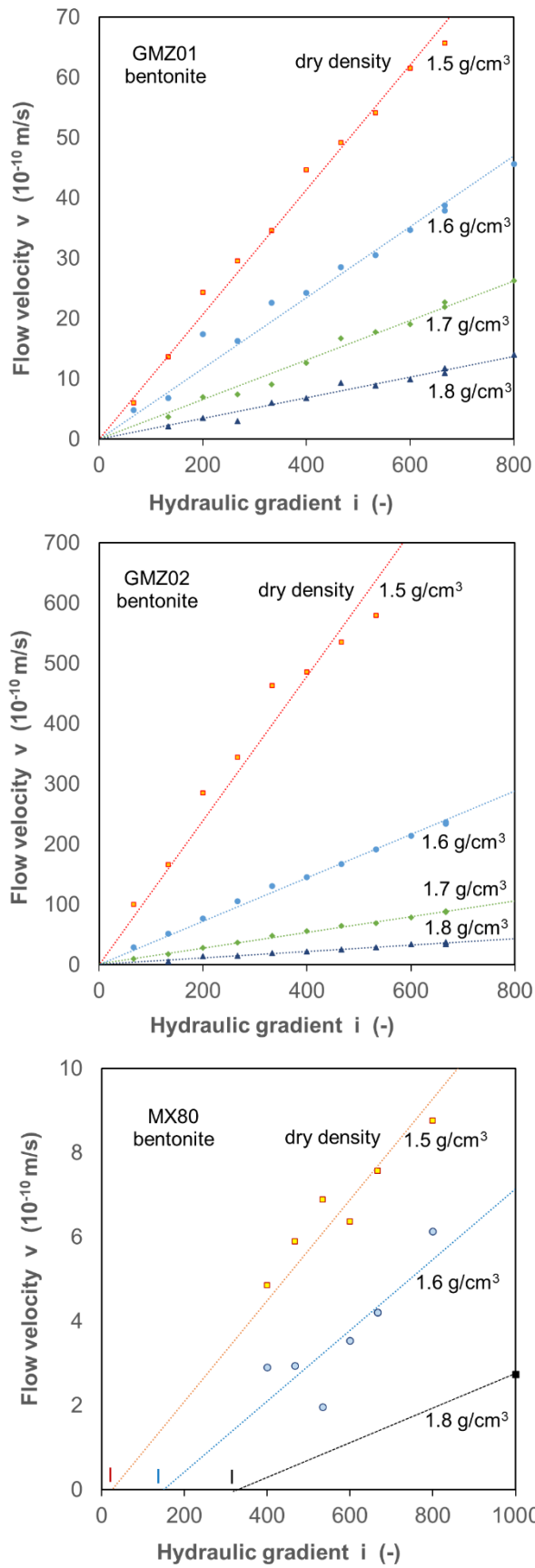
Fig. 2.17 Water flow velocities measured across the compacted bentonites GMZ01, GMZ02 and MX80 as a function of hydraulic gradient
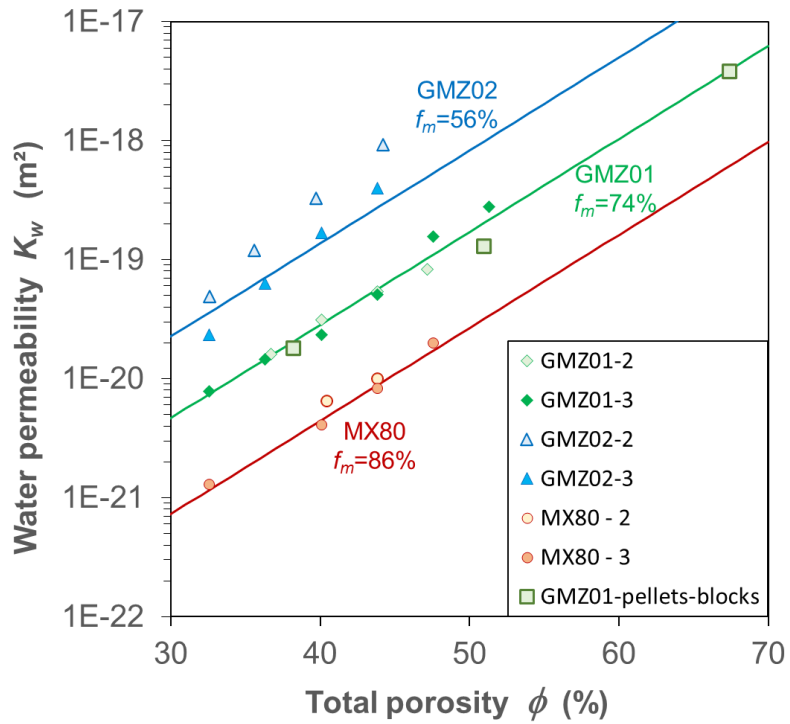
Fig. 2.18   Water permeability of the compacted bentonites as a function of total porosity and montmorillonite fraction
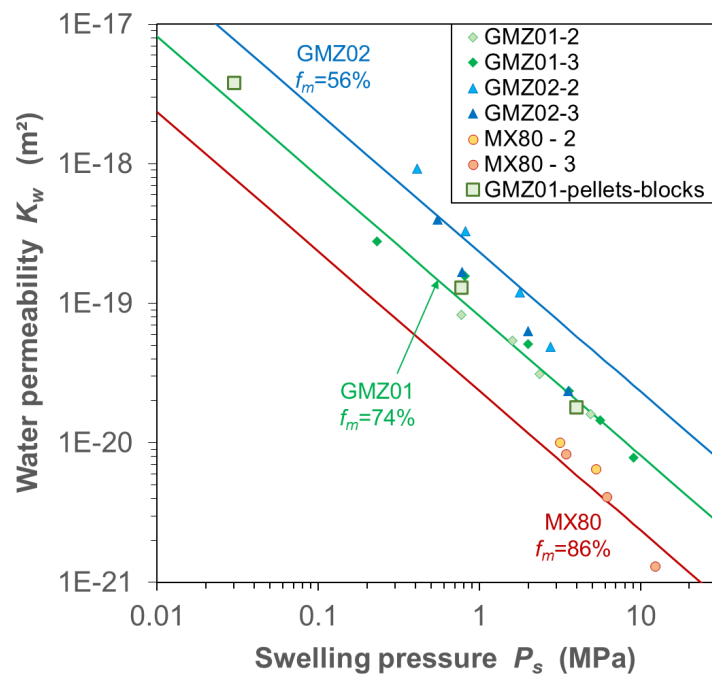
Fig. 2.19   Water permeability of the compacted bentonites as a function of swelling pressure and montmorillonite fraction

As mentioned earlier, the loose pellets and assembled blocks of GMZ01 bentonite became homogenized with swelling of the material. Even though some big voids remained in the pellets (figure 2.16a), the water permeability of the whole specimen maintained very low, which was in fact governed by the narrowed throats of the network rather than the remaining voids. Therefore, the permeabilities of the homogenized pellets and blocks are close to the fitting curve as those compacted specimens.

2.5   Gas penetration

2.5.1   Test method

After the measurement of water permeability mentioned above, the specimens were fully saturated, and some of them were directly used for further gas penetration testing under volume-constraint or flexible boundary conditions. Figure 2.20 shows the test layout, setup, and volume-constraint condition as well. A syringe pump (Model 260D) was applied for gas injection, which allows a maximum volume of 260 mL, a maximum pressure of 500 bar and flow rates in a range of 1 μL/min to 100 mL/min. Before testing, the water remaining in the inlet and outlet reservoirs was removed by vacuum pumping. Helium gas was then injected to the specimens at controlled flow rates of 0.02 – 0.2 ml/min, while gas outflow was accumulated in a steel vessel with a volume of 380 ml. Gas pressures in the up- and downstream were monitored by pressure transducers. Stress reaction was recorded by the load cell at the opposite side.

Another setup with three coupled triaxial cells was developed and used for the gas testing under flexible boundary conditions. Figure 2.21 illustrates the test system. The setup allows parallel gas testing on three specimens under identical conditions. The water-saturated specimens were installed in rubber jackets and covered with sintered porous discs of 50 mm diameter at the top and 25 mm diameter at the bottom. The smaller injection area at the bottom was selected to avoid possible flow along the interface between the specimen and the jacket. These specimens were loaded at constant axial and radial stresses controlled by two respective syringe pumps. Helium gas was injected by means of another pump with a maximum volume of 1000 mL at controlled flow rates in a range of 0.05 – 0.2 mL/min. Gas outflow was accumulated in a pressure vessel with a volume of 3600 mL. Gas pressures in the upstream and downstream were monitored during the injection. During the gas injection, axial deformation (ε_a) was recorded by a

linear variable differential transducer (LVDT) installed outside the cell, while radial strain (ε_r) was measured by a circumferential extensometer mounted around the sample outside the jacket. The volumetric strain is obtained approximately by $\varepsilon_v = \varepsilon_a + 2\varepsilon_r$.

The gas injection lasted for sufficient time periods to examine long-term gas flow process and to determine gas breakthrough pressure and permeability. The gas outflow rate can be estimated from the pressure difference across the specimen with elapsed time (Gutiérrez-Rodrigo et al., 2021)

$$Q_g = V_g \times \frac{P_g - P_o}{P_m} \times \frac{1}{\Delta t} \tag{2.10}$$

where Q_g is the mean gas flux (m³/s), V_g is the volume of the outlet reservoir (m³), P_g and P_o are the in- and outlet gas pressures (Pa), $P_m = (P_g + P_o)/2$ is the average gas pressure (Pa) between the time interval Δt (s) for the measurement. Effective gas permeability K_g (m²) is then estimated by Darcy's law:

$$K_g = \frac{2 \times Q_g \times \mu_g \times P_o \times L}{A \times \left(P_g^2 - P_o^2 \right)} \tag{2.11}$$

where μ_g is the dynamic viscosity of helium gas (1.96x10⁻⁵ Pa·s).
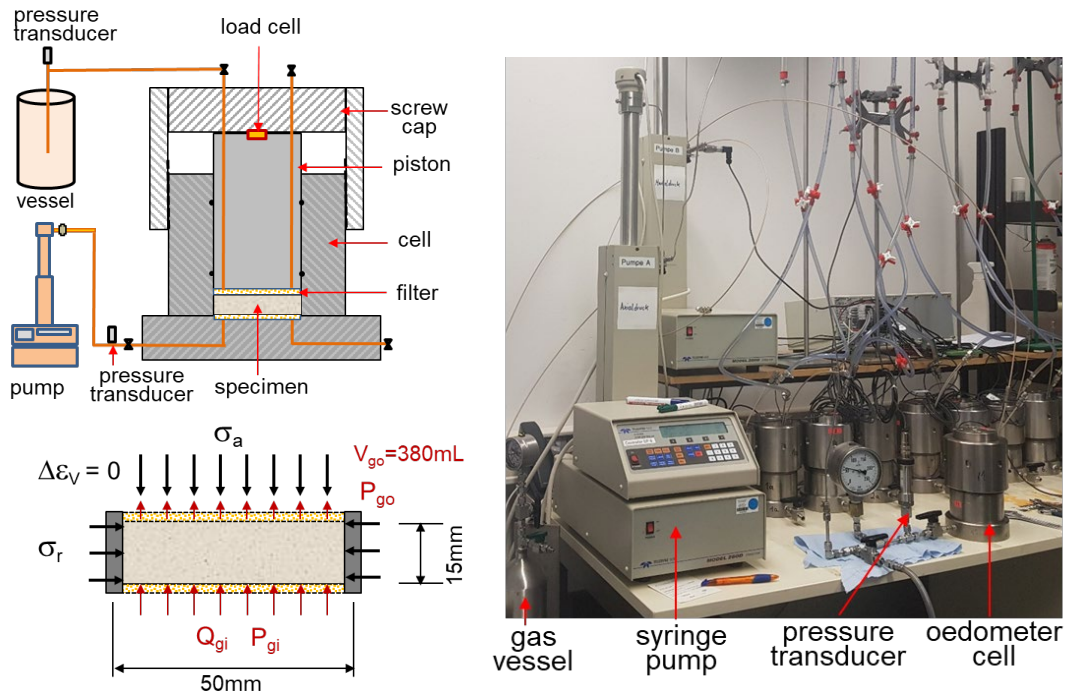
Fig. 2.20   Setup of the gas penetration testing under constant volume
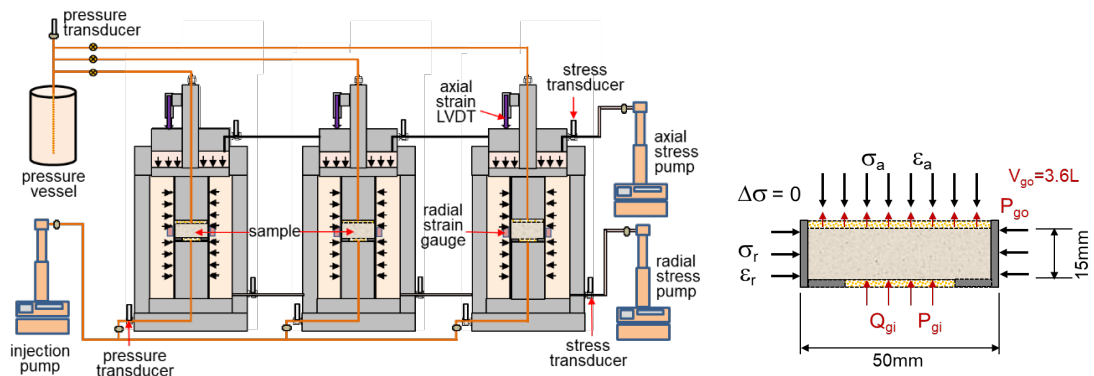
Fig. 2.21   Setup of the gas penetration testing on three parallel specimens in coupled triaxial cells

2.5.2   Test results

Under volume-constraint conditions

Totally, ten water-saturated specimens were selected for gas penetration testing under volume-constraint conditions. Their initial characteristics are given in table 2.9 in terms of dry density, water permeability and swelling pressure. The swelling pressure is equivalent to the initial total stress before gas injection. Test results are illustrated in figure 2.22 for the compacted specimens and in figure 2.23 for the pellets and blocks with large voids/gaps in terms of applied gas flow rate (Q_g), induced up- and downstream pressures (P_g, P_o), axial total stress (σ_a), and outflow rate (Q_o) versus elapsed time. It is evident that the gas penetration process was quantitatively different in each specimen due to the different material properties and gas injection rates, but qualitatively quite similar with multiple gas breakthrough events and unstable post-breakthrough flow.

Tab. 2.9   Initial properties of the water-saturated bentonite specimens for gas testing

Specimens	Dry density (g/cm^3)	Water permeability (m^2)	Swelling pressure (MPa)
GMZ01-1	1.4	8×10^{-20}	0.8
GMZ01-2	1.5	5×10^{-20}	2.0
GMZ01-3a	1.6	2×10^{-20}	3.6
GMZ01-3b	1.6	2×10^{-20}	3.0
GMZ01-4	1.7	1×10^{-20}	5.6
GMZ02-1	1.5	4×10^{-19}	0.6
MX80-1	1.4	2×10^{-20}	1.0
GMZ01-P	0.87	4×10^{-18}	0.03
GMZ01-B	1.65	2×10^{-20}	3.3
GMZ01-BP	1.31	1×10^{-19}	0.77

P: homogenized pellets;
B: sealed blocks;
BP: sealed pellets-blocks mixture (figure 2.16)

Gas breakthrough pressure

The gas injection at the controlled flow rates led to a gradual build-up of the upstream pressure, accompanied by an increase of the total stress over the initial swelling pressure. This implies that the water-saturated bentonites were gas tight and subjected to compression by the gas pressure against the rigid boundary. As a peak pressure P_{gb} was reached, gas breakthrough occurred, yielding a rapid gas release and hence a rapid drop of the upstream pressure as well as a rapid rise of the downstream backpressure. When the upstream pressure dropped down to a minimum value P_{gc} and the backpressure P_o became constant, the gas flow ceased due to self-sealing of the pathways. The upper peak P_{gb} is usually defined as the gas breakthrough pressure, whereas the lower peak P_{gc} is referred here as the gas seal pressure. In correspondence to the drop of the gas pressure from P_{gb} to P_{gc}, the total stress decreased from σ_{ab} to σ_{ac}. The gas breakthrough and seal pressures are depicted in figure 2.24a as a function of the total stress.
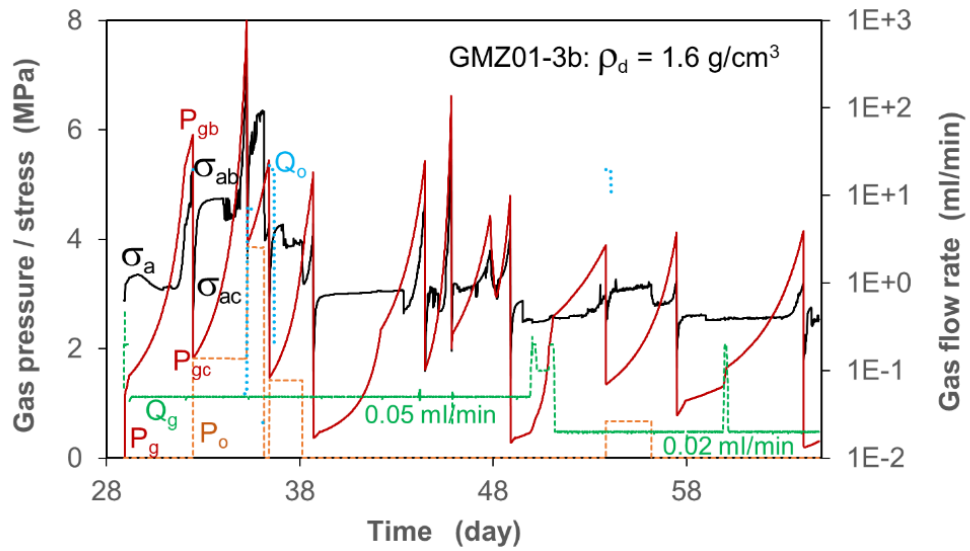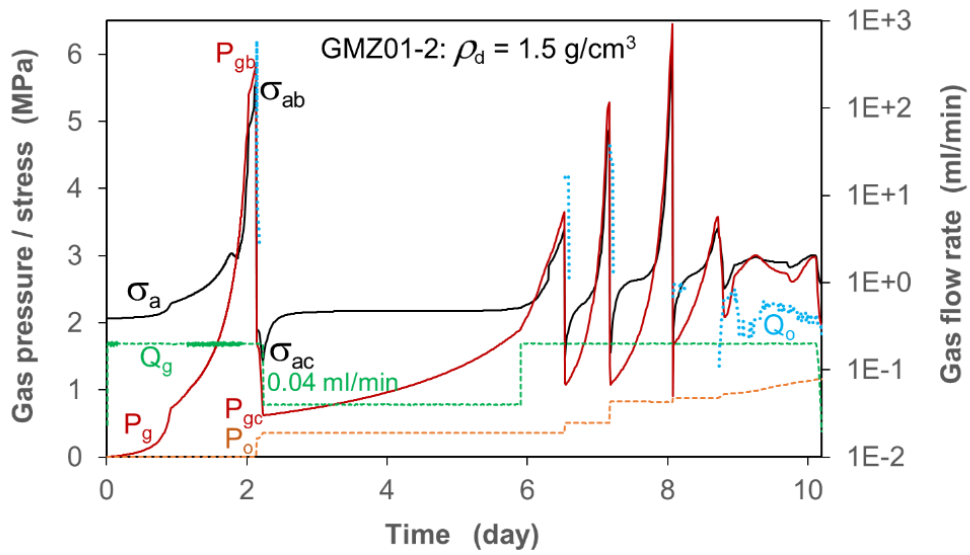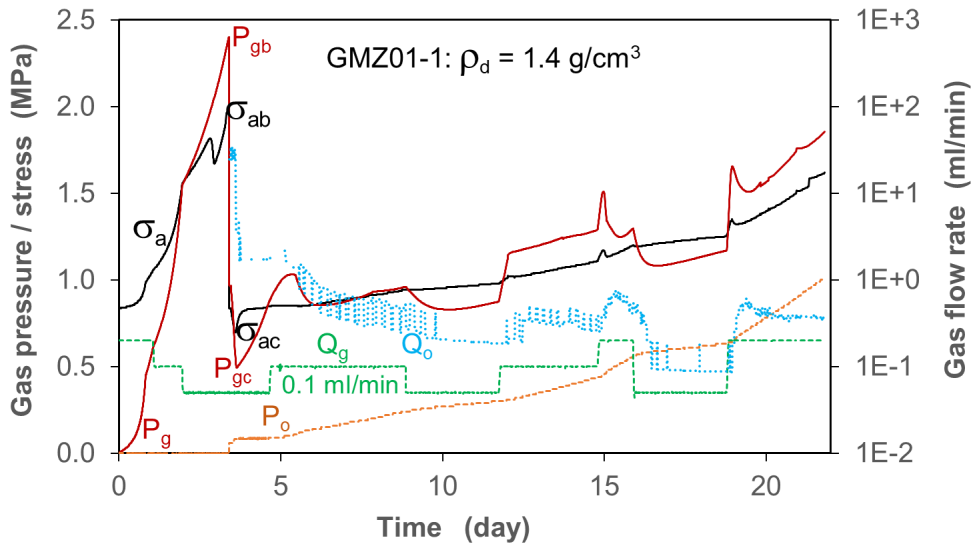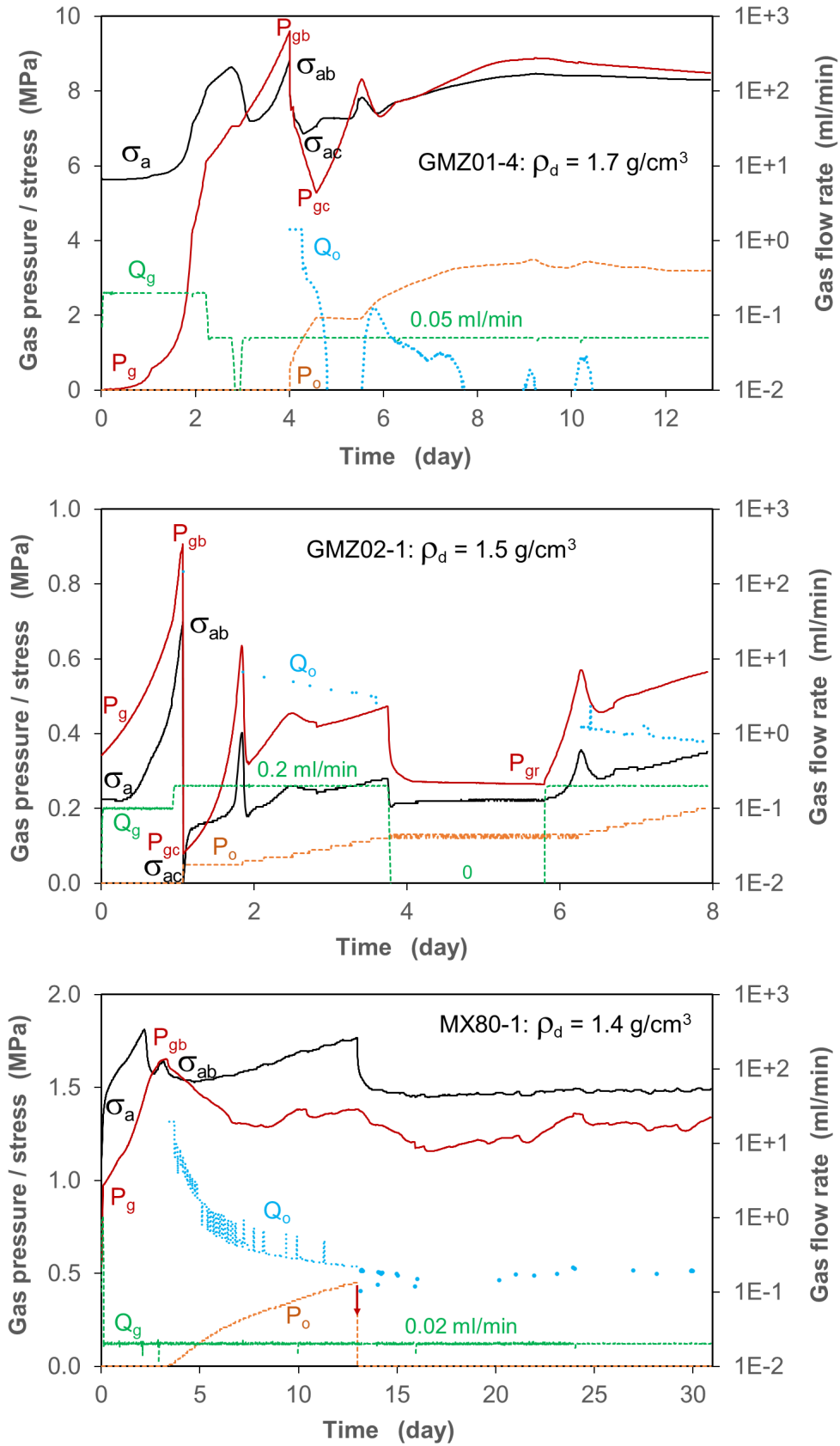
Fig. 2.22 Gas penetration processes in the water-saturated and compacted bentonites under volume-constraint conditions

36
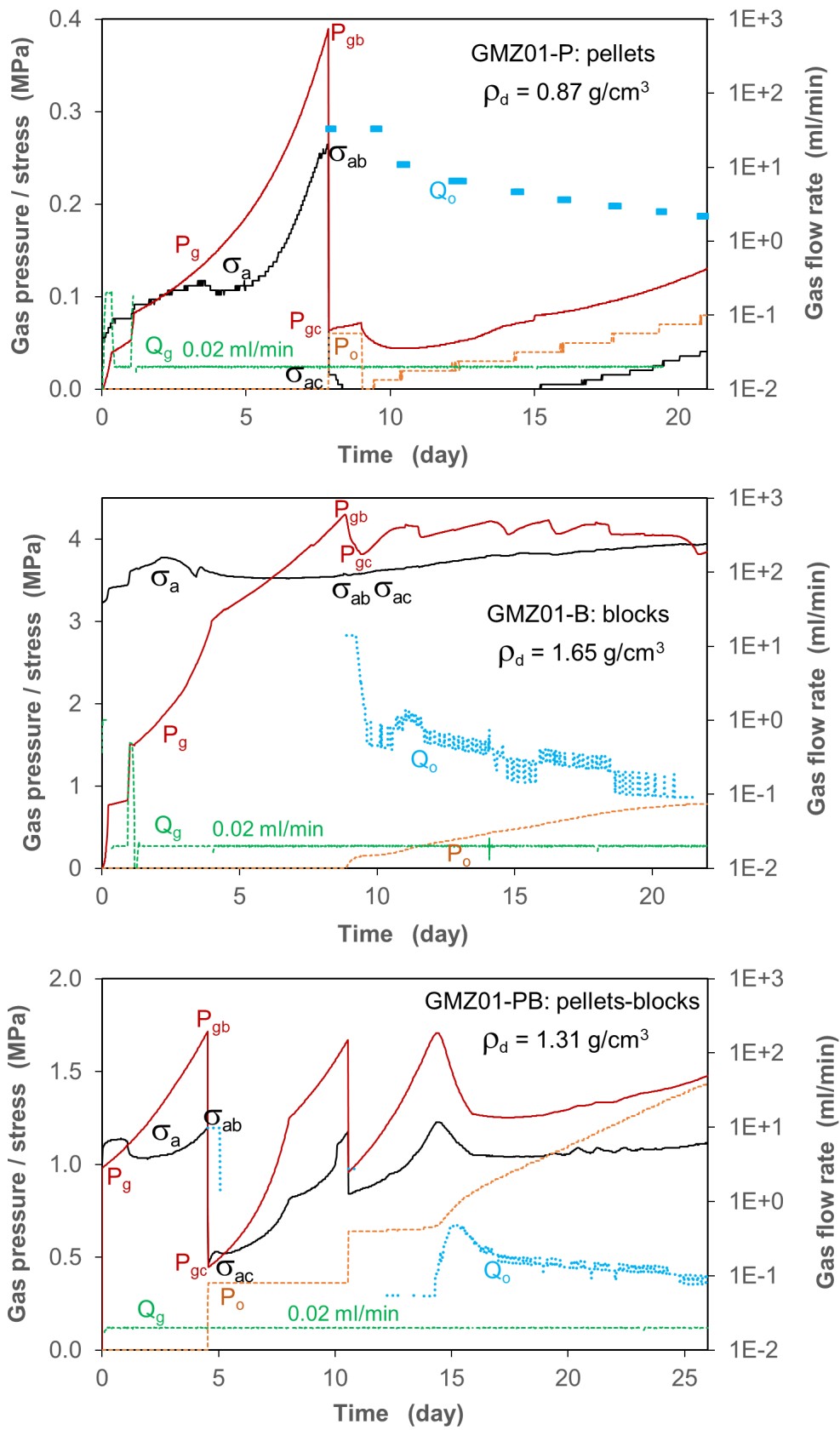
Fig. 2.23   Gas penetration processes in the water-saturated pellets and blocks of GMZ01 bentonite under volume-constraint conditions

Extensive investigations /PUS 87/HOR 96/ROD 99/SEL 14/HAR 17/LEV 20/ suggested that gas entry and penetration in water-saturated bentonite is governed by dilating pores locally in weak regions to form micro-fissures, which needs high gas pressures exceeding the sum of the minor principal stress and tensile strength of the material. This can be expressed as

$$P_{gb} \geq \sigma_{min} + \sigma_T \tag{2.12a}$$

where σ_{min} is the minor principal stress and σ_T is the tensile strength of the material. In case of the oedometer conditions (figure 2.20), the radial stress should be the minor one $\sigma_r = \sigma_{min}$ and nearly equal to the axial one, $\sigma_r = \sigma_{min} \approx \sigma_a$. Thus equation (2.12a) can be rewritten by

$$P_{gb} \geq \sigma_{rb} + \sigma_T \approx \sigma_{ab} + \sigma_T \tag{2.12b}$$

The tensile strength can be estimated by $\sigma_T = P_{gb} - \sigma_{ab}$ and assumed here to be related linearly with the total stress, $\sigma_T = b \times \sigma_{ab}$. Thus, equation (2.12b) can be expressed by

$$P_{\mathrm{gb}} \geq (1 + b) \times \sigma_{ab} \tag{2.12c}$$

The parameter $b = 0.09$ is obtained based on the measured data. Figure 2.24a shows the lower boundary for the gas penetration through the bentonites, $P_{\mathrm{gb}} = \sigma_{ab} + \sigma_T$, which fits the data from the different bentonites (GMZ01, GMZ02, MX80) with the different initial conditions. This model can also match the data from literature (figure 2.24b) obtained on MX80 bentonite from normally sized specimens /GRA 16/HAR 17/ and from a full-scale in-situ experiment Lasgit /CUS 14/ during slow gas injection. It is to be noted that this gas breakthrough criterium is adequate for volume-constraint conditions. If the boundary is not rigid, the specimen can deform with gas pressure to dilate pores to formulation of local micro-fissures at relatively low pressures. As observed on MX80 bentonite in oedometer cell under controlled axial load /ZHA 21/ and on GMZ01 bentonite under isostatic load /CUI 21/, the gas breakthrough occurred at pressures somewhat below the confining stresses. This is also confirmed by our new experiments under triaxial stress conditions as shown later in the following section.
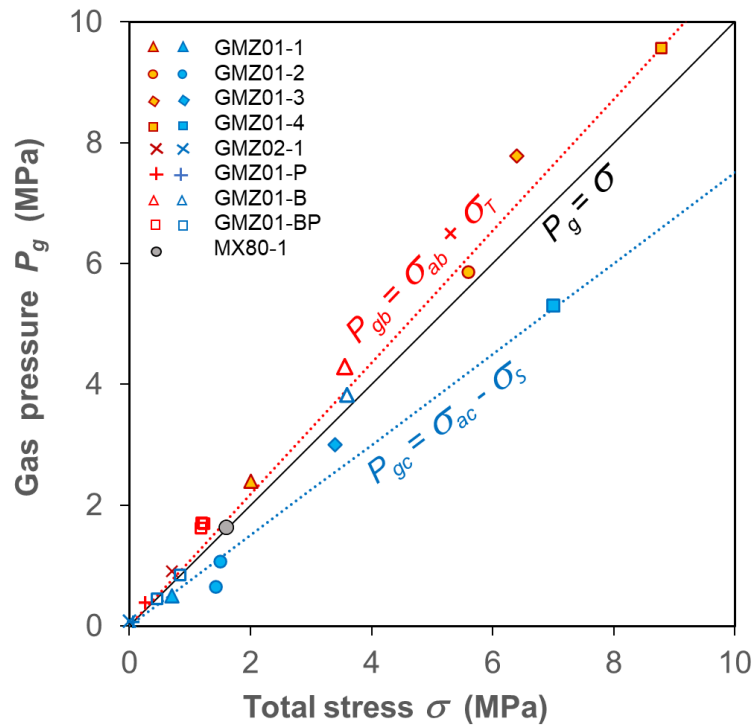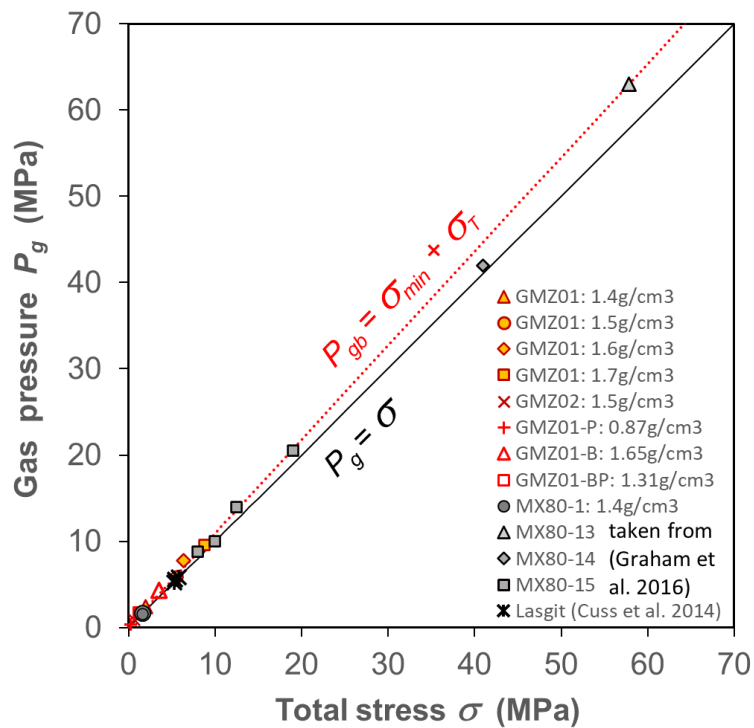
Fig. 2.24 Relationships of gas breakthrough and seal pressures with total stress obtained from GMZ01, GMZ02 and MX80 bentonites (a) and compared with the other data from small-scale specimens and full-scale buffer of MX80 bentonite

In contrast to the gas breakthrough pressure, the measured gas seal pressures P_{gc} are mostly lower than the associated total stresses σ_{ac}. A gas seal criterium may be formulated as

$$P_{\text{gc}} \leq \sigma_{ac} - \sigma_S = (1-c) \times \sigma_{ac} \qquad (2.13)$$

where σ_S is the minimum stress required to seal the gas pathways. $\sigma_S = c \times \sigma_{ac}$ is assumed with an estimated parameter c = 0.3. The line $P_{\text{gc}} = \sigma_{ac} - \sigma_S$ in figure 24a is the upper boundary, below which the pathway network is disconnected.

The gas breakthrough pressure is determined by many factors, particularly by the mineralogical composition and dry density of bentonite. Figure 2.25 summarises the present data together with those from literature /PUS 87/XU 17/GUT 21/. It shows that the gas breakthrough pressure of each bentonite increases exponentially with increasing dry density. The differences of the breakthrough pressures between the different bentonites might be attributed to the different fractions of montmorillonite, which determine the proportions of bound and free pore water, effective pore space and interconnection of them for gas flow. Unfortunately, the features of the internal structure of a bentonite could not be clearly identified from the tests. From the figure one can also find out that at a given dry density, the gas breakthrough pressures of GMZ01 pellets and blocks with the initial large voids/gaps are somewhat lower than those of the compacted homogenous specimens. That implies that the engineered voids and gaps in the bentonite buffer can serve as preferential gas pathways even though highly sealed.

Gas post-breakthrough flow

Following the first gas breakthrough/sealing event, further gas injection caused more cyclic rising/dropping of the upstream pressure, reflecting opening/closing cycles of the pathway network. The temporal disconnections of the network tended to disappear with time and followed by a continual gas flow, as shown by most of the specimens (except for GMZ01-3b). In the closed system, the backpressure on the specimen increased with the accumulation of the flowing gas, leading to an increase in average pore pressure (P_{gp} = (P_{g} + P_{o})/2). The increased pore gas pressures could keep and enlarge the pathway for a continual gas flow. However, the gas flow rate varied with changes of the pathway features (aperture, connectivity, etc.) under changes in pressure gradient or difference ($\varDelta P_{\text{g}}$ = P_{g} - P_{o}).
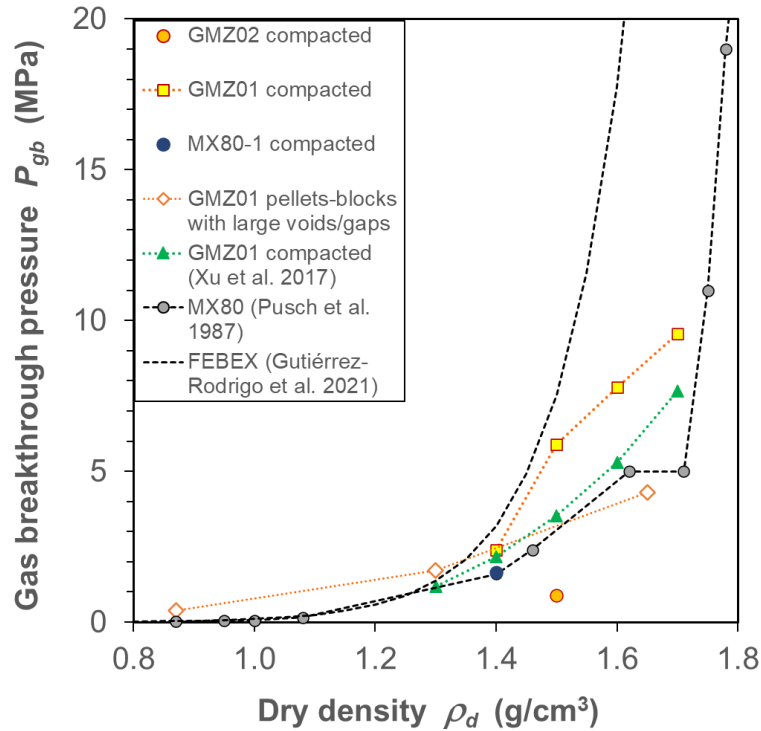
Fig. 2.25 Gas breakthrough pressures of the different bentonites as a function of dry density

When the backpressure was kept constant at atmospheric, specimen GMZ01-3b showed multiple breakthrough/sealing events without continual gas flowing through over a month. In contrast, specimen MX80-1 showed a continual gas flow with varied upstream pressures and flow rates. It seemed that the swelling capacity of the bentonite at the low dry density (1.4 g/cm^3) was not high enough to close the network.

As the gas injection was stopped at specimen GMZ02-1, the upstream pressure fell quickly within a short time and then declined to a lowest constant value P_{gr}, which is referred as the shut-in pressure and/or as the minimum internal gas pressure capable of maintaining the network /HOR 96/ROD 99/. Reopening the pathway for gas flow needs overpressures.

Effective gas permeability K_g was determined from the data of gas outflow Q_o for each specimen. Figure 2.26 shows some typical evolutions of gas permeability with variation of effective stress ($\sigma_{eff} = \sigma - P_{gp}$). It is obvious that the gas permeability in log (K_g) varies inversely with the periodic variation of the effective stress. In fact, the effective stress controls the geometric features of the network (aperture, connectivity, etc.) and thus the permeability. At specimen MX80-1, a rapid reduction in gas permeability was resulted from a high peak stress caused by dropping the backpressure (cf. figure 2.22).

41

Final K_g-values obtained at the end of each test are illustrated in figure 2.27 as a function of effective stress, which can be approximately approached by

$$K_g = K_{go} \times exp\left(-\xi \times \sigma_{eff}\right) \qquad (2.14)$$

where K_{go} is the gas permeability at $\sigma_{eff} = 0$ and ξ is a parameter. Fitting the data yields $K_{go} = 7\times10^{-17}$ m^2 and $\xi = 4$, with which the model curve matches the data well.
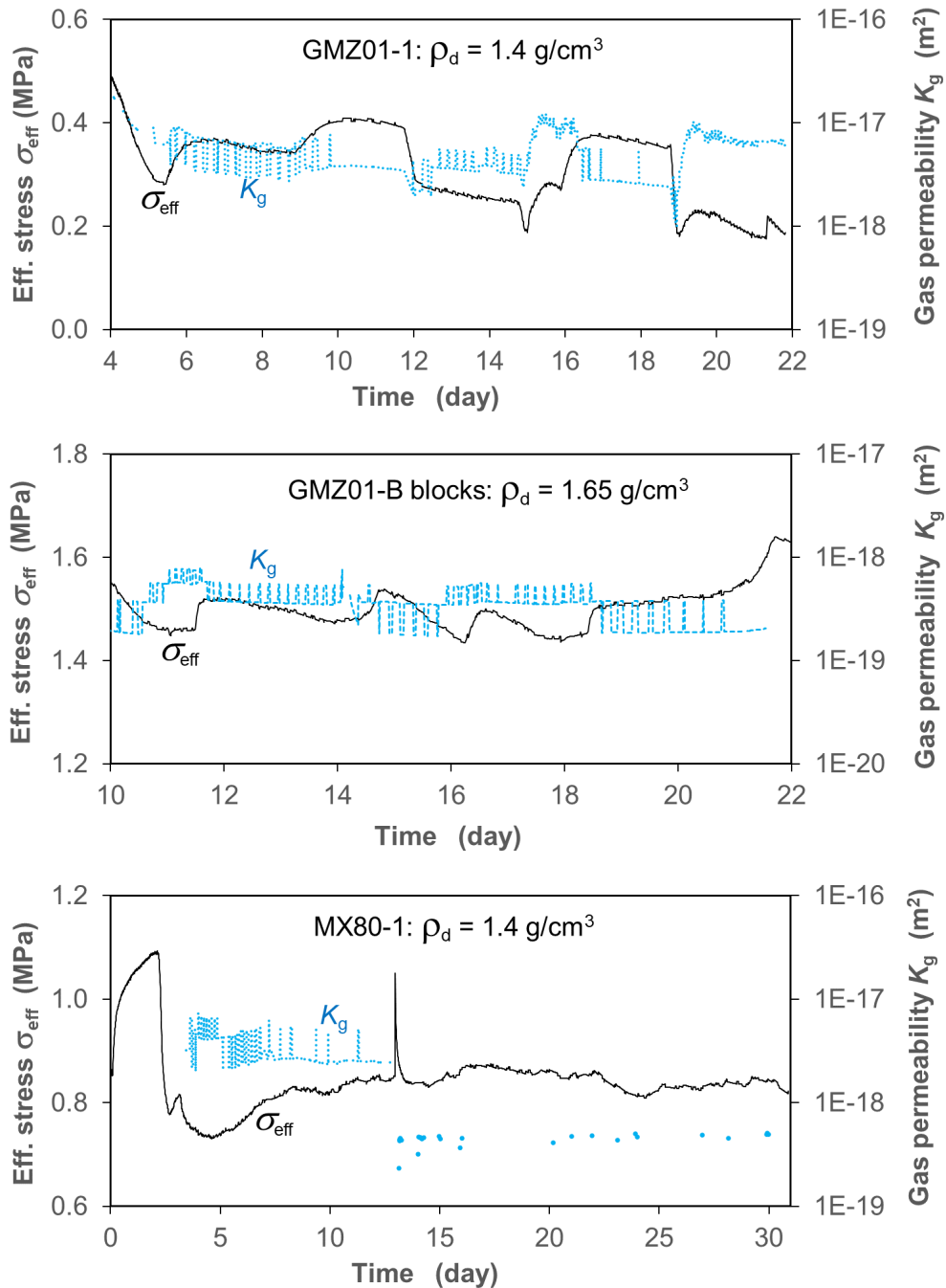
Fig. 2.26 Evolution of gas permeability in correspondence to variation of effective stress

42
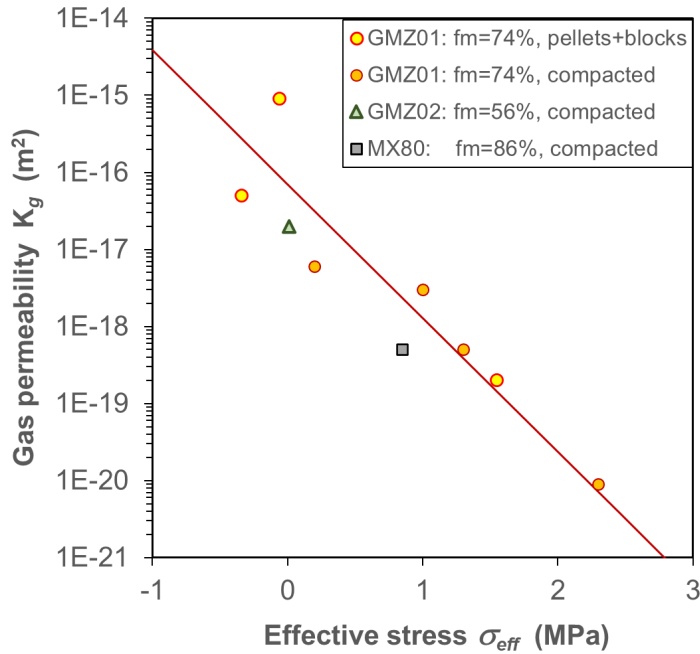
Fig. 2.27   Gas permeability of the compacted bentonites as a function of effective stress

After testing, the residual water content was determined on each specimen (table 2.10). Most of the tested specimens showed the full saturation after gas flowing through, except for the pellets and pellets-blocks mixture. The full saturation implies that no or negligible amount of pore water were displaced out of the specimens by gas injection and the gas entry/penetration was caused by gas pressure-driven dilatancy and creation of micro-fissures. In contrast, the desaturation of the pellets indicates that the water in some re-maining large voids (figure 2.16a) was moved out of the pores by gas pressure.

Under triaxial stress conditions

Gas penetration behaviour of the water-saturated bentonites GMZ01 and GMZ02 was also examined under triaxial stress conditions. Three specimens were taken from the oedometer cells (figure 2.20) and then installed in the triaxial cells (figure 2.21). Their initial characteristics are given in table 2.11. GMZ01 specimens S1 and S2 had the initial dry densities of ρ_d = 1.3 and 1.4 g/cm³ respectively, while GMZ02 specimen S3 is rela-tively denser at ρ_d = 1.5 g/cm³. All of them had been fully saturated during the previous water permeability testing. The gas testing in the triaxial cells was carried out by injecting helium gas to the specimens in three stages under increased quasi-hydrostatic stresses of σ_a/σ_r = 2.2/2, 4.2/4, and 6.5/6 MPa. The results are illustrated in figure 2.28 in terms

of measured gas up- and downstream pressures (P_g, P_o), gas permeability (K_g), axial and radial strains (ε_a, ε_r) versus elapsed time. Some interesting phenomena can be identified from the data.

Tab. 2.10 Results of the gas penetration tests on the water-saturated bentonite specimens under volume-constrained conditions

Specimens	Gas breakthrough pressure (MPa)	Gas seal pressure (MPa)	Gas permeability (m^2)	Rest water content (%)	Rest degree of saturation (%)
GMZ01-1	2.4	0.5	6×10^{-18}	47.6	110
GMZ01-2	5.9	0.7	3×10^{-18}	34.8	120
GMZ01-3a	7.9	3.0	5×10^{-19}	-	-
GMZ01-3b	5.9	1.8	-	30.8	123
GMZ01-4	9.6	7.0	9×10^{-21}	28.8	135
GMZ02-1	0.9	0.1	2×10^{-17}	29.1	103
MX80-1	1.65	-	5×10^{-19}	35.5	104
GMZ01-P[1]	0.39	0.07	9×10^{-16}	46.0	59
GMZ01-B[2]	4.3	3.8	2×10^{-19}	23.2	101
GMZ01-BP[3]	1.71	0.45	5×10^{-17}	34.5	89

Stage I

Firstly, the specimens were compacted by increasing axial and radial stresses to σ_a/σ_r = 2.2/2 MPa, which increased the dry densities to 1.41 g/cm^3 at S1, 1.45 g/cm^3 at S2 and 1.6 g/cm^3 at S3 respectively. Under the load, the gas was injected to the three specimens simultaneously at elevated pressure of P_g = 1.5 MPa for 10 days (figure 2.28a). Over the time, no gas outflow was detected. Further gas injection at a flow rate of 0.2 ml/min rose the pressure to a peak P_{gb} = 1.9 MPa, where gas broke through specimen S3. The breakthrough pressure is slightly below the radial stress. The rapid gas release led to a drop of the upstream pressure and a rise of the downstream backpressure. At the lowered upstream pressure P_{gc} and the increased backpressure P_o, the gas flow ceased due to self-sealing of the pathways. Further continuation of the gas injection yielded the second breakthrough at a lower pressure P_{gb} = 1.7 MPa. Following that, a continual pathway was formed indicated by the gradual increase of the backpressure. When the injection

pressure was limited at 1.9 MPa, the gas flow slowed to ceasing over time. A subsequent gas breakthrough/sealing process was induced by dropping the backpressure down.

Tab. 2.11 Results of the gas penetration tests on the water-saturated bentonite specimens under triaxial stress conditions

Stage	Stress (MPa)	Properties	S1: GMZ01	S2: GMZ01	S3: GMZ02
0	$\sigma_a = 0$ $\sigma_r = 0$	Dry density (g/cm^3)	1.3	1.4	1.5
		Water content (%)	38.4	32.0	25.7
		Water saturation (%)	111	113	110
I	$\sigma_a = 2.2$ MPa $\sigma_r = 2.0$ MPa	Dry density (g/cm^3)	1.41	1.45	1.6
		Gas breakthrough pressure (MPa)	> 1.9	> 1.9	1.9
II	$\sigma_a = 4.2$ MPa $\sigma_r = 4.0$ MPa	Dry density (g/cm^3)	1.48	1.51	1.71
		Gas breakthrough pressure (MPa)	3.8	3.8	3.0
III	$\sigma_a = 6.5$ MPa $\sigma_r = 6.0$ MPa	Dry density (g/cm^3)	1.53	1.57	1.76
		Gas breakthrough pressure (MPa)	5.5	5.3	4.8
	After water resaturation	Dry density (g/cm^3)	1.53	1.57	1.76
		Gas breakthrough pressure (MPa)	5.8	5.8	5.7
IV	After testing	Water content (%)	27.1	27.4	12.2
		Water saturation (%)	97	104	63

The gas breakthrough firstly occurred at specimen S3 (GMZ02), which had a relatively low content of montmorillonite ($f_m = 56$ %) compared to S1 & S2 (GMZ01) with $f_m = 74$ %, indicates a significant effect of the swelling mineral on gas penetration in saturated clay. A low content of montmorillonite means a relatively large proportion of free water in the bentonite (figure 2.6), which is relatively easily displaced by the injected gas.

To examine effect of gas flow rate on breakthrough pressure, a low injection rate of 0.02 ml/min was applied after reducing the backpressure to zero. At the low gas flow rate, the upstream pressure firstly dropped down to 1.4 MPa, then fluctuated within 0.2 MPa over several days, and finally decreased gradually. The fluctuation reflected cyclic opening/closing of the pathway. The subsequent increase of the injection rate to 0.05 ml/min resulted in a similar process with fast and parallel increases in both up- and downstream pressures. The breakthrough pressure of 1.5 MPa was slightly higher than before. From

the final period with smooth increase of the pressures, a relatively constant gas permeability is estimated to K_g = 5x10^{-19} m^2.

The gas injection caused deformation of the specimens. The variations of axial and radial strains suggest a combined impact of the gas pressure and the confining stress, which may be expressed by the effective mean stress, σ_{eff} = σ - P_{gp}, where σ = (σ_a + 2σ_r)/3 is the total mean stress and P_{gp} = (P_g + P_o)/2 is the average pore gas pressure. The strain curves show that

- the radial strains were much smaller than the axial ones, which might be partly attributed to the relatively large friction effect along the upper and lower interfaces between the thin specimen and load pistons;
- at σ_{eff} ≈ const, the specimens consolidated with time;
- when the gas pressure increased or the effective stress decreased with time, the specimens expanded gradually; and
- the different specimens showed the same deformation behaviour, independent of whether gas pathways were generated or not; and the gas breakthrough event had not significant impact on the deformation.

Stage II

The stresses were increased to σ_a/σ_r = 4.2/4 MPa, which consolidated the specimens to dry densities of 1.48 g/cm^3 at S1, 1.51 g/cm^3 at S2 and 1.71 g/cm^3 at S3 respectively. The gas was injected sequentially to each specimen by keeping the others closed. Figure 2.28b shows that

- the gas breakthrough at specimen S3 occurred at pressure P_{gb} = 3 MPa which is lower than the radial stress, and then followed by unsteady gas flow with fluctuations of the gas pressure over time;
- both GMZ01 specimens S1 and S2 showed a same gas breakthrough pressure of P_{gb} = 3.8 MPa which is slightly lower than the radial stress, and then followed by unsteady gas flow but with insignificant fluctuations of the gas pressure;
- the unsteady state gas flow through each specimen is also revealed by variations in gas permeability in a range between 5x10^{-18} m^2 and 5x10^{-20} m^2; and
- the impact of gas penetration on the deformation of all the specimens is insignificant as discussed earlier.

Stage III

The stresses were increased to σ_a/σ_r = 6.5/6 MPa, compacting the specimens to dry densities of 1.53 g/cm^3 at S1, 1.57 g/cm^3 at S2 and 1.76 g/cm^3 at S3 respectively. The gas was injected sequentially to each specimen by switching off the others. Figure 2.28c shows that the gas breakthrough pressures of the three specimens are quite similar in a range of 4.5 to 5.1 MPa, which are significantly lower than the radial stress. To examine possible effect of pathway desaturation induced by flowing the unwetted gas, the specimens were resaturated by injecting the synthetic groundwater at increased pressures of 0.5 – 2 MPa over a month. After that, the gas injection was repeated at zero backpressure. It was observed that gas breakthrough took place sequentially from a specimen to another and surprisingly at the same upper limited high pressure of 5.8 MPa, which is higher than before. This conforms that the gas flow resulted in desaturation of the pathways. It is to be noted that a sufficiently long time was required for creating micro-fissures for gas passage by the applied gas pressure.

After testing, water contents of the dismantled specimens were measured, based on which their saturation degrees were calculated for the last load stage III. The results are given in table 2.11 and indicated that specimen S2 maintained full saturation, S1 was slightly desaturated, and S3 was highly desaturated. That implies that only a few gas pathways were created in GMZ01 bentonite specimens S1 and S2 with the high montmorillonite content (f_m = 74 %) and the gas flow might be dominated by the pathway dilatancy. Contrary the large desaturation of GMZ02 specimen S3 with the small montmorillonite content (f_m = 56 %) suggests that the gas pressure drove the free water out of the pores (two-phase flow process).
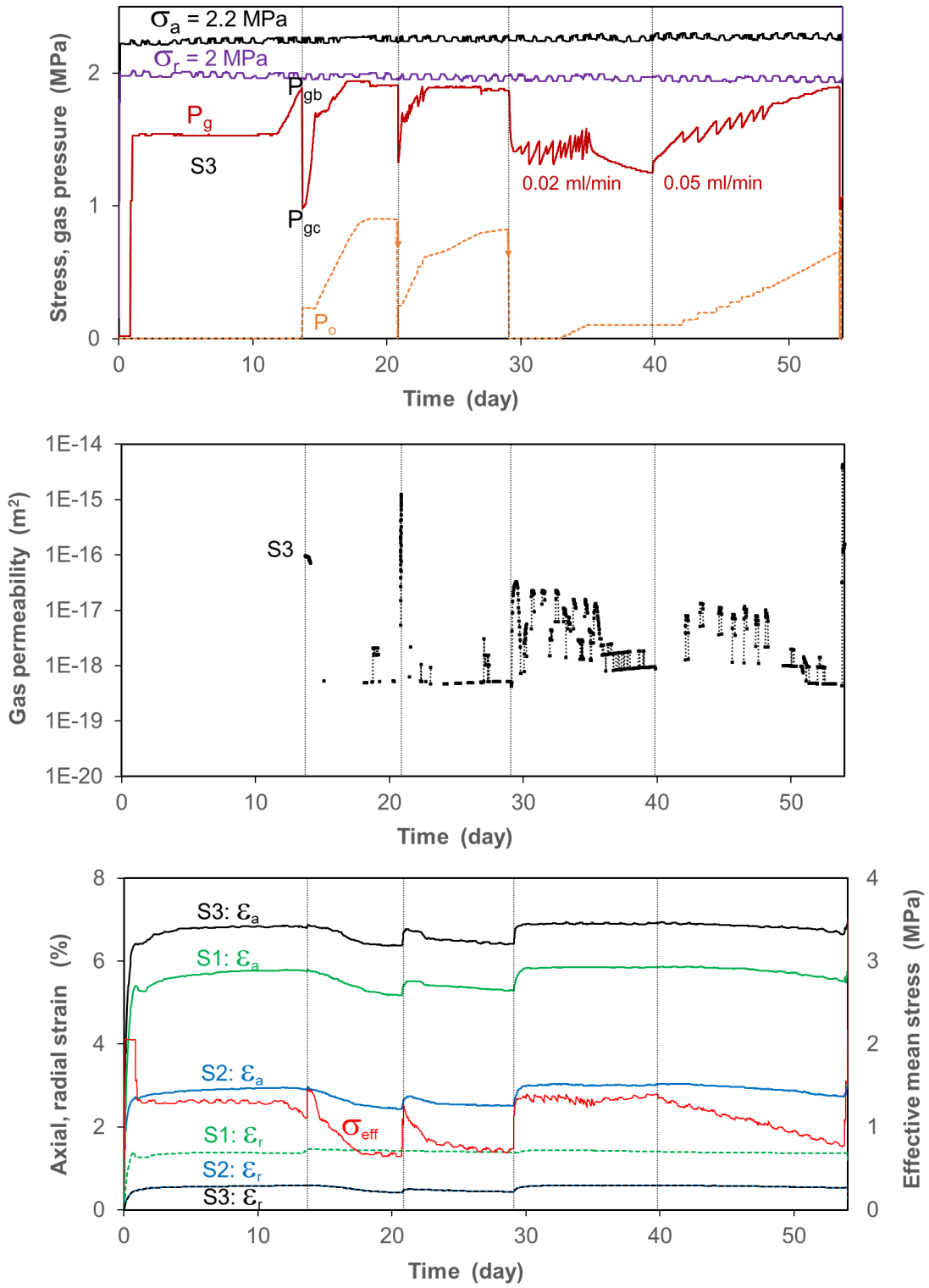
a. test stage I
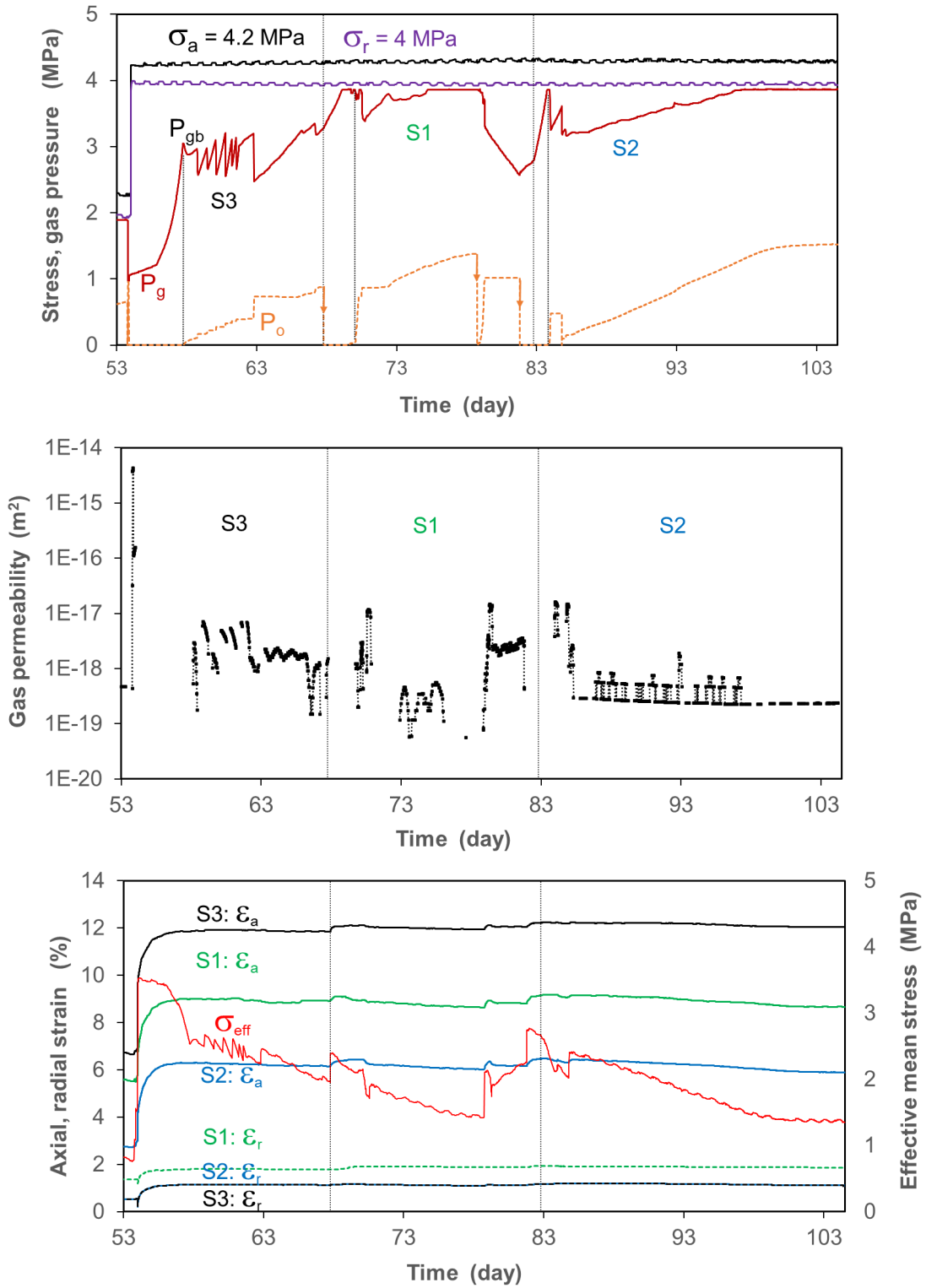
b.   test stage II
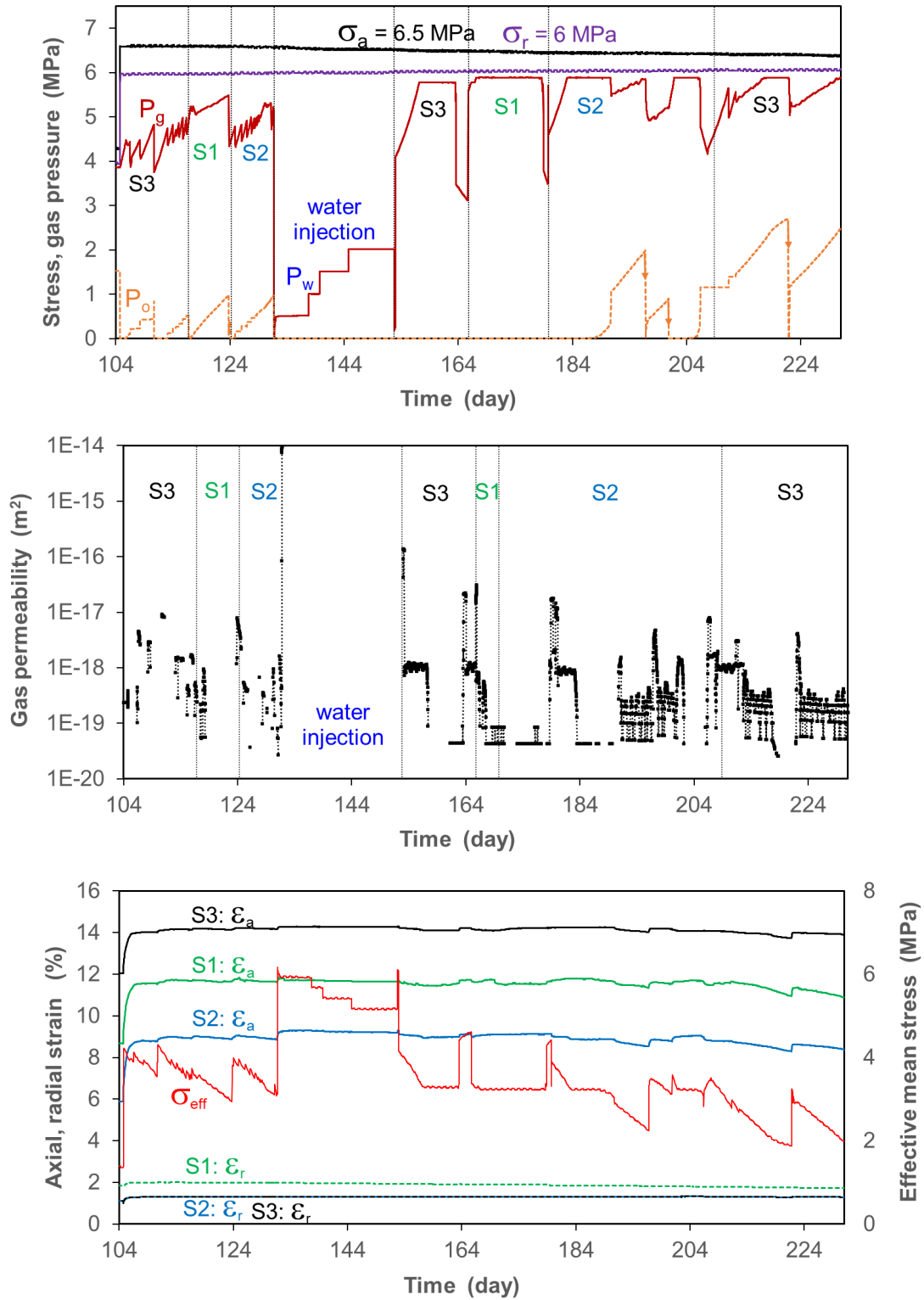
c. test stage III

Fig. 2.28 Gas penetration processes in the water-saturated bentonite specimens
(S1&S2: GMZ01; S3: GMZ02) under triaxial stress conditions

2.6 Deformation and strength

A rock shear, for instance, caused by an earthquake, can yield a shear deformation of the bentonite buffer. The protection of HLW canisters from damage caused by direct hard contact with the rock requires a high plasticity of the bentonite. It is necessary to characterize the deformability and strength of the buffer material for the assessment of the long-term mechanical stability of the canister-buffer-rock system. Within the project, a triaxial test setup was developed and used for investigating time dependent deformation and strength of the bentonite. Preliminary results were obtained on compacted MX80 bentonite.

2.6.1 Test method

The triaxial test setup used for the gas tests mentioned above was also adopted for deformation and strength testing on compacted bentonite. Figure 2.29 illustrates the test setup and layout. It consists of three parallel triaxial cells which are hydro-mechanically coupled with each other. The cells allow a normal sample size of 50 mm diamter and 100 mm length. Identical hydro-mechanical conditions can be applied simultaneously on the samples. The mechanical loading is applied by means of two syring pumps (Model 260D). One is connected to the cell chambers for radial stress (σ_r) and another one to the piston chambers for axial stress (σ_a). The axial and radial stresses applied to each specimen are monitored by pressure transducers. The axial loading can be controlled by adjusting the pump pressure or flow rates. The apparatus allows a maximum radial stress of 15 MPa and a maximum axial stress of 25 MPa. During mechanical loading, axial strain (ε_a) is recorded by a linear variable differential transducer (LVDT) installed at the top of each cell, while radial strain (ε_r) is measured by a circumferential extensometer mounted at the middle length around the specimen outside the jacket. The volumetric strain (ε_v) can be calculated from the measured length and diameter of the specimen. Another syringe pump serves for injecting water or gas into the specimens via inlet lines and sintered porous discs at the bottom. The injection pressure is monitored by a pressure transducer for each specimen. The fluid outflow is recorded at the opposite side of each specimen using a scaled burette at atmospheric pressure.

51
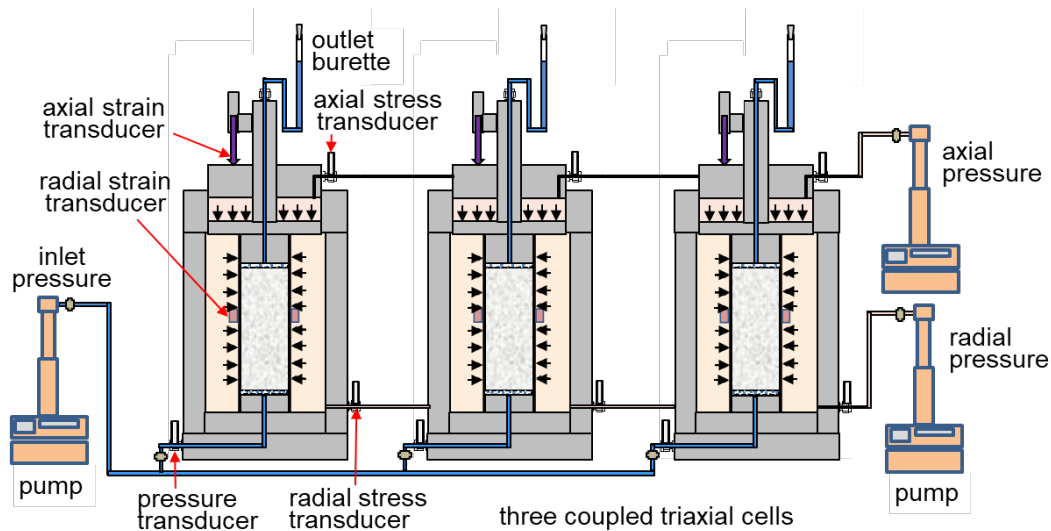
Fig. 2.29   Setup of the gas penetration testing under constant volume

A preliminary test was carried out on three specimens of MX80 bentonite. They were prepared by a) wetting and mixing the material with spraying distilled water to a targeted content; b) storing the mixture in an airtight desiccator for several days to reach a homogeneous water distribution; and c) compacting the wetted material in a cylinder mould to a size of d = 50 mm and l = 100 mm and to a desired density. Figure 2.30 shows pictures of the prepared specimens. Their initial properties are summarized in table 2.12. The specimens are differing from each other in dry density and water content. They are partly saturated to degrees of 60 %, 85 % and 89 %, respectively.

These specimens were installed in rubber jackets, confined in individual cells, and sealed at end sides, i.e., under undrained boundary conditions. Two test phases were carried out: 1) multistage long-term creep under increased deviatoric stresses by keeping radial

stress constant; and 2) multistage short-term deviatoric loading at increased radial stresses. Application of the multistage loading procedure makes it possible to maximize the information about deformation and strength from a single specimen and to eliminate the effect of specimen variability on the results. Such multistage testing procedures were already successfully applied for triaxial testing on clay soil /FRE 93/ and claystone /ZHA 04/.

| Compaction of specimens in a mould | MX80-1 | MX80-2 | MX80-3 |
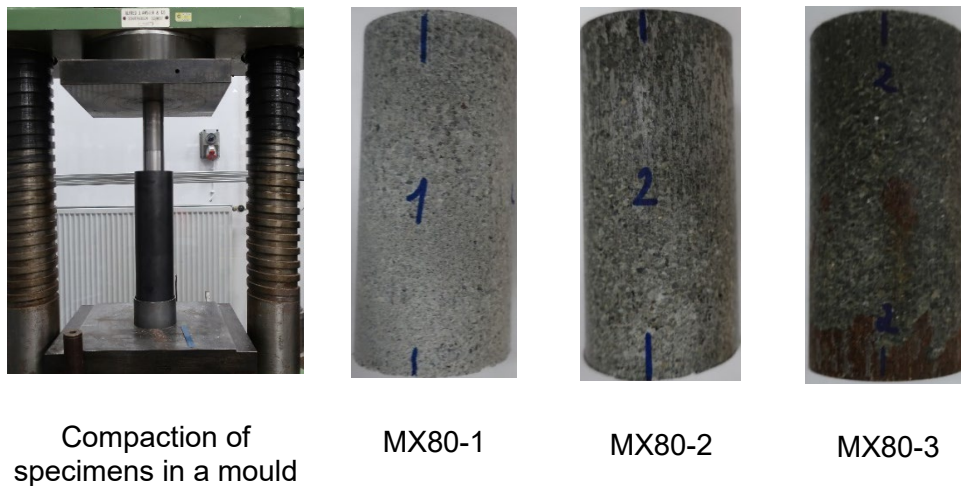
Fig. 2.30   Pictures of the compacted bentonite specimens

Tab. 2.12   Initial properties of the MX80 bentonite specimens for triaxial creep and strength testing

Specimen	dry density (g/cm^3)	bulk density (g/cm^3)	water content (%)	porosity (%)	saturation degree (%)
MX80-1	1.63	1.91	14.5	39.0	60.0
MX80-2	1.67	2.06	19.1	37.6	85.0
MX80-3	1.53	2.03	25.0	43.0	89.0

2.6.2   Test results

Creep

The multistage creep test was conducted simultaneously on the three specimens at ambient temperature and under stepwise increased axial stresses from σ_a = 2.2 to 3, 4, 5, and 6 MPa by keeping a radial stress σ_r = 2 MPa. Figure 2.31 presents results obtained from two specimens MX08-2 and -3 in terms of temperature and stress conditions, variations in deformation and dry density versus elapsed time, except for MX08-1 that failed in the beginning.
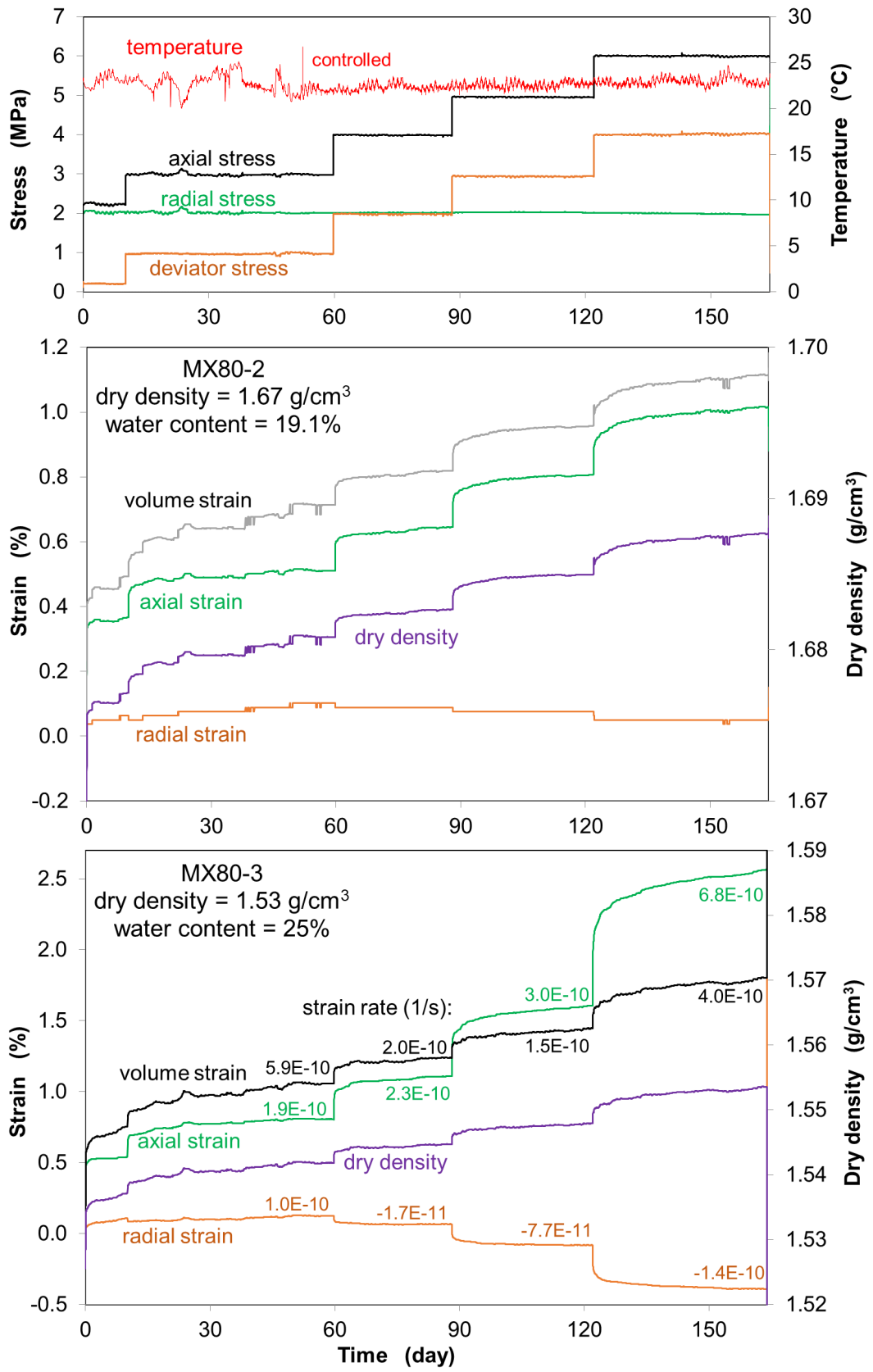
Fig. 2.31   Creep behaviour of compacted MX80 bentonite under triaxial stresses

During the first and second stages at σ_a/σ_r = 2.2/2 and 3/2 MPa, the temperature was uncontrolled and varied in a large range of 20 to 25 °C, which resulted in significant fluctuations of axial/radial stresses and thus strains. Consequently, the quality of the data is poor and not adequate for accurate evaluation. The thermal condition was then improved using an air conditioner to small fluctuations in a small range 21.6 to 23.6 °C, but still not good enough for the precise measurement. The temperature for creep testing should be controlled in a small range of ± 0.1 °C /ZHA 13/.

The strain curves show gradual deformation of the specimens under each constant stress condition. The deformation at the low deviatoric stresses of 0.2 and 1 MPa suggests that no stress threshold exists for onset of creep. Under increased deviatoric stresses of 2, 3 and 4 MPa, the specimens were more compressed in axial direction, accompanied by expansion in radial direction. The axial compression was faster than the radial expansion, leading to a volumetric consolidation and thus an increase in density. This might be resulted from the compaction of the unsaturated pores. Under each constant stress condition, the strain rates decreased with time in the beginning and then tended to constant. Over a month, a quasi-steady state seemed to be reached. At the end of each stage, the "stationary" creep rates were estimated for specimen MX80-3.

The creep deformation of water-saturated clay is mainly governed by slip and rupture of interparticle bound water-films between the particles (cf. figure 2.6). Through thermodynamically analysis of soil flow by application of the absolute reaction rate theory, Mitchell /MIT 76/92/ has derived a creep equation for clay soils

$$\dot{\varepsilon} = A \, \exp\left(-\frac{Q}{RT}\right) \, \sinh(\alpha \, \Delta\sigma) \tag{2.15}$$

where

$\Delta\sigma = {1}/{\sqrt{2}} \sqrt{(\sigma_1 - \sigma_2)^2 + (\sigma_2 - \sigma_3)^2 + (\sigma_3 - \sigma_1)^2}$ is the deviatoric stress (MPa), or

$\Delta\sigma = \sigma_a - \sigma_r$ for triaxial stress state ($\sigma_a = \sigma_1, \sigma_r = \sigma_2 = \sigma_3$),

$\dot{\varepsilon} = {\sqrt{2}}/{3} \sqrt{(\dot{\varepsilon}_1 - \dot{\varepsilon}_2)^2 + (\dot{\varepsilon}_2 - \dot{\varepsilon}_3)^2 + (\dot{\varepsilon}_3 - \dot{\varepsilon}_1)^2}$ is the shear creep rate (s⁻¹), or

$\dot{\varepsilon} = {2}/{3} |\dot{\varepsilon}_a - \dot{\varepsilon}_r|$ for triaxial deformation ($\dot{\varepsilon}_a = \dot{\varepsilon}_1, \dot{\varepsilon}_r = \dot{\varepsilon}_2 = \dot{\varepsilon}_3$),

T is the absolute temperature (K),

R is the universal gas constant ($8.31433 \cdot 10^{-3}$ kJmol⁻¹K⁻¹),

Q is the apparent activation energy (kJmol⁻¹),

A is a parameter in s⁻¹, and α is another parameter in MPa⁻¹.

If $\alpha \, \Delta\sigma < 1$, then $\sinh(\alpha \, \Delta\sigma) \approx \alpha \, \Delta\sigma$, and the strain rate is directly proportional to $\Delta\sigma$

$$\dot{\varepsilon} = A \, \exp\left(-\frac{Q}{RT}\right) (\alpha \, \Delta\sigma) \tag{2.16}$$

The shear creep rates were estimated for specimen MX80-3 with 89-93 % degrees of water saturation. Figure 2.32 depicts the data, which are fitted by equation (2.15) with parameters $A \, \exp\left(-\frac{Q}{RT}\right) = 1.3 \cdot 10^{-10} \, \text{s}^{-1}$ and α = 0.5 MPa^{-1}, and equation (2.16) with $A \, \exp\left(-\frac{Q}{RT}\right) = 7.8 \cdot 10^{-11} \, \text{s}^{-1}$ and α = 1 MPa^{-1}, respectively. The activation energy Q needs to be determined by creep testing at different temperatures. The hyperbolic model (Eq. 2.15) matches all the data well, whereas the linear model (Eq. 2.16) is adequate for the low stress range of $\Delta\sigma \leq 3$ MPa. According to Rutter /RUT 83/, the linear stress/strain rate relation implicates that the time-dependent deformation of water-saturated clay is controlled by diffusive mass transfer or pressure solution processes in interfaces between particles. One of the required conditions for admitting diffusive transport is the existence of interparticle water-films which must be so strongly adsorbed onto grain surfaces that it is not squeezed out and able to support shear stress. At high stresses, the creep rate increases rather exponentially, indicating the contributions from slips and ruptures of the interparticle bound water-films. It is to be pointed out that the consolidation of unsaturated pores in the specimen also plays certain part in the creep.
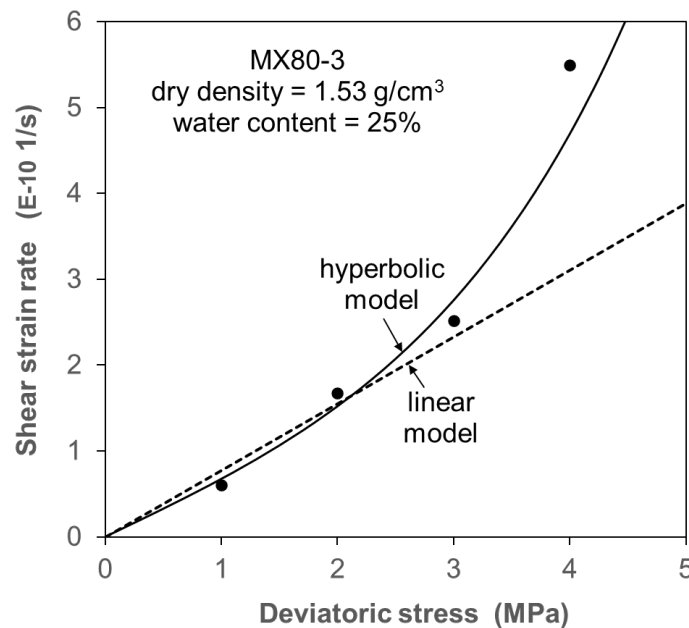
Fig. 2.32   Quasi-steady creep rates of a MX80 bentonite specimen as a function of deviatoric stress

Strength

After the creep tests, both specimens MX80-2 and -3 were loaded at axial strain rate of $1 \cdot 10^{-7}$ and $1 \cdot 10^{-6}$ s^{-1} and at radial stress of 0.5 and 1 MPa, respectively. The stress-strain curves obtained are illustrated in figure 2.33. They show a typical elasto-plastic behaviour with a linear increase of the deviatoric stress with the axial strain in the beginning and then with deviation from the linearity from a yield stress σ_y to a peak strength σ_f. Specimen MX80-2 with a higher density and a lower water saturation exhibited higher strengths (σ_y = 7 MPa; σ_f = 8.5 MPa) compared to that (σ_y = 3.2 MPa; σ_f = 3.5 MPa) of MX80-3. Whereas MX80-2 ruptured at the peak, the deformation of MX80-3 continued. Plastic flow would be expected if the loading were not terminated artificially.
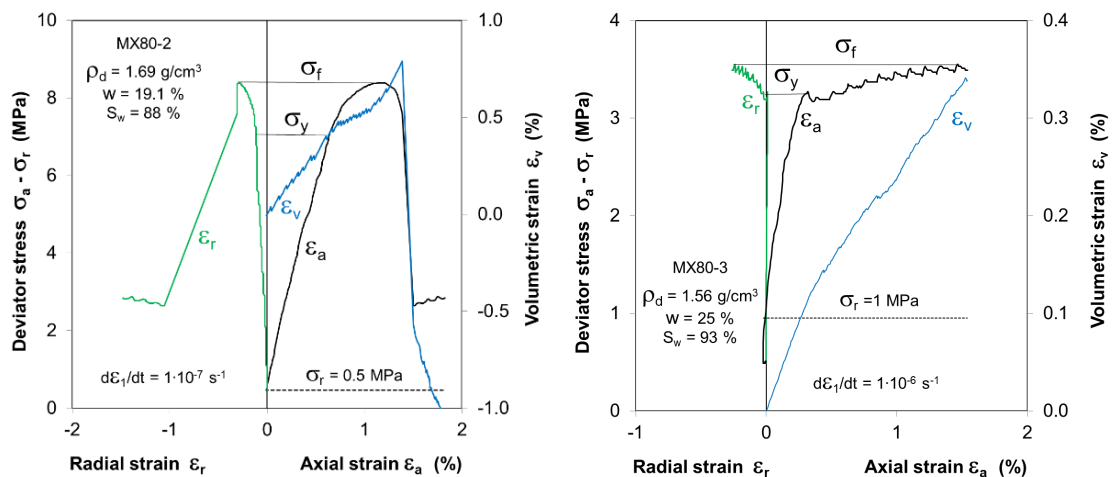
Fig. 2.33   Short-term deviatoric stress-strain behaviour of the bentonite specimens MX80-2 and -3 with different densities and water contents

Following the first test stage at σ_r = 1 MPa, multiple deviatoric loading was conducted on specimen MX80-3 at elevated radial stresses of σ_r = 2, 3, 4 and 5.5 MPa. Before each deviatoric loading, the specimen was quasi-hydrostatically consolidated at increased stresses of σ_a = 6 MPa and σ_r = 5.5 MPa to minimize effect of the previous shear deformation. The deviatoric loading was conducted at an axial strain rate of $1 \cdot 10^{-6}$ s^{-1}. Figure 2.34 presents the stress-strain curves obtained from the pre-consolidation and the deviatoric loading at each constant radial stress. The consolidation lasted over 1 – 3 days for strains to stabilize. Each deviatoric loading was terminated beyond the maximum strength at axial strains of 3 – 4 %, but not to failure.
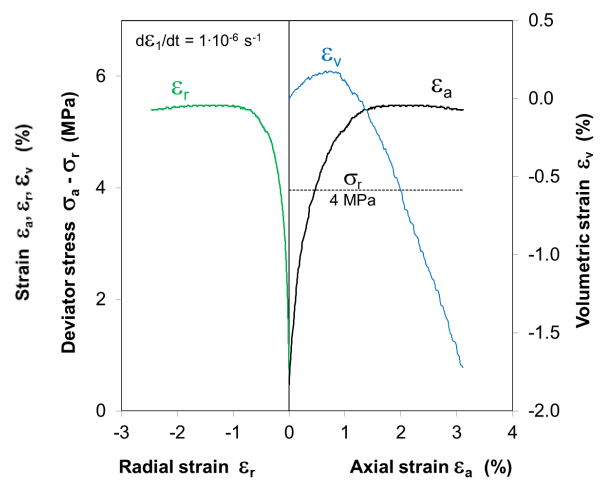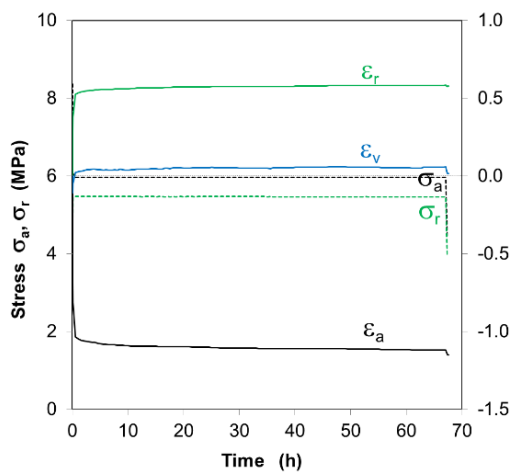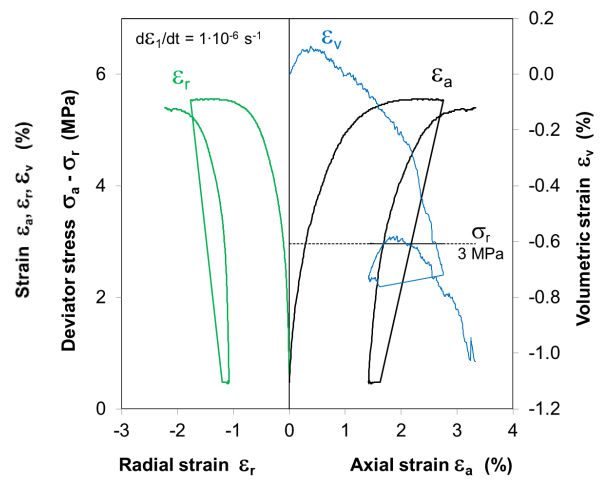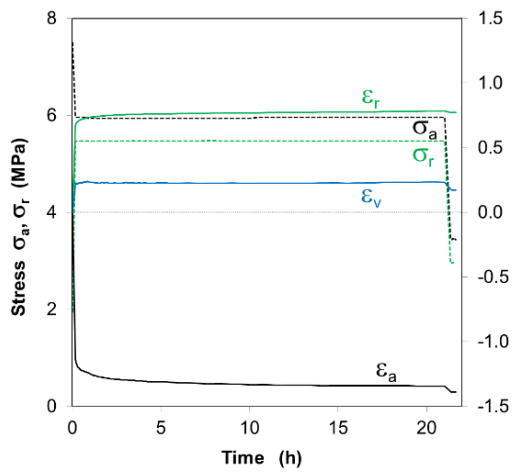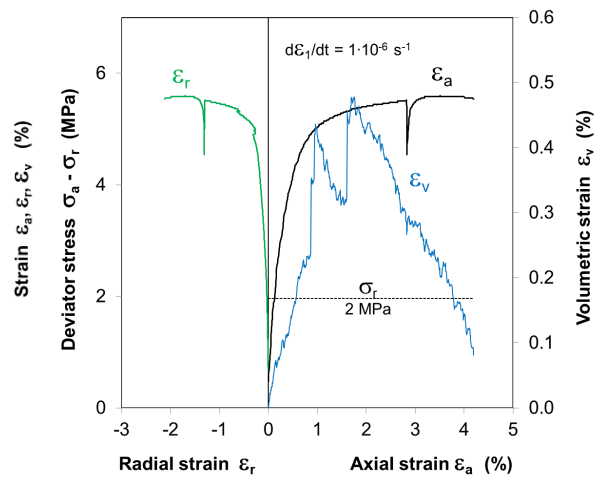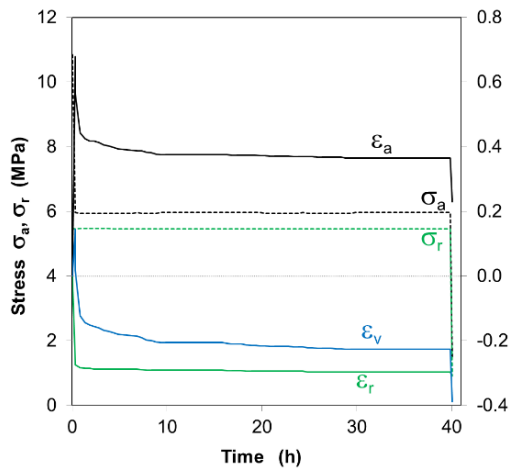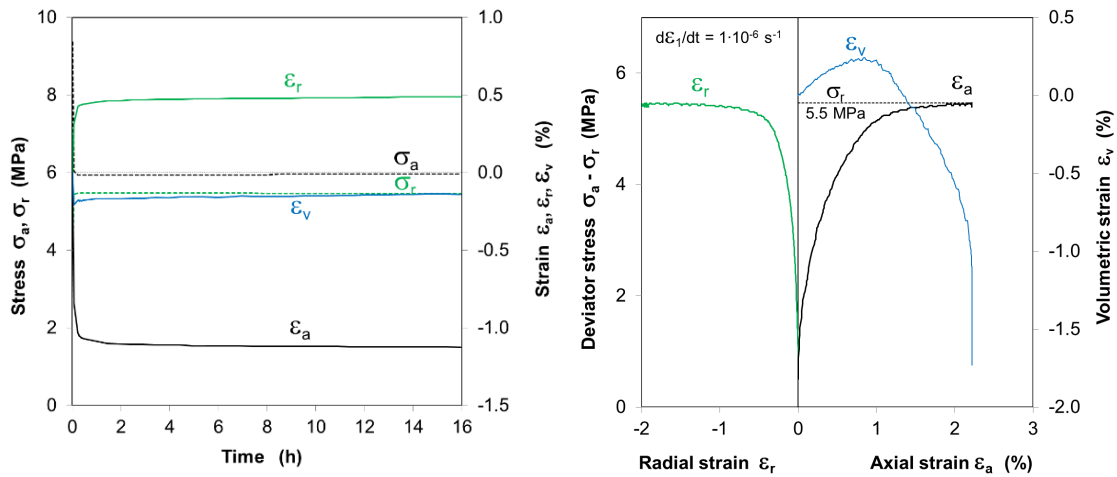
Fig. 2.34 Multistage deviatoric stress-strain behaviour of the bentonite specimen MX80-3

For comparison, the deviatoric stress-strain curves are summarized in figure 2.35 for each applied radial stress. They are very close to each other and reveal the elasto-plastic stress-strain behaviour. Below the yield stress σ_y, the stress and strain are related linearly. Further loading led to a transition from the volume compaction to dilation at deviatoric stress σ_d and then to plastic flow at the maximum stress σ_f. Beyond that, the plastic flow continued without changing the stress and could reach large strains if not artificially terminated. The triaxial tests performed by Dueck et al. (2010) /DUE 10/ and Seiphoori (2015) /SEI 15/ showed large plastic strains over 10 – 17 % in the partly and fully saturated compacted MX80 bentonite (figure 2.36).

The first load at σ_r = 1 MPa generated a shear plane in the specimen MX80-3, which inclined at an angle of α = 40° to the axial stress direction. The subsequent cyclic shear strains at the increased radial stresses should occur along the previously created shear plane because of its weakness, even though it was reconsolidated in some degrees. Figure 2.37 pictures the dismantled specimen with both surfaces of the shear plane. On the surfaces, long shear tracks appeared.

The shear strengths of the specimen MX08-3 are depicted in figure 2.38 as a function of mean total stress. It can be seen that except for the relatively low peak strength σ_f at σ_r = 1 MPa, where the shear plane was firstly generated, the respective yield σ_y, the respective dilatancy σ_d and maximum strength σ_f is nearly constant, independent of the mean stress. That means that the strength of the shear plane was controlled by its

cohesion between the surfaces or bonding of the adsorbed water layer on the surfaces but not the internal friction (friction angle is null).
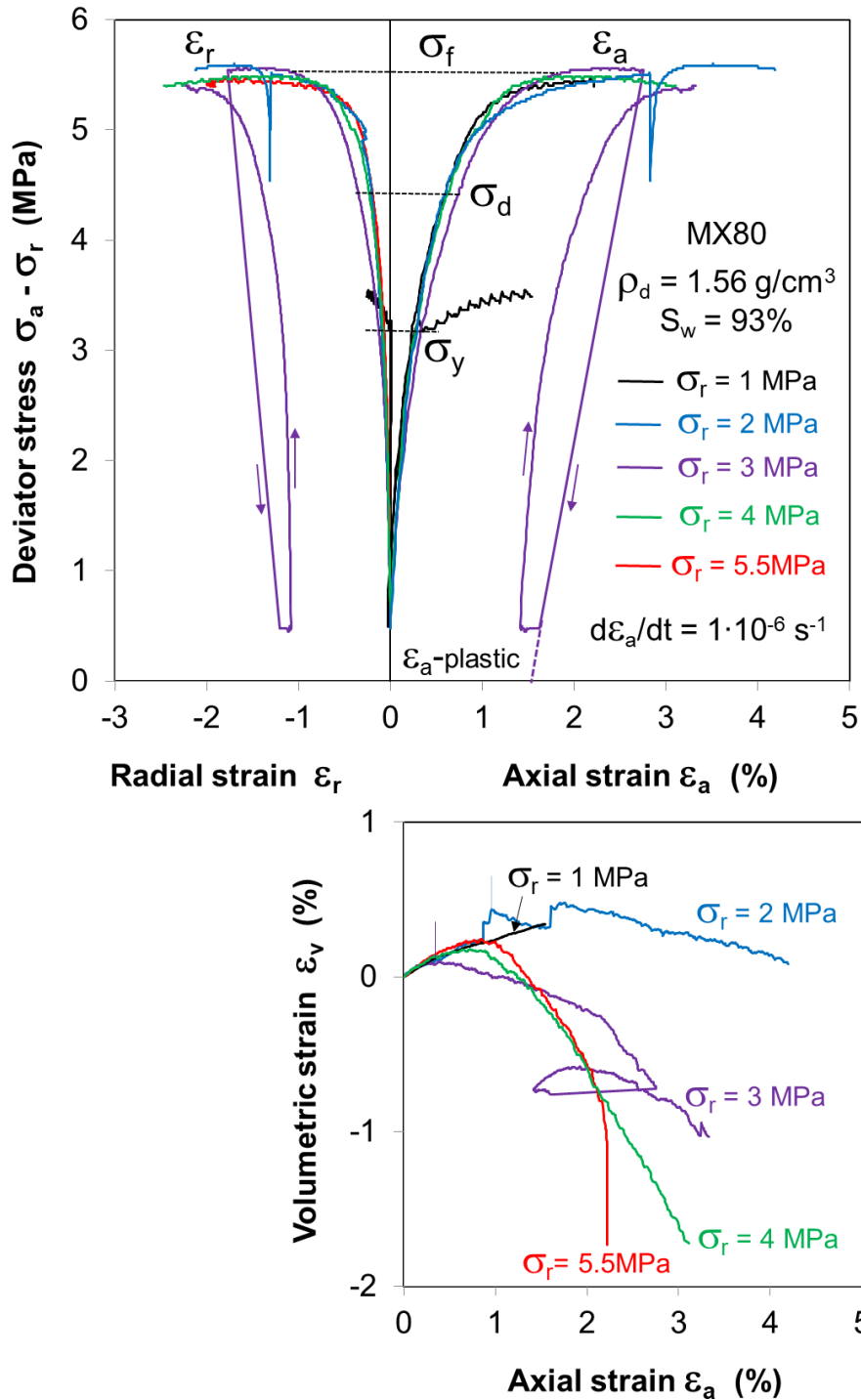
Fig. 2.35 Multistage deviatoric stress-strain behaviour of a bentonite specimen MX80-3
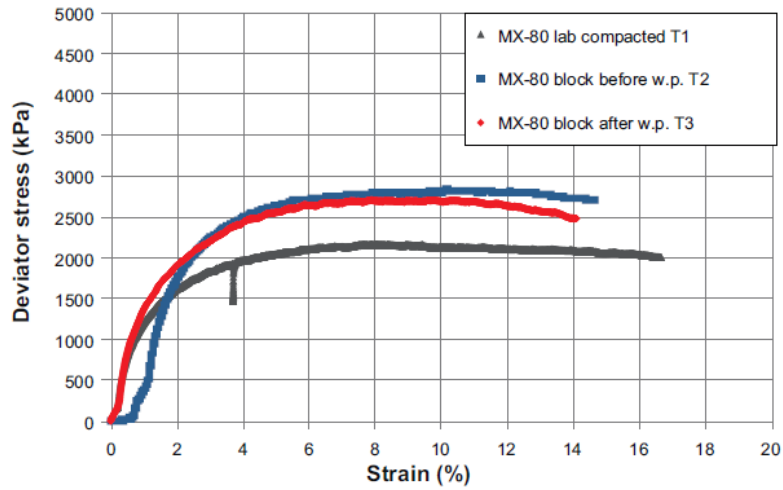
	MX-80 Lab compacted T1	MX-80 Block before w.p. T2	MX-80 Block after w.p. T3
w (%)	27.9/29.8	25.5/29.0	27.2/27.2
ρ (kg/m^3)	1,960/1,980	2,010/1,990	2,020/2,020
e	0.81/0.82	0.73/0.80	0.75/0.75
S_r (%)	96/101	97/101	100/101
At start of shearing			
σ_3 (kPa)	7,400	10,220	8,820
u (kPa)	850	1,170	730
p' (kPa)	6,550	9,050	8,090
Shearing rate (mm/s)	$5 \cdot 10^{-6}$	$5 \cdot 10^{-6}$	$5 \cdot 10^{-6}$

a. Data from Dueck et al. (2010) /DUE 10/
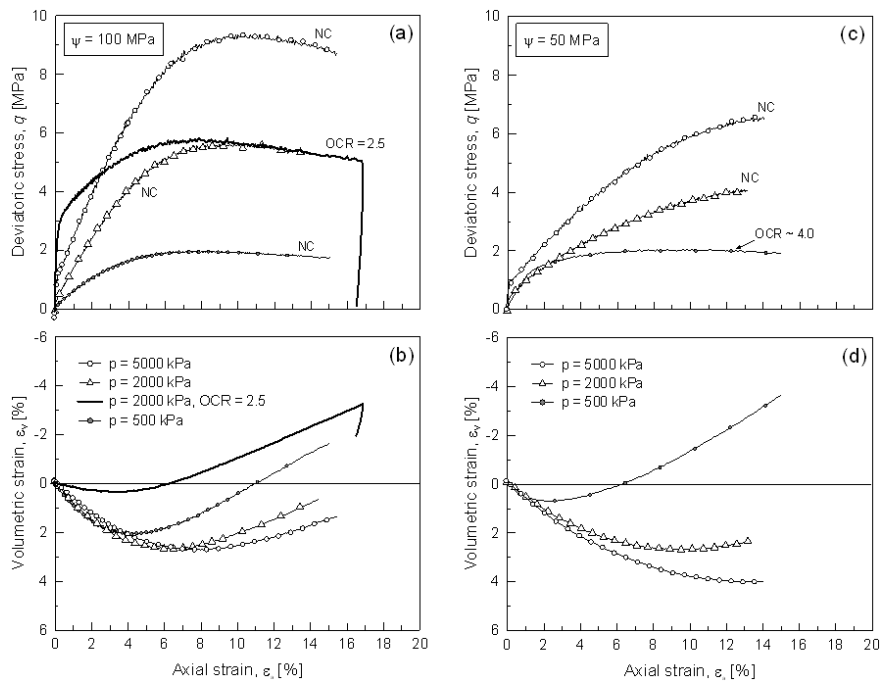
b. Data from Seiphoori (2015) /SEI 15/

Fig. 2.36   Deviatoric stress-strain curves of MX80 bentonite from (a) highly saturated specimens with bulk densities of 1.96 - 2.02 g/cm^3 /DUE 10/ and (b) normally (NC) and over consolidated (OCR) specimens with an initial dry density of 1.5 g/cm^3 at controlled suctions (Ψ) /SEI 15/

61

sheared specimen | shear surfaces
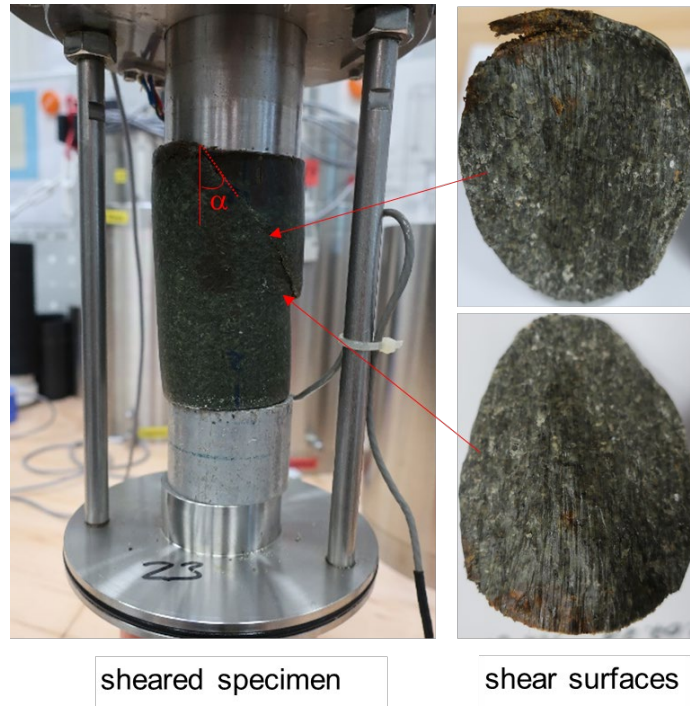
Fig. 2.37 Dismantled specimen MX80-3 with a shear plane inclined at an angle of $\alpha = 40°$ to the axial stress direction
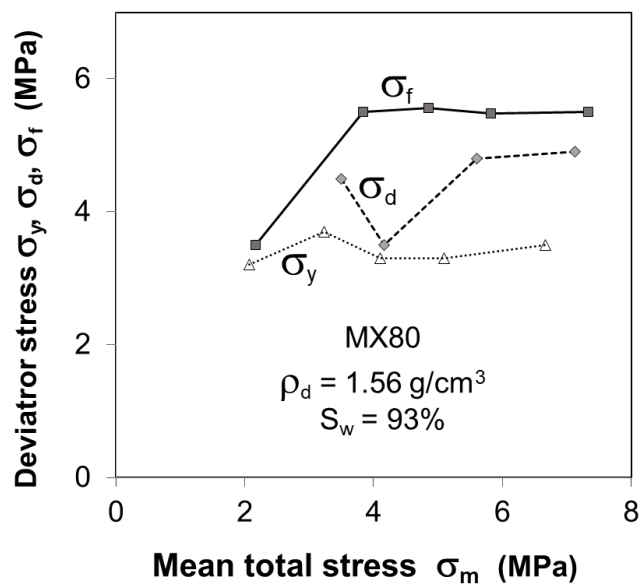
Fig. 2.38 Yield, dilatancy and peak strengths of a MX80 bentonite specimen as a function of mean total stress

In addition, the elastic parameters are also determined from the linear elastic strains before yielding, namely Young's modulus E, Poisson's ratio ν, shear modulus G, and volumetric compaction modulus K, by

$$E = \frac{\Delta\sigma_a}{\Delta\varepsilon_a} \tag{2.17}$$

$$v = -\frac{\Delta\varepsilon_r}{\Delta\varepsilon_a} \tag{2.18}$$

$$G = \frac{E}{2(1+2v)} \tag{2.19}$$

$$K = \frac{E}{3(1-2v)} \tag{2.20}$$

where $\Delta\sigma_a$ is the increment of axial stress, $\Delta\varepsilon_a$ and $\Delta\varepsilon_r$ represent the associated variation of the axial and radial strain, respectively. Figure 2.39 shows that Young's modulus increases with increasing radial stress and conversely Poisson's ratio decreases. Correspondingly, the deduced compaction modulus increases while the shear modulus decreases slightly.
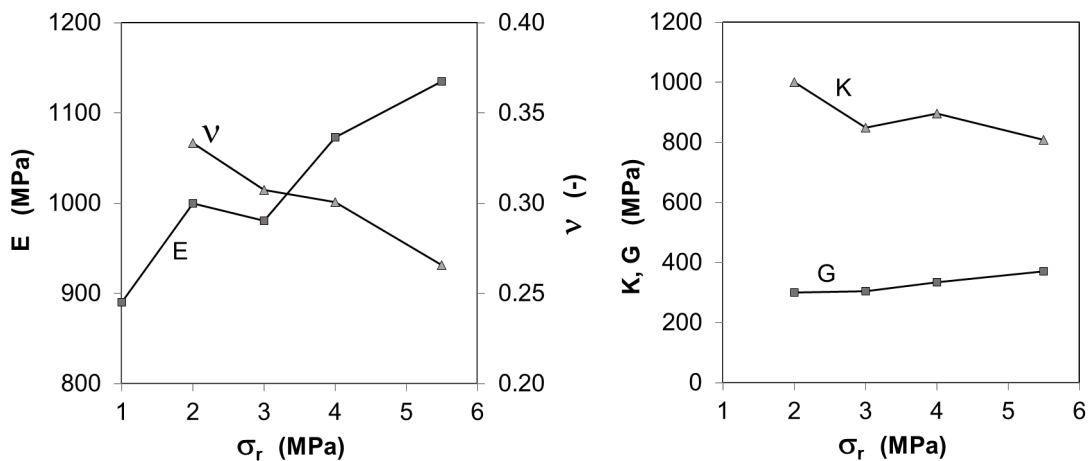
Fig. 2.39　Elastic parameters of a MX80 bentonite specimen as a function of radial stress

Generally, the preliminary results from the compacted bentonite MX80 indicate a high deformability, which is influenced by its inherent properties such as density and water content and external load conditions such as load magnitude and duration. Up to now, available data for the long-term deformation of the bentonite are very limited. It is also true for GMZ bentonite. More investigations on time dependent deformation and strength behaviour of the bentonites are to be continued for deep understanding of the deformation mechanisms and for prediction as well as assessment of the long-term performance of the bentonite buffer under various THM conditions in the DGR.

2.7 Thermal effects

Thermal perturbation (loading) induced by heat-emitting from HLW can affect the chemical-mineralogical and hydro-mechanical properties of the buffer material and hence the ability to retard radionuclide transport /BER 17/VIL 20/. The most concern is whether and how the favourable barrier properties of the bentonite buffer will be altered during the thermal period over several thousands of years under designed temperatures below 100 °C. The previous studies on different kinds of bentonites indicated that:

- the mineral montmorillonite is stable if the maximum temperature is below 100 °C /WER 07/LEU 14/BIR 17/JEN 19/;
- the water retention capacity decreases with increasing temperature /VIL 05/10/ /TAN 05/WAN 15/;
- the swelling capacity (pressure or strain) decreases with increasing temperature /VIL 10/YE 13/; and
- the water conductivity increases with temperature rise due to variations of water viscosity and effective flow channels /VIL 10/YE 13/DAN 07/21/.

Overall, the observed effects of temperature on the bentonite properties can be qualitatively explained by considering the transfer of high-density interlayer water to the macropores that is triggered by the increase in temperature /BIR 17/JEN 19/VIL 20/. Another important issue dealing with thermal impact on gas migration in water-saturated bentonite is however much less investigated. There are only some preliminary data available from Daniels et al. (2017) /DAN 17/21/.

To enhance the understanding of thermal effects on the hydro-mechanical properties of compacted GMZ and MX80 bentonites, a series of thermal experiments was carried out on different specimens by simulating the relevant THM conditions expected in HLW buffer. Four types of testing materials were selected: pre-compacted blocks of GMZ01 and GMZ02 bentonites proposed in the Chinese concept for the DGR in the Beishan granite (figure 1.1); granular MX80 bentonite proposed in the Swiss concept for the DGR in the Opalinus clay /NAG 02/; and crushed clastone/ bentonite mixture suggested by GRS /ZHA 21/. Hydro-mechanical responses of these materials to THM loading were monitored by measuring different parameters such as water uptake and swelling during hydration, deformation, water permeability, gas penetration pressure and conductivity.

2.7.1 Test method

Setup

Two coupled load rigs were used for THM testing on the bentonites. Figure 2.40 illustrates the test layout and setup. Each rig allows two specimens in stainless steel cells of 120 mm diameter and 160 mm height one upon another. They are installed in separated thermal chambers and can be heated up to 110 °C. Each specimen is covered with sintered porous plates and connected to thin holes through the upper load piston and the lower basic plate for fluid flow. A syringe pump (Model 500D) is used for fluid injection at the bottom, while fluid outflow is measured at the top by means of scaled burette at atmospheric pressure. The pump allows a maximum volume of 507 mL, a maximum pressure of 500 bar and flow rates in a range of 1 μL/min to 100 mL/min. Gas testing is usually carried out by injecting helium gas to the specimens at controlled flow rates, during which gas outflow is accumulated in a steel vessel with a volume of 950 ml and the outlet pressure is recorded. Axial load is applied by means of another syringe pump. Axial deformation is monitored using two linear variable differential transducers (LVDTs) mounted between the upper load piston and the cell top. Identical THM conditions can be simultaneously applied to four specimens. This parallel testing provides an opportunity of direct comparison of the behaviour of the different specimens.

Specimens

Two groups of specimens were prepared for testing:

Group 1: Two GMZ01 and two GMZ02 bentonite specimens were pre-compacted in the cells to respective dry densities of 1.71 g/cm^3 and 1.85 g/cm^3, which are close to the buffer blocks designed for the Chinese disposal concept in the granite /LIU 14/CHE 14/.

Group 2: Two granular MX80 bentonite specimens with grains smaller than 5 mm were loosely emplaced in each cell to a dry density of 1.4 g/cm^3, which is consistent with that emplaced in a full-scale drift at Mont-Terri Rock Laboratory /MÜL 17/. Two specimens of a crushed claystone/bentonite mixture (CB7/3) in a mass ratio of 7/3 were loosely emplaced in each cell to a dry density of 1.57 g/cm^3. The crushed claystone was taken from the sandy facies of Opalinus Clay with limited clay content of 20 – 25 % and with grain sizes smaller than 10 mm /ZHA 21/.

Thick-wall cell	Test layout

Test rig 1Test rig 2
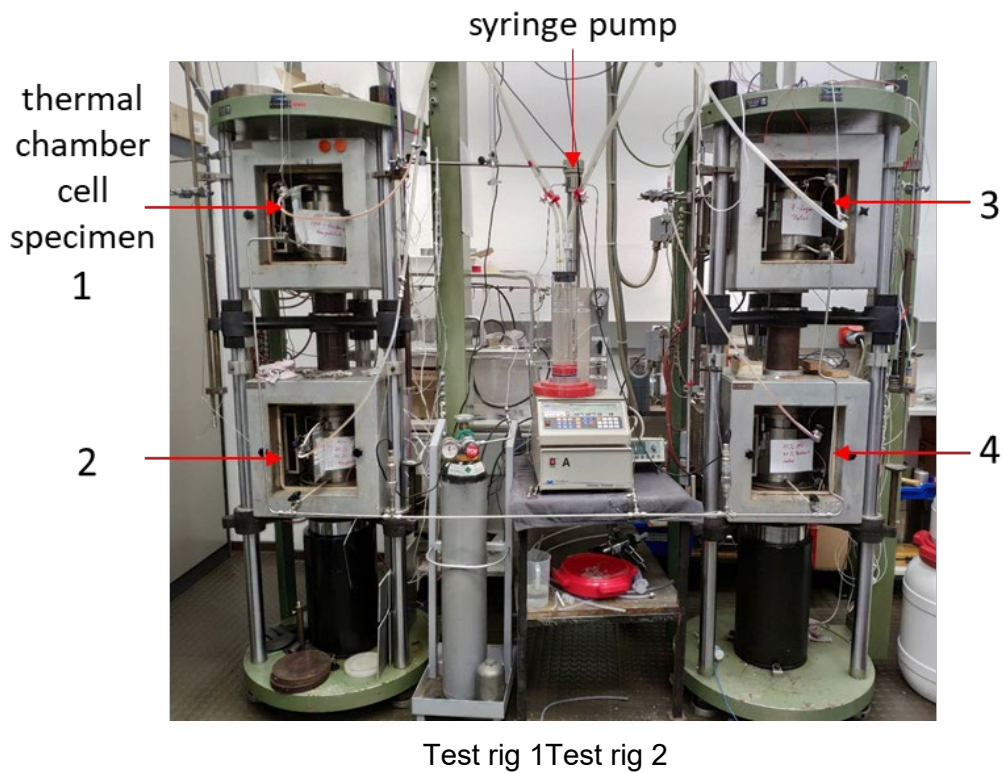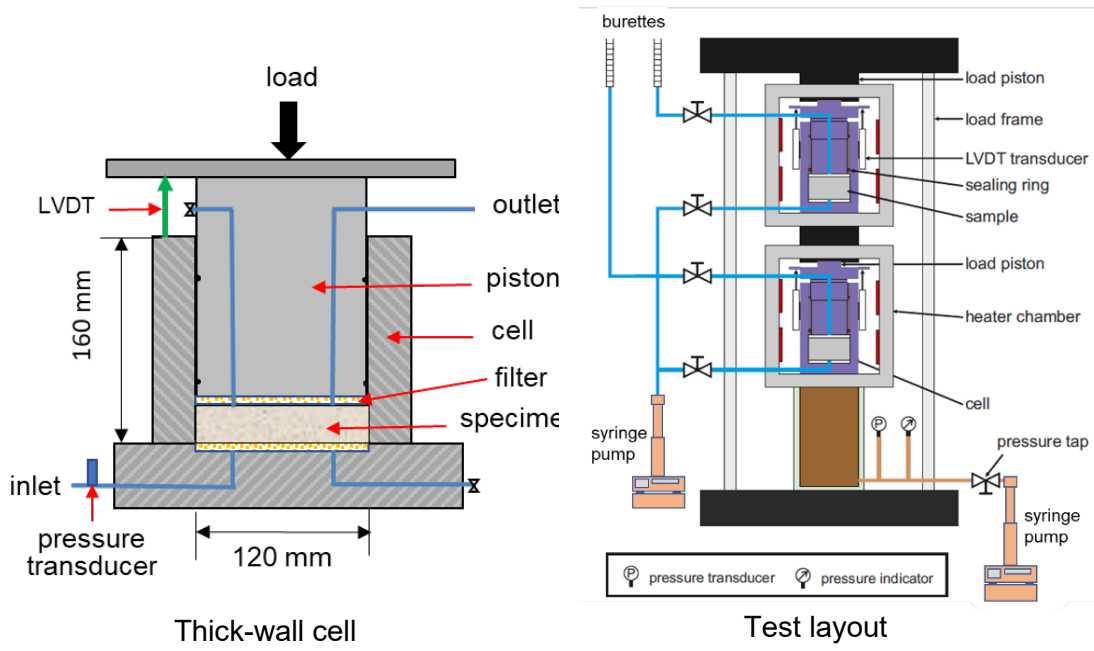
Fig. 2.40   A setup with two coupled load rigs each allowing parallel testing on four specimens in oedometer cells one upon another under identical THM conditions

The initial characteristics of all specimens are summarized in table 2.13. For hydraulic testing, the synthetic Beishan groundwater (BSW) was used for GMZ01 and GMZ02 specimens; and the synthetic Opalinus clay water (OPAW) for MX80 and CBM7/3. The densities and viscosities of the synthetic waters are given in figure 2.9.

Tab. 2.13   Initial characteristics of the bentonite specimens for THM testing in oedometer cells

Specimens	Group 1		Group 2	
Property	GMZ01a-b	GMZ02a-b	MX80a-b	CB7/3a-b
Grain size (mm)	< 0.074	< 0.074	< 5	< 10
Height/Diameter (mm)	25/120	23/120	43/120	65/120
Bulk density (g/cm^3)	1.86	2.0	1.47	1.67
Dry density (g/cm^3)	1.71	1.85	1.40	1.57
Porosity (%)	35.7	30.6	47.8	41.8
Water content (%)	8.1	7.0	5.6	7.0
Saturation degree (%)	39	42	16	26

Procedure

The tests were divided in two groups: group 1 with four specimens GMZ01a-b and GMZ02a-b and group 2 with another four MX80a-b and CB7/3a-b. A common test procedure was performed under various THM conditions to investigate responses of the specimens:

I.   Initial conditions were adjusted to axial stress σ_a = 4 MPa for the compacted specimens GMZ01a-b and GMZ02a-b in group 1 and 0.3 MPa for MX80a-b and CB7/3a-b in group 2. The initial stress magnitudes correspond to the swelling pressures of the specimens after water saturation. Under the loads, two specimens of each material were heated to temperature T = 30 °C and 90 °C respectively.

II. Hydration followed by infiltration of the synthetic water from the scaled burette into the bottom of each specimen at small height differences of 0.5 – 0.8 m. Water uptake and axial strain of the specimens were monitored for evaluation of their hydration processes and swelling capacities.

III. Loading and water injection started upon the water-saturated specimens at the constant temperatures. Axial load was stepwise increased to 3 and 4 MPa for the specimens in group 1, whereas the load for group 2 was firstly lowered to 2 MPa

and then increased to 4 MPa again. Each load step was kept for 1-2 months. Under the load, the synthetic water was injected at pressures of P_w = 0.4 MPa to the specimens in group 1 and 0.8 MPa to the specimens in group 2. The high pressure gradients over 1000 were selected for precise measurement of water flow through the low permeable materials within acceptable durations. In order to examine influence of temperature on porosity and water permeability specimens a of MX80 and CB7/3 in group 1 were stepwise cooled to 70, 50 and 26 °C at axial load of 4 MPa, while specimens b were heated to 50, 70 and 90 °C. each step lasted for weeks to a month. During steady-state water flow, apparent water permeability can be determined (Eq. 2.7).

IV. Gas testing followed to investigate gas penetration behavior of the water-saturated bentonites. Before testing, the water remaining in the inlet and outlet reservoirs was removed by vacuum pumping. Helium gas was then injected to the specimens using syringe pump at controlled flow rates of 0.03 – 0.05 ml/min. Gas outflow was detected by means of the burrete at atmospheric pressure for the specimens in group 1. As first gas bubbles appeared, the gas pressure in the inlet was defined as the breakthrough pressure P_b. In group 2, a steel vessel with a volume of 950 ml was used for accumulation of gas flow out of each specimen. Gas pressures in the up- and downstream were monitored by pressure transducers. The gas injection was continued for 10 – 30 days to examine gas flow process and determine some characteristics such as gas breakthrough and shut-off pressures. The gas flow rate could be estimated from the pressure difference across the specimen with elapsed time (Eq. 2.10).

V. Resealing of the gas-induced pathways was examined on some specimens in group 1 by measuring water permeability at decreased temperature.

VI. Finally, the tested specimens were unloaded and dismantled for visual inspection and examination of final water saturation.

2.7.2   Results

Hydration and swelling

Figure 2.41 illustrates hydration process and changes in porosity observed on the specimens of bentonites GMZ01 and GMZ02. They were firstly heated to 90 °C or 30 °C and then loaded to axial stress of 4 MPa, which resulted in relatively larger compaction at the higher temperature for both bentonites (GMZ01a/02a). This should be attributed to more

evaporation of the pore water at the high temperature, leading to more reduction in bonding or cohesion of the adsorbed water film between clay particles and hence easier collapse of the pore structure. As the synthetic water (BSW) was introduced to the specimens, a hydration process began quickly with rapid water uptake and then slowed down with time until full saturation (calculated). The full saturation of both bentonites was reached earlier at 90 °C but the maximum amount of water uptake was less than at 30 °C. This indicates that the water absorption capacities of the bentonites at high temperatures are relatively lower /MIT 76/HOR 96/. The water uptake yielded gradual expansion of bentonite GMZ01 and the increased porosity of 1.5 % at 90 °C (GMZ01a) is lower than that of 3.5 % at 30 °C (GMZ01b). In contrast, specimens GMZ02a-b showed a different process with a short increase in porosity in the beginning and then a gradual decrease with time to constant. It means that the hydration resulted in a slight consolidation of the specimens rather than expansion because of their swelling capacities with the low montmorillonite content (f_m = 56 %) compared to GMZ01 (f_m = 74 %), even though specimens GMZ02a-b had the higher densities (lower porosities) than GMZ01a-b.

The specimens of bentonite MX80 and the claystone/bentonite mixture CB7/3 were hydrated under a low axial stress of 0.3 MPa and at temperatures of 24 °C and 90 °C (figure 2.42). It is evident that the saturation of the mixture was very fast and required 2-3 days to full saturation, while the bentonite took much langer time over 1 – 2 months to full saturation. Because of its high montmorillonite content (f_m = 86 %), the bentonite could take up more water compared to the mixture with a small montmorillonite content (f_m < 30 %). As mentioned earlier, the amount of water uptake of each material is more at 24 °C than at 90 °C due to the relatively high capacity of water absorption at the low temperature. The hydration caused significant increase in porosity of the bentonite by $\Delta\phi$ = 6.0 % at 24 °C and 2.8 % at 90 °C, respectively. Conversely, the mixture did not swell but shrunk slightly due to its low swelling capacity with the low montmorillonite content.

From the observations, one can conclude that a) the water absorption and swelling capacity of the bentonites decreases with increasing temperature; b) hydration can cause the bentonites to expand or contract depending on montmorillonite content, dry density, and confining stress; and c) the swelling strain of a bentonite increases with increasing montmorillonite content and dry density, but with decreasing confining stress.
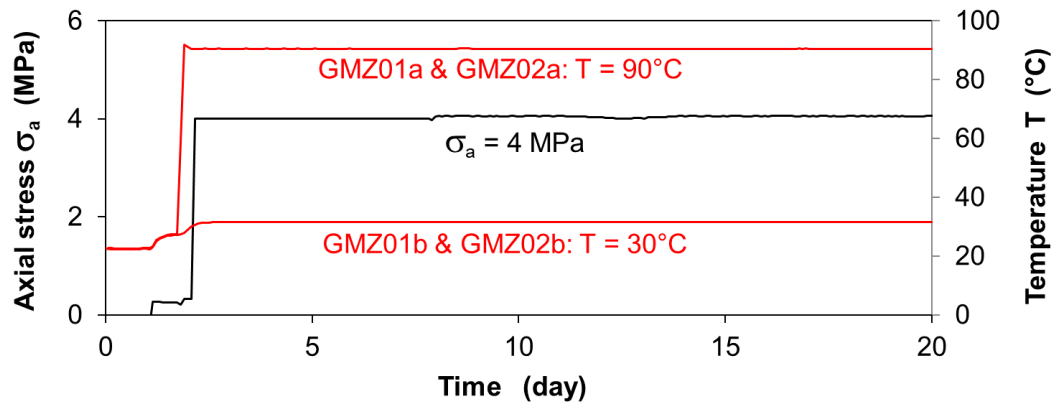
a. applied stress and temperature
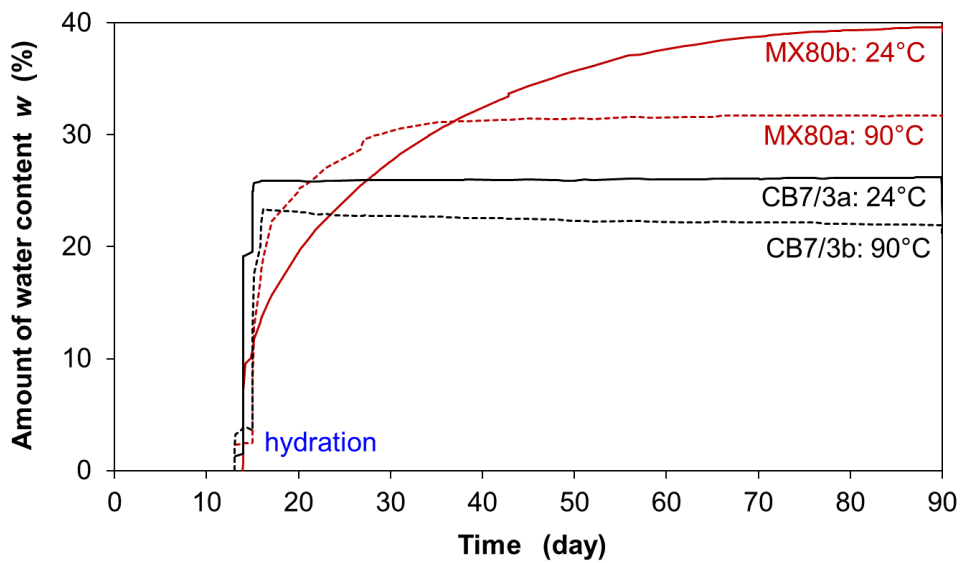
b. water uptake

c. porosity change

Fig. 2.41 Hydration and induced swelling of the bentonites GMZ01 and GMZ02 under axial load of 4 MPa and temperatures of 30 °C and 90 °C
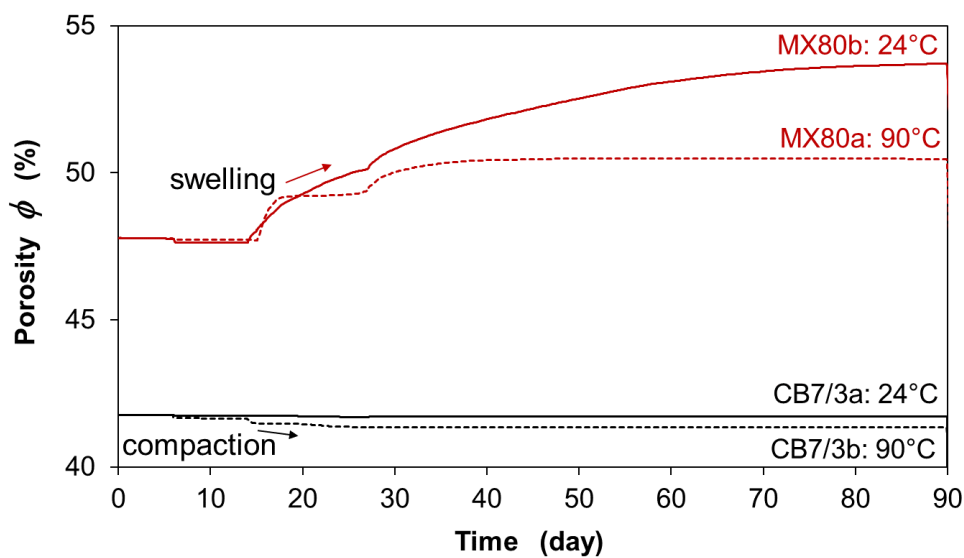
Fig. 2.42 Hydration and induced swelling of the bentonite MX80 and claystone/bentonite mixture CB7/3 under axial load of 0.3 MPa and temperatures of 24 °C and 90 °C

71

Deformation and water permeability

After full saturation, thermal effects on deformation and water permeability of the bentonites were examined. Figure 2.43 shows results obtained on specimens GMZ01a-b and GMZ02a-b. Keeping the previously applied temperatures of 30 °C and 90 °C and axial stress of 4 MPa, the synthetic water was injected into the specimens at increased pressures of P_w = 0.4 and 0.8 MPa. This caused a slight increase in porosity in specimens GMZ01a-b but almost no deformation in GMZ02a-b. When the stress was lowered to 2 MPa, all specimens initially expanded strongly and then slowly over time. Reloading caused each specimen to consolidate to a recovery of almost half the previous porosity. The deformations of GMZ01a-b with the high starting porosities are more significant than those of GMZ02a-b with the lower porosities. The deformations at 30 °C and 90 °C appeared to be nearly the same for each bentonite, i.e., no temperature influence on the deformation. In addition, mechanical unloading/reloading caused a slight increase and decrease in water permeability on each specimen. The corresponding permeabilities at 30 °C and 90 °C are very close for each bentonite. Under the same boundary conditions, the permeabilities of GMZ01a-b are an order of magnitude lower than those of GMZ02a-b, although the porosities of GMZ01a-b are relatively larger. The main reason for the difference is the higher content of montmorillonite in GMZ01a-b, which swells more and seals the porosity better against water flow.

A similar deformation and permeability behaviour was also observed for the bentonite MX80 and the mixture CB7/3 with step loading from 0.3 to 3 and 4 MPa, as shown in Figure 4.44. However, the consolidation of the less dense materials is more significant at the high temperature of 90 °C than at 24 °C. This is because the pore water is less adsorbed on clay mineral surfaces at high temperatures, is less viscous, more mobile and is more easily expelled from the pore space under load. To investigate temperature effects, the samples (MX80a, CB7/3a) were cooled from 90 °C to 70, 50 and 26 °C under the load of 4 MPa, while the others (MX80, CB7/3b) were heated from 24 °C to 50, 70 and 90 °C. Surprisingly, the strain measurements showed rapid compaction of the specimens both when the temperature increased and decreased. Theoretically, an increase in temperature should cause expansion or, conversely, contraction. One reason for the confusion is that the measured strain consists of the specimen itself and the testing system used. Unfortunately, one cannot separate them precisely and see the deformation of the specimen from such a test system.
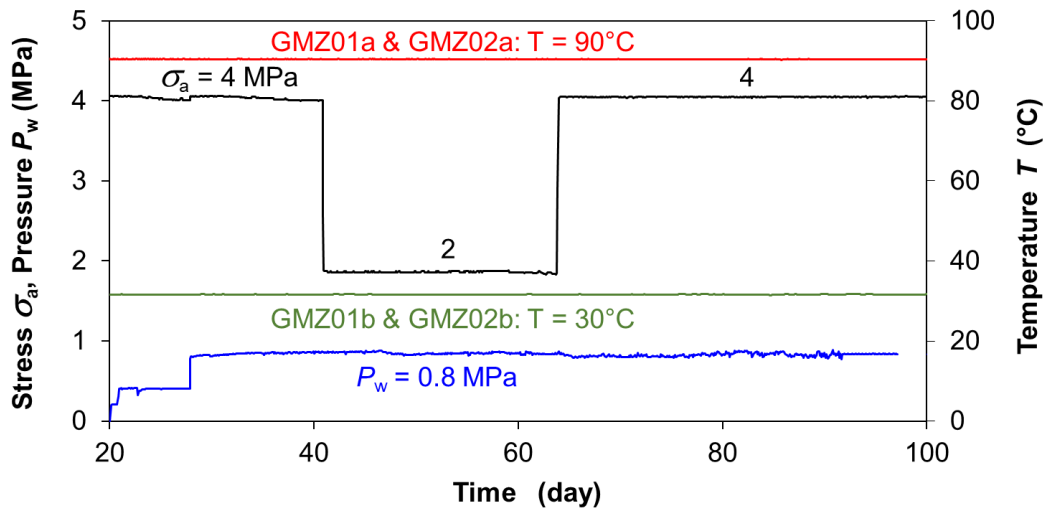
a. applied stress, temperature, and water injection pressure
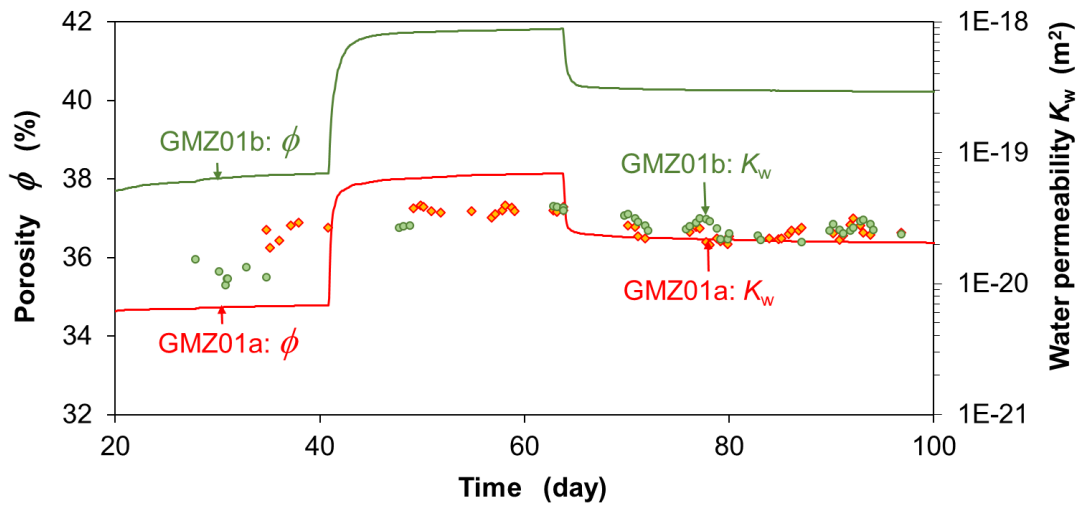
b. porosity and water permeability of bentonite GMZ01
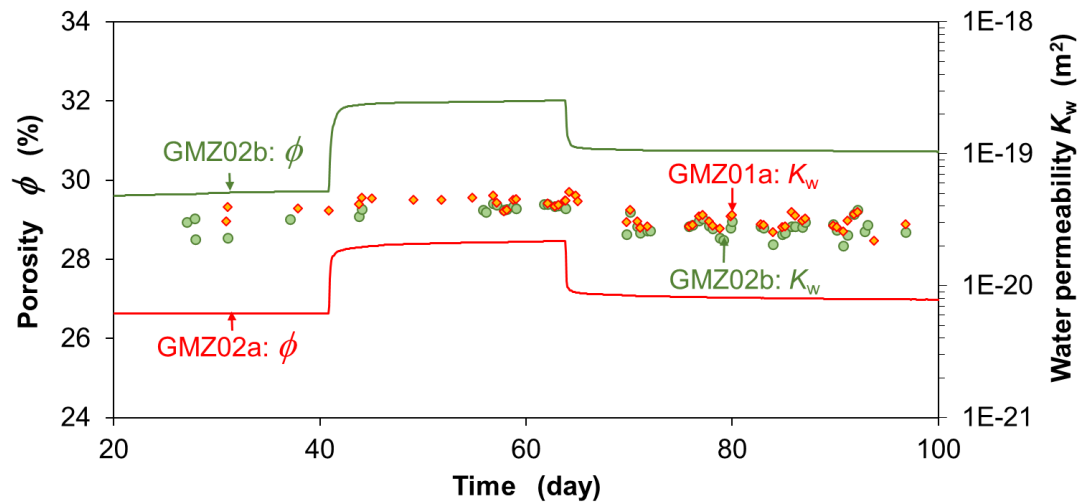
c. porosity and water permeability of bentonite GMZ02

Fig. 2.43 Consolidation and water permeability changes of the bentonites GMZ01 and GMZ02 under varied stresses and constant temperatures
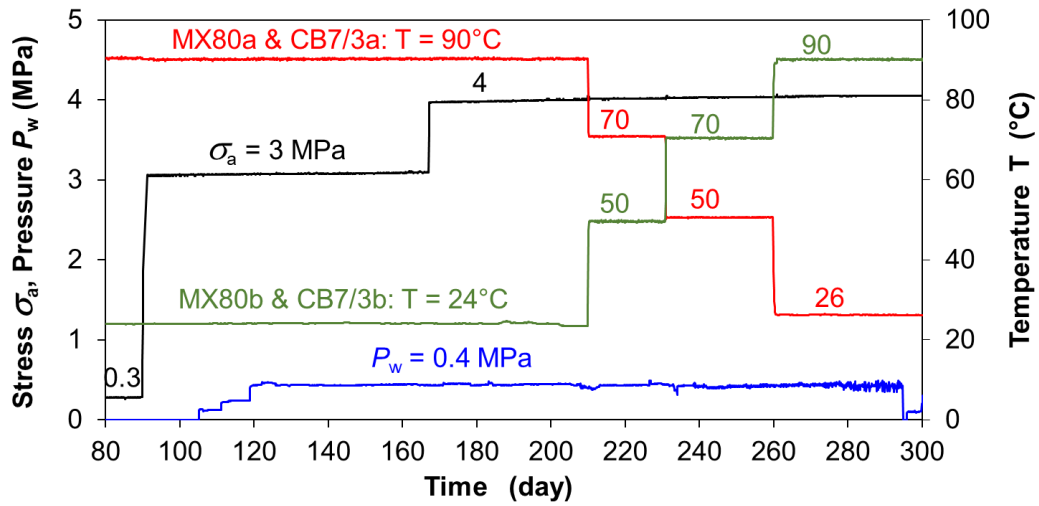
a. applied stress, temperature, and water injection pressure
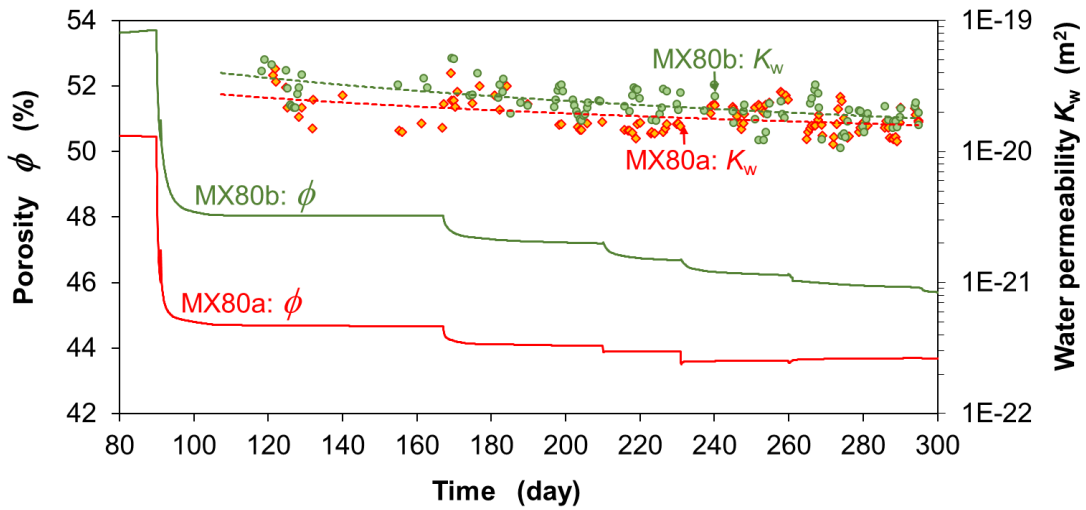
b. porosity and water permeability of bentonite MX80
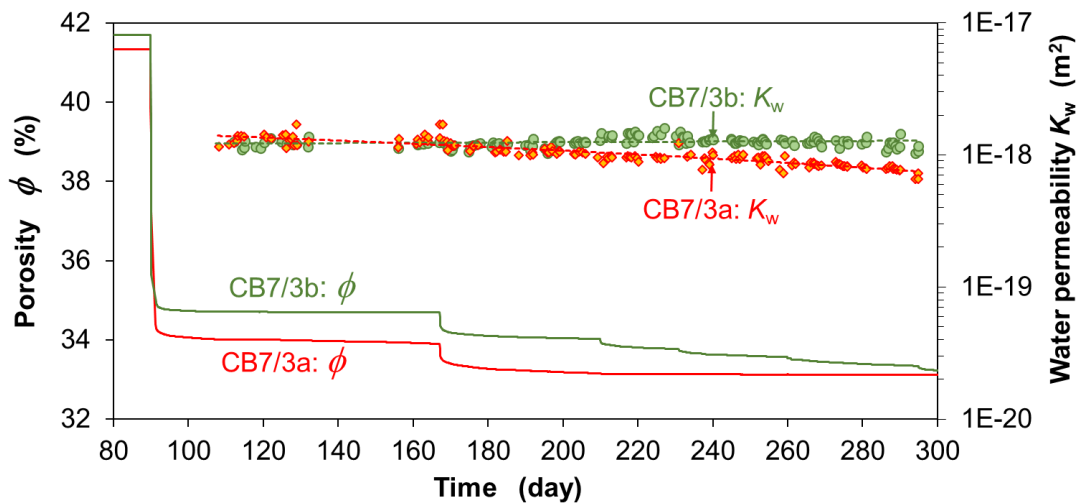
c. porosity and water permeability of claystone/bentonite mixture CB7/3

Fig. 2.44   Consolidation and water permeability changes of the bentonite MX80 and claystone/bentonite mixture CB7/3 under varied stresses and temperatures

74

In addition to the reduction in porosity during mechanical and thermal loading, water permeability also decreased. However, the permeability variations are limited to small ranges, as shown in figure 2.45. The permeability K_w of specimen MX80b decreased from = 2.5×10^{-20} m^2 to 1.8×10^{-20} m^2 with the reduction in porosity from ϕ = 47.2 % to 45.8 % during heating from 24 °C to 90 °C, while K_w of CB7/3a from 1.2×10^{-18} m^2 to 7.8×10^{-19} m^2 with the ϕ–reduction from 33.2 % to 33.1 % during cooling from 90 °C to 26 °C. It is evident that the variation in water permeability is mainly resulted from the porosity change with thermal loading. However, the temperature has an influence on the associated hydraulic conductivity of the clay materials due to thermally induced changes in viscosity and density of the flowing water. A comparison shows that the water permeabilities of the bentonite are about two orders of magnitude lower than that of the mixture, although the total porosities of the bentonite are much larger. In fact, the effective porosities for water flow in the compacted bentonite must be much lower than that of the mixture, because most of the pore water in the bentonite is highly bound and immobile, reducing the effective pore space and connectivity for the flow of free water (cf. figure 2.6).

Gas penetration and impact

Gas penetration testing followed the last water flow stage at constant axial stress of σ_a = 4 MPa and various temperatures of T = 30 − 100 °C. Helium gas was injected at controlled flow rates of Q_g = 0.03 − 0.05 ml/min. Results obtained from the bentonites are illustrated in figure 2.46 in terms of gas injection pressure P_{gi}, backpressure P_{go}, pressure difference $\Delta P_g = P_{gi} − P_{go}$, and axial strain ε_a versus elapsed time. Whereas the gas backpressure P_{go} was recorded during gas injection at specimens GMZ01a-b and GMZ02a-b, it was kept at atmospheric (P_{go} = 0) for MX80a-b. The gas penetration processes performed differed from each specimen due to different conditions but showed a similar pattern with some common features.

Gas breakthrough pressure

Under constant thermal-mechanical conditions, gas injection led to a gradual build-up of the upstream pressure P_{gi} until breakthrough occurred at a peak P_{gb}. The breakthrough yielded a rapid gas release and hence a rapid drop of the upstream pressure to a minimum P_{gc} as well as a rapid rise of the backpressure P_{go}. When P_{go} then maintained constant, the gas flow stopped due to the sealing of the pathways under the swelling

effect of the surrounding matrix. The gas breakdown/sealing event repeated itself with continued gas injection, reflecting a periodic process of the path opening/closing under interactions between gas pressure and confining stress. The periodic burst of gas would progress over time if the paths had not been desaturated by flowing gas.
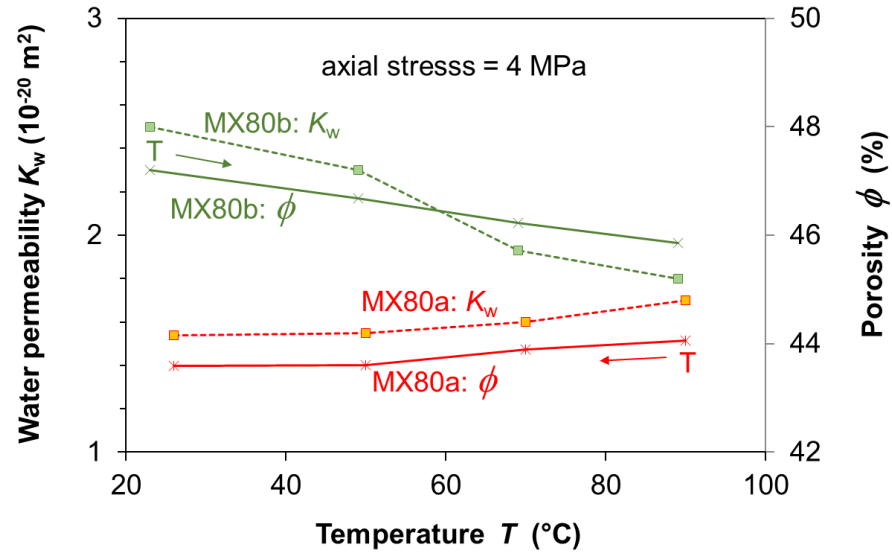
a. bentonite MX80
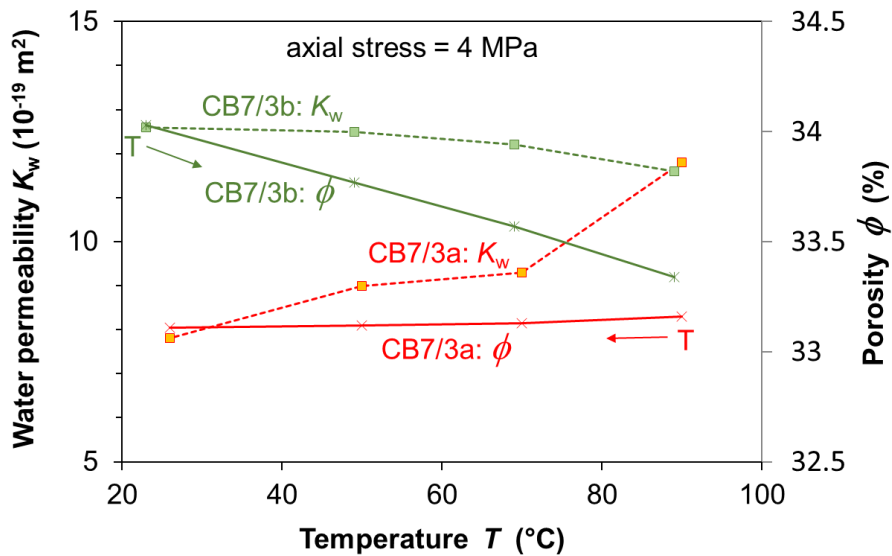
b. claystone/bentonite mixture CB7/3

Fig. 2.45 Thermally induced variations in porosity and water permeability of the bentonite MX80 (a) and claystone/bentonite mixture CB7/3 (b) under axial stress of 4 MPa
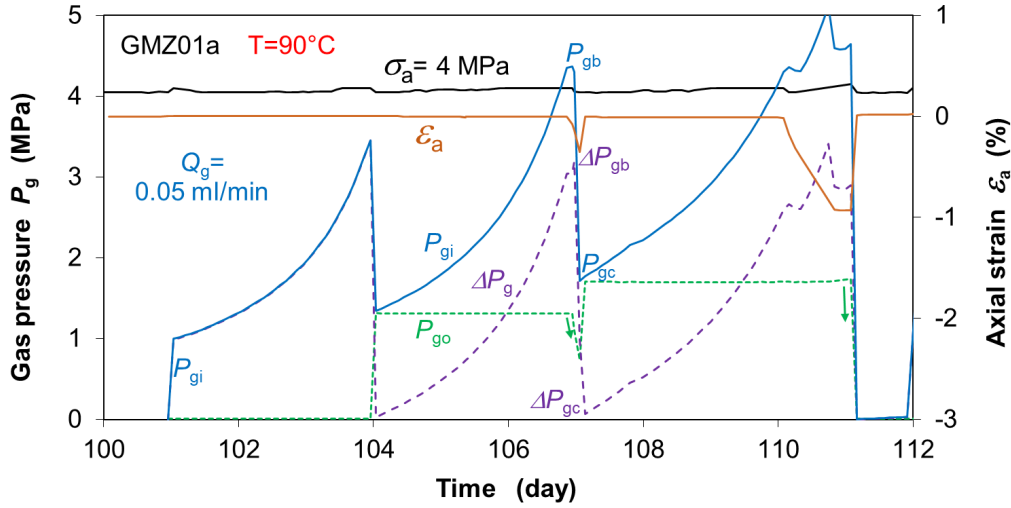
a. specimen GMZ01a with a dry density of 1.71 g/cm^3
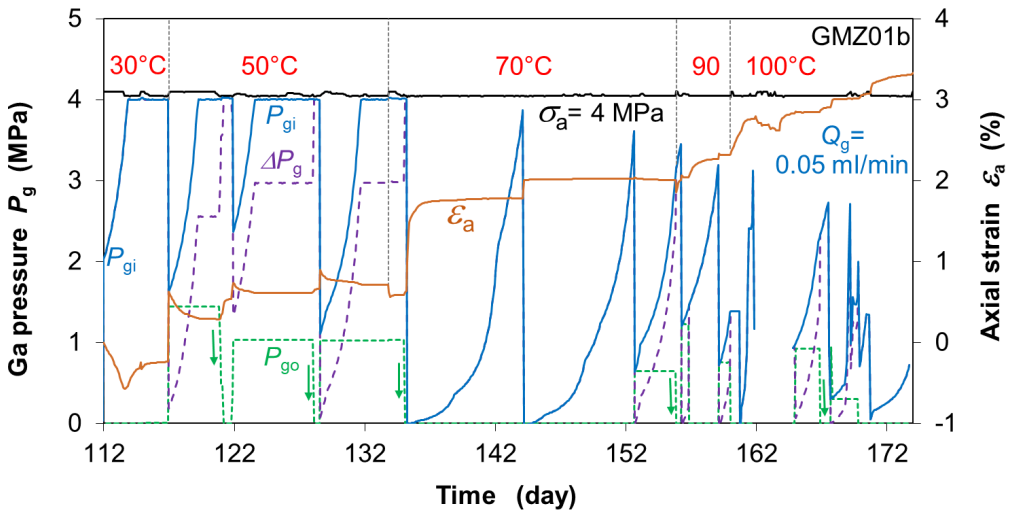
b. specimen GMZ01b with a dry density of 1.61 g/cm^3
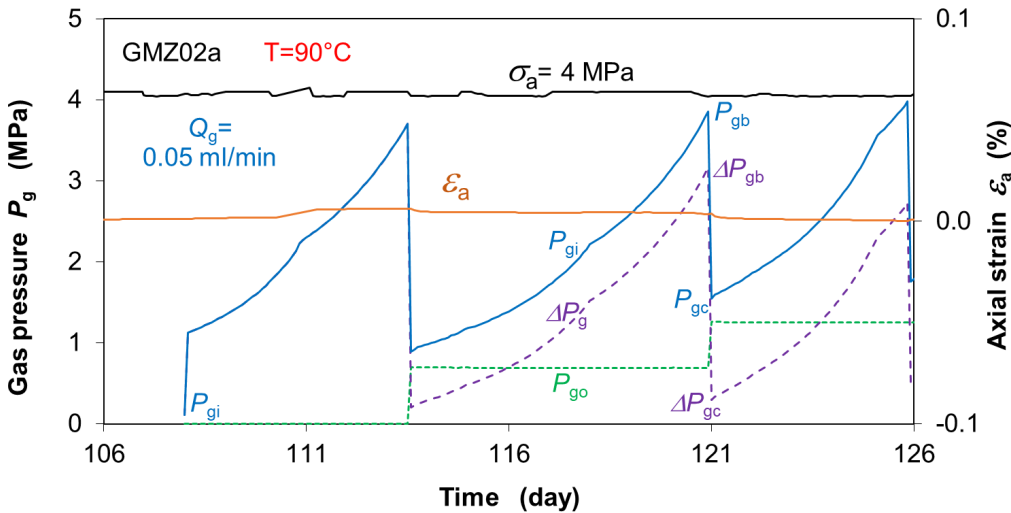
c. specimen GMZ02a with a dry density of 1.95 g/cm^3
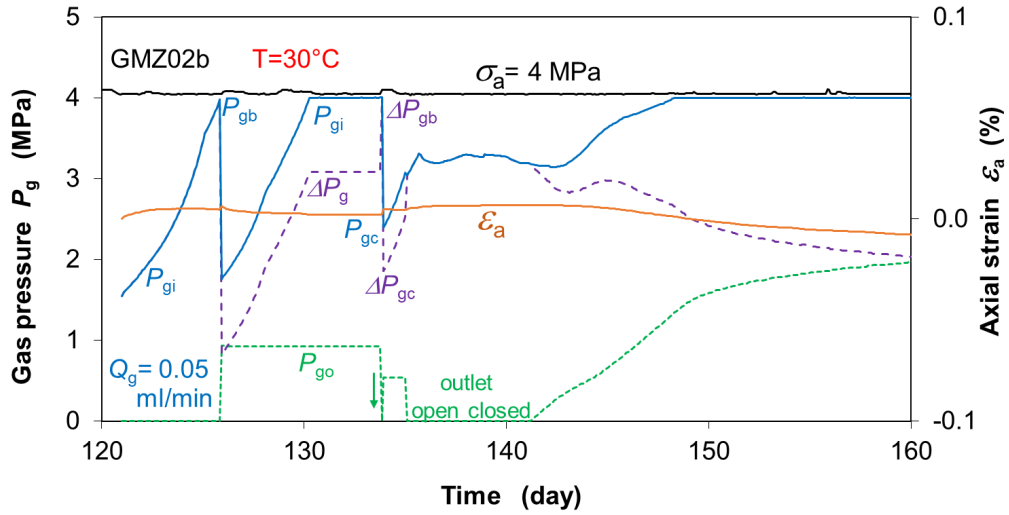
d. specimen GMZ02b with a dry density of 1.85 g/cm³
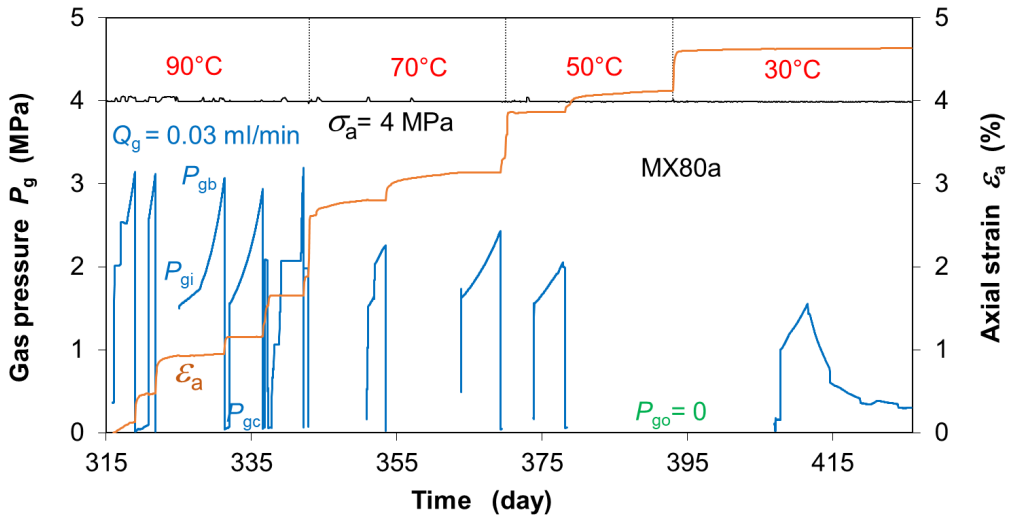
e. specimen MX80a with a dry density of 1.50 g/cm³
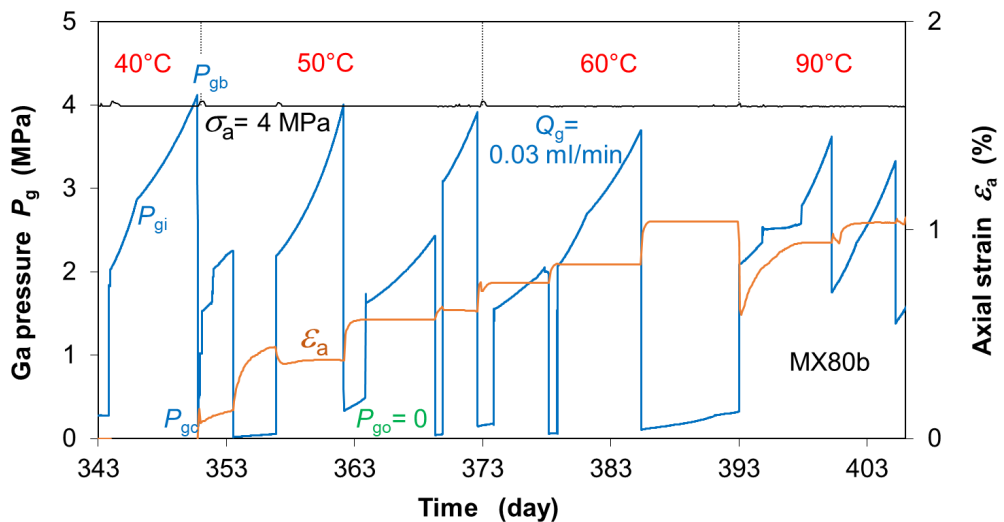
f. specimen MX80b with a dry density of 1.45 g/cm³

Fig. 2.46 Gas injection pressures and strain responses of the bentonite specimens under constant axial stress and different temperatures

78

The determined gas breakthrough and seal pressures P_{gb} and P_{gc} are strongly dependent on the properties of the specimens (mineralogical composition, dry density, water saturation, etc.) and boundary conditions (confining stress, temperature, gas injection rate and duration, backpressure, etc.). For instance, specimens GMZ01a and GMZ02a at 90 °C (figures 2.46a, c) showed the increase of P_{gb} and P_{gc} with the increased backpressure P_{go}. To avoid the gas pressure exceeding the limit stress, the injection pressure has been limited to a maximum of 3.9 MPa, which is slightly lower than the confining stress. However, under the high injection pressure, no gas breakthrough occurred at specimens GMZ01b and GMZ02b under the previously increased backpressures (figure 2.46b, d). Only when the backpressure was reduced to zero, gas broke down. This demonstrates the influence of the backpressure on the gas breakthrough. It appears that the gas backpressure shall be added to the confining stress for the total stress. Equations (2.12a-b) for gas breakthrough may be rewritten by

$$P_{gb} \geq \sigma_{min} + P_{go} + \sigma_T \approx \sigma_{ab} + P_{go} + \sigma_T \tag{2.21a}$$

$$\Delta P_{gb} = P_{gb} - P_{go} \geq \sigma_{min} + \sigma_T \approx \sigma_{ab} + \sigma_T \tag{2.21b}$$

where $\Delta P_{gb} = P_{gb} - P_{go}$ might be taken as the effective gas breakthrough pressure. Similarly, the pressure difference, $\Delta P_{gc} = P_{gc} - P_{go}$, might be taken as the effective gas seal pressure. However, there is confusion about the true effect of gas backpressure and the definition of total stress and effective stress for this case. This uncertainty needs to be clarified theoretically and experimentally.

Thermal effects on the gas penetration in the bentonites were examined on some specimens (GMZ01b, MX80a-b) under elevated or lowered temperatures in a range of 30 °C to 90-100 °C. It was observed that the gas breakthrough pressure decreased not only with increasing temperature at GMZ01b and MX80b (figures 2.46b, f) but also with decreasing temperature at MX80a (figure 2.46e). The heating-induced decrease in gas breakthrough pressure can be attributed to the reduction in viscosity and binding forces in the pore water, while the cooling-induced decrease in gas breakthrough pressure actually resulted from some initial desaturation of the specimen at the high temperatures as measured after testing. The post-testing measurement showed a residual water saturation of 79 % at MX80a cooled from 90 °C to 30 °C over four months. However, MX80b heated from 40 °C to 90 °C exhibited full residual saturation with a calculated degree of 104 %.

Figure 2.47 summarizes the effective gas breakthrough pressures of all specimens as a function of temperature. Along heating path, the gas breakthrough pressure decreases linearly with increasing temperature. This appears to be independent of the mineralogical composition and density of the specimens. At T < 50 °C, the breakthrough pressures are close to or slightly higher than the confining stress. At T > 50 °C, the evaporation of the pore water and thus the desaturation of the pores lowers the pressure threshold for the gas flow. As again shown, the initial desaturation of MX80a caused by the high temperature resulted in lower breakthrough pressures during cooling compared to MX80b, which was less or not desaturated during heating.
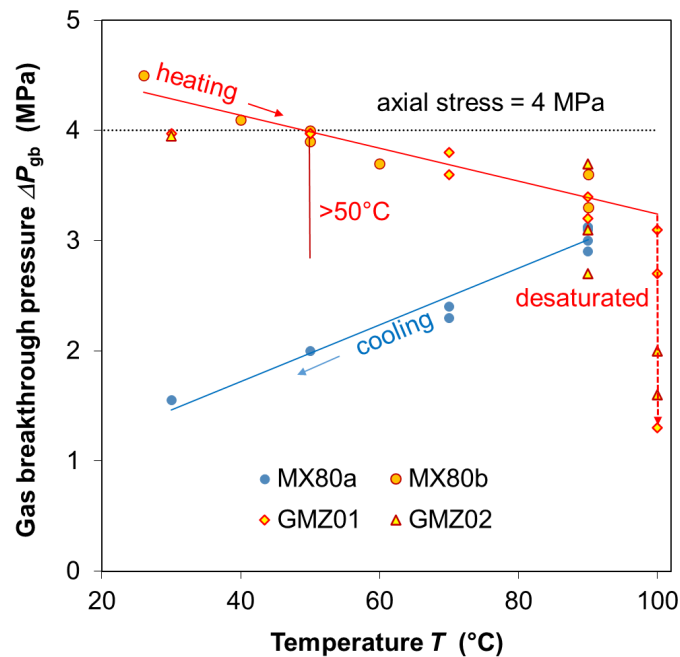
Fig. 2.47   Gas breakthrough pressures of the bentonites as a function of temperature

Strain response

Impact of gas pressure on deformation of the bentonites can be recognized by the strain curves measured on the specimens (figures 2.46a-f). They show that the increase of the gas injection pressure before breakthrough caused only negligible compaction. At each breakthrough, the rapid gas release decreased the pore gas pressure ($P_{gp} = (P_g + P_o)/2$) and thus increased effective stress ($\sigma_{eff} = \sigma - P_{gp}$), which yielded a sudden compaction. The compaction of specimens MX80a-b with the relatively low densities was relatively greater compared to the other specimens with the high densities. It is to be noted that as the gas pressure exceeded the confining stress at GMZ01a (figure 2.46a), the entire sample was moved outwards along the cell wall due to excess gas pressure and inwards upon release of gas pressure at breakthrough. The interface between the specimen and

the cell wall might serve as preferable gas pathways. The interface effect must be avoided in gas testing. As already mentioned, the compaction due to rapid heating (Fig. 2.46f) or cooling (Fig. 2.46e) is due to the thermal deformations of the specimen itself and the test system, which unfortunately cannot be differentiated and analysed here.

Resealing of gas pathways

Gas pathways could severe as preferential pathways for contaminated water and radionuclides to the aquifers and the biosphere. Gas overpressure could also push contaminated water further away through the barriers and act as a supplementary mechanism to enhance the radionuclide transport to the biosphere (Bernier et al., 2017). However, the gas pathways in water-saturated compacted bentonites can reseal under swelling effect. This important issue was examined on two specimens GMZ01a and GMZ02a by measuring their water permeabilities before and after gas penetration. After gas penetrated through GMZ01a and GMZ02a at 90 °C (figures 2.46a, c), the temperature was increased to 100 °C and gas flow continued for a month to widen the pathways. Subsequently, the water permeability was measured by injecting the synthetic water at a pressure P_w = 1 MPa and by lowering the temperature from 100 °C to 80, 55 and 28 °C. The measured data are illustrated in figure 2.48 together with the associated porosities. The water permeabilities almost did not change with the temperature variation. The average values are K_w = 2x10^{-20} at GMZ01a and 3x10^{-20} m^2 at GMZ02a respectively. They are exactly consistent with those before the generation of the gas pathways (cf. figures 2.43b-c). The result shows a full resealing of the pathways in the bentonites.
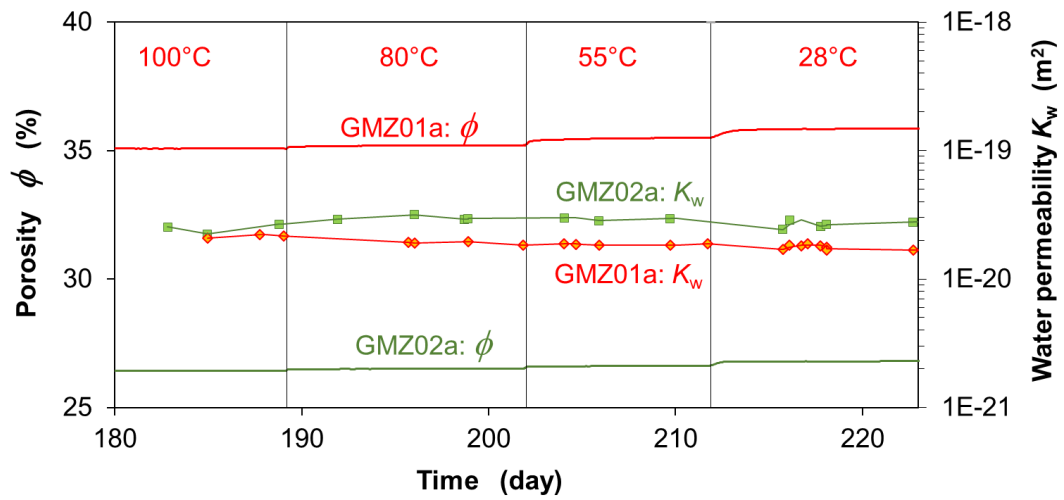
Fig. 2.48   Resealing of the gas pathways in the compacted bentonites GMZ01 and GMZ02 measured by water permeability at different temperatures

3   Summary and conclusions

As the buffer material for the deep geological disposal of high-level radioactive waste in the granite at Beishan site in the north-western China, two types of GMZ bentonite (GMZ01 and GMZ02) have been extensively investigated compared to the well-known MX80 bentonite. These bentonites consist predominately of montmorillonite amounting to 74 % in GMZ01, 56 % in GMZ02 and 86 % in MX80, respectively. Accessory minerals are quartz, cristobalite, plagioclase, K-feldspar, etc. Safety-relevant properties of the bentonites as a buffer around HLW were determined on the compacted specimens with dry densities of $1.3 – 1.8$ g/cm^3 and on the pellets and blocks with engineered voids/gaps, including chemical and mineralogical composition, water absorption and retention capacity, swelling pressure and strain upon hydration, water permeability, gas migration, self-sealing of engineered voids/gaps, deformation and strength, and thermal effects. Specific test setups and methods were developed and applied for the different kinds of laboratory experiments. Synthetic granite groundwater and helium gas were used for respective water and gas flow testing. The experiments provided a large amount of valuable data for deep understanding and accurate evaluation of the buffering performance of the studied bentonites. It was found that the bentonite properties are dominated by montmorillonite content and dry density.

Major insights obtained are

- The water absorption and retention capacities increase with increasing montmorillonite content and decreasing suction. The maximum water content is reached at zero suction but limited by the given porosity under volume-constrained conditions.
- The swelling pressure builds up with hydration and is characterized by a typical double peak pattern due to variations in internal structure. The maximum swelling pressure reached at full saturation increases exponentially with increasing montmorillonite content and dry density.
- Threshold hydraulic gradients were observed for MX80 bentonite at dry densities above 1.5 g/cm^3 but not for GMZ01 and GMZ02. The water permeabilities determined beyond the thresholds decrease exponentially with increasing montmorillonite content and linearly with swelling pressure.
- Gas penetration into the water-saturated bentonites under constrained boundary conditions requires high overpressures that exceed the total stress and tensile strength of the material to create local microcracks for gas passage. Conversely, the

flexible confinement allows the bentonite to deform by gas injection so that pathways can be created at relatively lower gas pressures compared to the confining stress. The network can be disconnected by local sealing with the swelling effect of the bentonite. Under interactions between gas pressure and confining stress, the gas breakthrough/sealing event repeats itself periodically over certain periods of time until the network is opened continuously. The gas permeability after breakthrough decreases exponentially with increasing effective stress.

- The highly water-saturated bentonite MX80 has a high plastic deformability which is time dependent. No stress threshold for shear creep initiation was found. The creep rate increases with increasing deviatoric stress. Shear strength is primarily controlled by shear plane cohesion.

- The engineered voids/voids in the bentonite pellets and blocks can seal themselves due to the high swelling capacity and ductile deformability of the bentonite.

- Various thermal effects on the bentonite properties were observed: a) increasing temperature reduces the water absorption capacity and thus the swelling capacity of the bentonite; b) the hydraulic conductivity of the bentonite increases with increasing temperature due to the decrease in the viscosity and density of the flowing water, and however the intrinsic water permeability is mainly dominated by the effective porosity; c) increasing temperature increases the mobility of adsorbed pore water and thus lowers the pressure threshold for gas penetration; and d) no significant thermal influence on the buffering performance of the bentonites was found.

Generally, the tested bentonites GMZ and MX80 behave qualitatively the same. The quantitative differences in properties stem from the differences in montmorillonite content and dry density. The relationships between the bentonite properties and the montmorillonite content and dry density can be approximated quantitatively using the proposed corresponding equations and the determined parameters.

It should be noted that further research is needed to strengthen the database, improve the understanding of the coupled thermo-hydro-mechanical behaviour of the bentonites, validate the constitutive models and numerical codes for accurate prediction and assessment of the repository performance and safety.

Acknowledgements

References

/BER 17/ Bernier, F., Lemy, F., De Cannière, P., Detilleux, V., 2017. Implications of safety requirements for the treatment of THMC processes in geological disposal systems for radioactive waste. J. Rock Mech. Geotech. Eng. 9 (2017) 428-434. http://dx.doi.org/10.1016/j.jrmge.2017.04.001

/BIR 17/ Birgersson, M., Hedström, M., Karnland, O., Sjöland, A., 2017. Bentonite buffer: macroscopic performance from nanoscale properties. Geological Repository Systems for Safe Disposal of Spent Nuclear Fuels and Radioactive Waste. http://dx.doi.org/10.1016/B978-0-08-100642-9.00012-8.

/BRA 02/ Bradbury, M.H. and Baeyens, B., 2002. Porewater chemistry in compacted resaturated MX-80 bentonite: Physico-chemical characterisation and geochemical modelling, PSI Bericht Nr. 02-10, ISSN 1019-0643, https://www.researchgate.net/publication/237620129.

/BUC 89/ Bucher, F. and Müller-Vonmoos, M., 1989. Bentonite as a containment barrier for the disposal of highly radioactive wastes. Applied Clay Science 4 (2), 157–177.

/CHE 14/ Chen, L., Liu, Y.M., Wang, J., Cao, S., Xie, J., Ma, L., Zhao, X., Li, Y., Liu, J., 2014. Investigation of the thermal-hydro-mechanical (THM) behavior of GMZ bentonite in the China-Mock-up test. Engineering Geology 172 (04/2014), pp. 57–68. DOI: 10.1016/j.enggeo.2014.01.008.

/CHE 15/ Chen, Y.G., Zhua, C.M., Ye, W.M., Cui, Y.J., Wang, Q., 2015. Swelling pressure and hydraulic conductivity of compacted GMZ01 bentonite under salinization–desalinization cycle conditions. In: Applied Clay Science 114 (2015) 454–460.

/CUI 21/ Cui, L.Y., Ye, W.M., Wang, Q., Chen, Y.G., Chen, B., Cui, Y.J. 2021. Insights into gas migration in saturated GMZ bentonite under flexible constraint conditions. Construction and Building Materials 287 (2021) 123070.

/CUS 14/ Cuss, R.J., Harrington, J.F., Noy, D.J., Graham, C.C., Sellin, P., 2014. Evidence of localized gas propagation pathways in a field-scale bentonite engineered barrier system; results from three gas injection tests in the large scale gas injection test (Lasgit). Appl. Clay Sci. 102, 81–92. http://dx.doi.org/10.1016/j.clay.2014.10.014.

/DAN 17/ Daniels, K.A., Harrington, J.F., Zihms, S.J., Wiseall, A.C., 2017. Bentonite Permeability at Elevated Temperature. Geosciences 7(3): 1 – 24.

/DAN 21/ Daniels, K.A., Harrington, J.F., Sellin, P., Norris, S., 2021. Closing repository void spaces using bentonite: does heat make a difference? Applied Clay Science 210 (2021) 106124.

/DIX 02/ Dixon, D.A., Chandler, N.A., Baumgartner, P., 2002. The influence of groundwater salinity and interfaces on the performance of potential backfilling materials, 6th International Workshop on Design and Construction of Final Repositories. ONDRAF/NIRAS, Brussels, Belgium.

/DUE 10/ Dueck, A., Börgesson, L., Johannesson, L.-E. (2010): Stress-strain relation of bentonite at undrained shear - Laboratory tests to investigate the influence of material composition and test technique, Clay Technology AB, Technical Report TR-10-32.

/FRE 93/ Fredlund, D.G., Rahardjo, H. (1993): Soil Mechanics for Unsaturated Soils. John Wiley & Sons, INC.

/GRA 16/ Graham C.C., Harrington J.F., Sellin P., 2016. Gas migration in pre-compacted bentonite under elevated pore-water pressure conditions. Applied Clay Science 132, 353–365.

/GUT 21/ Gutiérrez-Rodrigo, V., Martín, P. L., Villar, M. V, 2021. Effect of interfaces on gas breakthrough pressure in compacted bentonite used as engineered barrier for radioactive waste disposal, Process Safety and Environmental Protection 149 (2021) 244–257. https://doi.org/10.1016/j.psep.2020.10.053.

/ELF 20/   ELF-China Pilot Project: Thermo-Hydro-Mechanical-Chemical (THMC) Processes in Bentonite Barrier Systems, in Pilot Phase: Reanalysis of the BRIUG THM Mock-up Test & Preparation of Forthcoming Research Activities, 2020.

/HAR 17/   Harrington J. F., Graham C. C., Cuss R. J. and Norris S., 2017. Gas network development in a precompacted bentonite experiment. evidence of generation and evolution. Applied Clay Science 147, 80–89.

/HOR 96/   Horseman, S.T., Higgo, J.W., Alexander, J., Harrington, J.F., 1996. Water, Gas and Solute Movement through Argillaceous Media. Report CC-96/1.

/HUE 02/   Hueckel, T., Loret, B., Gajo, A., 2002. Expansive clays at two-phase, deformable, reactive continua: Concepts and modeling options. Chemic-mechanical coupling in clays; from nano-scale to engineering application, Di Maio, Hueckel & Loret (eds), 2002 Swets & Zeitlinger, Lisse, ISBN 90 5809 384.

/IMB 06/   Imbert, C. and Villar, M.V., 2006. Hydro-mechanical response of a bentonite pellets/powder mixture upon infiltration. Applied Clay Science 32(3-4), 197–209.

/JEN 19/   Jenni, A., Wersin, P., Thoenen, T., Baeyens, B., Ferrari, A., Gimmi, T., Mäder, U., Marschall, P., Hummel, W. and Leupin, O., 2019. Bentonite backfill performance in a high-level waste repository: a geochemical perspective, Nagra Technical Report 19-03.

/KAR 07/   Karnland, O., Olsson, S., Nilsson, U., Sellin, P., 2007. Experimentally determined swelling pressures and geochemical interactions of compacted Wyoming bentonite with highly alkaline solutions. Physics and Chemistry of the Earth, Parts A/B/C 2007, 32(1–7): 275-86.

/KAR 08/   Karnland, O., Nilsson, U., Weber, H. and Wersin, P., 2008. Sealing ability of Wyoming bentonite pellets foreseen as buffer material – laboratory results. Physics and Chemistry of the Earth, Parts A/B/C, 33, S472-S475.

/KAU 10/   Kaufhold, S., Dohrmann, R., and Klinkenberg, M., 2010. Water-uptake capacity of bentonites, Clays and Clay Minerals, Vol. 58, No. 1, 37–43.

/LEV 20/ Levasseur, S., Collin, F., Daniels, K., Dymitrowska, M., Harrington, J., Jacops, E., Kolditz, O., Marschall, P., Norris, S., Sillen, X., Talandier, J., Truche, L., Wendling, J., 2020. Initial State-of-the-Art on Gas Transport in Clayey Materials. Final version as of 30.11.2020 of deliverable D6.1 of the HORIZON 2020 project EURAD. EC Grant agreement no: 847593.

/LIU 03/ Liu, Y.M. and Wen, Z.J., 2003. Study on clay-based materials for the repository of high-level radioactive waste. J. Mineral Peztro. 23(4), 42-45 (in Chinese).

/LIU 10/ Liu, Y.M., 2010. Influence of heating and water-exposure on the liquid limits of GMZ01 and MX80 bentonites. J. Rock Mech. Geotech. Eng. 2010, 2(2): 188-192.

/LIU 14/ Liu, Y.M., Ma, L., Ke, D., Cao, S., Xie, J., Zhao, X., Chen, L., Zhang, P., 2014. Design and validation of the THMC China-Mock-Up test on buffer material for HLW disposal. J. Rock Mech. Geotech. Eng. 6.2 (04/2014), 119–125. DOI: 10.1016/j.jrmge.2014.01.004.

/LIU 17/ Liu H.H., 2017. Theory and Applications of Transport in Porous MediaFluid Flow in the ubsurface: History, Generalization and Applications of Physical Laws. Springer International Publishing Switzerland 2017. DOI 10.1007/978-3-319-43449-0.

/LEU 14/ Leupin, O.X. (Ed.), Birgersson, M., Karnland, O., Korkeakoski, P., Sellin, P., Mäder, U., Wersin, P., 2014. Montmorillonite stability under near-field conditions. NAGRA TR14-12. Wettingen, 104 pp.

/MIT 76/ Mitchell, J.K., 1976. Fundamentals of Soil Behavior. University of California, Berkeley, USA.

/MIT 92/ Mitchell, J.K. (1992): Characteristics and Mechanisms of Clay Creep and Creep Rupture, in "Clay-water interface and its rheological implications, Clay Mineral society", Vol.4, 212-244

/MÜL 17/ Müller, H.R., Garitte, B., Vogt, T., Köhler, S., Sakaki, T., Weber, H., Spillmann, T., Hertrich, M., Becker, J.K., Giroud, N., Cloet, V., Diomidis, N., 2017. Implementation of the full-scale emplacement (FE) experiment at the Mont Terri rock laboratory, Swiss J Geosci (2017) 110:287-306.

/MUU 87/ Muurinen, A., Penttila-Hiltunen, P., Rantanen, J., Uusheimo, K., 1987. Diffusion of uranium and chloride in compacted Na-bentonite. Report YJT-87-14. Nuclear waste Commission of Finnish Power Companies, Helsinki, Finland.

/NAG 02/ NAGRA, 2002. Project Opalinus Clay, Models, Codes and Data for Safety Assessment – Demonstration of disposal feasibility for spent fuel, vitrified high-level waste and long-lived intermediate-level waste

/PEA 99/ Pearson F.J., 1999. WS-A Experiment: Artificial waters for use in laboratory and field experiments with Opalinus clay, Status June 1998. – Mont Terri Project, Technical Note 99-31, January 1999.

/PLÖ 07/ Plötze, M. and Weber, H.P., 2007. ESDRED - Emplacement tests with granular bentonite Wyoming. Laboratory results from ETH Zürich. Nagra Arbeitsber. NAB 07-24. Nagra, Switzerland.

/PUS 87/ Pusch, R., Hökmark, H., Börgesson, L., 1987. Outline of Models of Water and Gas Flow through Smectite Clay Buffers. SKB Technical Report 87-10, Stockholm, Sweden.

/PUS 90/ Pusch, R., Karnland, O., Hökmark, H., 1990. GMM - A general microstructural model for qualitative and quantitative studies of smectite clays. SKB Technical Report 90-43, Stockholm, Sweden.

/ROD 99/ Rodwell, W.R., Harris, A.W., Horseman, S.T., Lalieux, P., Müller, W., Ortiz, A.L., Pruess, K., 1999. Gas Migration and Two-Phase Flow through Engineered and Geological Barriers for a Deep Repository for Radioactive Waste. A Joint EC/NEA Status Report, European Commission, EUR 19122 EN.

/RUT 83/ Rutter, E.H. (1983): Pressure solution in nature, theory and experiment, Journal of Geological Society. London, Vol. 140, pp. 725-740

/SEI 15/ Seiphoori, A., 2015. Thermo-hydro-mechanical characterisation and modelling of Wyoming granular bentonite. Nagra Technical Report NTB 15-05, Nagra, Switzerland.

/SEL 14/ Sellin, P. (editor), 2014. Experiments and modelling on the behaviour of EBS. FORGE Report D3.38. 426pp.

/SKB 11/ SKB, 2011. Long-term safety for the final repository for spent nuclear fuel at Forsmark. Main report of the SR-Site project – Volume I. TR-11-01. Svensk Kärnbränslehantering AB.

/SUN 18/ Sun, Z., Chen, Y.G., Cui, Y.J., Xu, H.D., Ye, W.M., Wu, D.B., 2018. Effect of synthetic water and cement solutions on the swelling pressure of compacted Gaomiaozi (GMZ) bentonite: the Beishan site case, Gansu, China. Engineering Geology, 244, 66-74.

/TAN 05/ Tang, A.M. and Cui, Y.J., 2005. Controlling suction by the vapour equilibrium technique at different temperatures and its application in determining the water retention properties of MX80 clay. Canadian Geotechnical Journal 42, 287–296.

/UPC 15/ UPC, 2015. User's Guide of CODE_BRIGHT - A 3-D Program for Thermo-Hydro-Mechanical Analysis in Geological Media, Department of Geotechnical Engineering and Geosciences of Technical University of Catalonia (UPC), Barcelona, Spain.

/VIL 05/ Villar M.V., Martin P.L., Lloret A., 2005. Determination of water retention curves of two bentonites at high temperature. Proceedings of an International symposium on Advanced Experimental Unsaturated Soil Mechanics in Trento, Italy. 77–82.

/VIL 10/ Villar, M.V., Gómez-Espina, R., Lloret, A., 2010. Experimental investigation into temperature effect on hydro-mechanical behaviours of bentonite. J. Rock Mech. Geotech. Eng. 2010, 2 (1): 71–78.

/VIL 20/ Villar, M.V., Armand, G., Conil, N., de Lesquen, C., Herold, P., Simo, E., Mayor, J.C., Dizier, A., Li, X., Chen, G., Leupin, O., Niskanen, M., Bailey, M., Thompson, S., Svensson, D., Sellin, P., Hausmannova, L., 2020. Initial State-of-the-Art on THM behaviour of i) Buffer clay materials and of ii) Host clay materials. Deliverable D7.1 HITEC. EURAD Project, Horizon 2020, No. 847593. 214 pp.

/VOK 14/ Vokál A., Polívka P., Dobrev D., 2014. Experimental investigation of migration of hydrogen through compacted bentonite, in FORGE Report D3.38 (edited by Sellin P) - Experiments and modelling on the behaviour of EBS.

/WAN 15/ Wan, M., Ye, W.M., Chen, Y.G., Cui, Y.J., Wang, J., 2015. Influence of temperature on the water retention properties of compacted GMZ01 bentonite. Environ Earth Sci (2015) 73:4053–4061,

/WAN 18/ Wang, J., Chen, L., Su, R., Zhao, X.G., 2018. The Beishan underground research laboratory for geological disposal of high-level radioactive waste in China: Planning, site selection, site characterization and in situ tests. J. Rock Mech. Geotech. Eng. 10(2018)411-435. Doi.org/10.1016/j.jrmge.2018.03.002.

/WER 07/ Wersin, P., Johnson, L.H., McKinley, I.G., 2007. Performance of the bentonite barrier at temperatures beyond 100 °C: A critical review. Physics and Chemistry of the Earth 32(8–14): 780–788.

/XU 17/ Xu. L., Ye. W.M., Ye. B., 2017. Gas breakthrough in saturated compacted GaoMiaoZi (GMZ) bentonite under rigid boundary conditions, Can. Geotech. J. 54: 1139–1149 (2017) dx.doi.org/10.1139/cgj-2016-0220.

/YE 13/ Ye, W.M., Wan, M., Chen, B., Chen, Y.G., Cui, Y.J., Wang, J., 2013. Temperature effects on the swelling pressure and saturated hydraulic conductivity of the compacted GMZ01 bentonite. Environ Earth Sci 68(1):281–288.

/YON 12/ Yong, R.N., Nakano, M., Pusch, R., 2012. Environmental Soil Properties and Behaviour. CRC Press, Taylor & Francis Group.

/ZHA 04/   Zhang, C.L. and Rothfuchs, T., 2004. Experimental Study of Hydromechanical Behaviour of the Callovo-Oxfordian Argillites. Special Issue: Clays in Natural and Engineering barriers for Radioactive Waste Confinement, Reims, France, 2002. Applied Clay Science 26 (2004) 325-336. ISSN0169-1317.

/ZHA 13/   Zhang, C.L., Czaikowski, O., Rothfuchs, T., Wieczorek, K., 2013. Thermo-Hydro-Mechanical Processes in the Nearfield around a HLW Repository in Argillaceous Formations - Volume I: Laboratory Investigations, Gesellschaft für Anlagen- und Reaktorsicherheit (GRS) mbH, Braunschweig, GRS-312.

/ZHA 14/   Zhang, C.L., 2014. Characterization of Excavated Claystone and Claystone-Bentonite Mixtures as Backfill/Seal Material, Geological Scociety Special Publication 400 – Clays in Natural and Engineering barriers for Radioactive Waste Confinement (edited by Norris et al.), The Geological Society of London, 2014, 323-337.

/ZHA 15/   Zhang, C.L., 2015. Investigation of gas migration in damaged and resealed claystone, Geological Society Special Publication 415 – Gas Generation and Migration in Deep Geological Radioactive Waste Repositories (edited by SHAW, R.P.), The Geological Society of London, 75-93.

/ZHA 21/   Zhang, C.L., 2021. Deformation and water/gas flow properties of claystone/bentonite mixtures. J. Rock Mech. Geotech. Eng. 13 (2021) 864-874. https://doi.org/10.1016/j.jrmge.2020.12.003.

/ZHA 19/   Zhang, F., Ye, W.M., Wang. Q., Chen, Y.G., Chen, B., 2019. An insight into the swelling pressure of GMZ01 bentonite with consideration of salt solution effects, Engineering Geology 251 (2019) 190-196.

/ZHO 20/   Zhou, Z.C., Wang, J., Su, R., Guo, Y.H., Zhao, J.B., Zhang, M., Ji, R.L., Li, Y.N., Li, J.B., 2020. Hydrogeochemical and isotopic characteristics of groundwater in Xinchang preselected site and their implications, Environmental Science and Pollution Research (2020) 27:34734–34745. https://doi.org/10.1007/s11356-019-07208-1.

/ZHU 13/ Zhu, C.M., Ye, W.M., Chen, Y.G., Chen, B., Cui, Y.J., 2013. Influence of salt solutions on the swelling pressure and hydraulic conductivity of compacted GMZ01 bentonite. Engineering Geology, 166: 74–80. doi:10.1016/j.enggeo.2013. 09.001.

List of figures

List of tables